Analysis and Design of Axial Flux Permanent Magnet Wind Generator System for Direct Battery Charging Applications

by

Francois Gerhardus Rossouw

Thesis presented in partial fulfilment of the requirements for the degree of Master of Science in Engineering at the University of Stellenbosch

Department of Electrical & Electronic Engineering
Stellenbosch University
Private Bag X1, Matieland, 7602, South Africa

Supervisor: Prof M.J. Kamper

March 2009

Declaration

By submitting this thesis electronically, I declare that the entirety of the work contained therein is my own, original work, that I am the owner of the copyright thereof (unless to the extent explicitly otherwise stated) and that I have not previously in its entirety or in part submitted it for obtaining any qualification.

Signature: .....
F.G. Rossouw

Date: .....

Abstract

Analysis and Design of Axial Flux Permanent Magnet Wind Generator System for Direct Battery Charging Applications

F.G. Rossouw

Department of Electrical & Electronic Engineering
Stellenbosch University
Private Bag X1, Matieland, 7602, South Africa

Thesis: MScEng (Elec)

March 2009

In this study the focus is on the implementation of a coreless axial flux permanent magnet (AFPM) generator for use in a wind generator application with direct battery charging. The wind generator power system is analysed and discussed. The common concerns with AFPM wind generators in rectifier-fed direct battery charging applications, such as maximum power point matching and acoustic noise emission, are discussed.

In this study the AFPM wind generator is theoretically analysed and the different winding topologies for this type of machine are evaluated. This evaluation is based on a theoretical analysis and confirmed by finite element analysis and practical measurements. It is shown that an AFPM machine equipped with non-overlapping windings can give a similar performance to that of normal overlapping windings, while using less copper.

It is shown in this thesis that the coreless AFPM generator has a relatively low internal phase synchronous inductance resulting in severe problems with regard to maximum power matching and noise. A method is proposed and in detail analysed in this thesis whereby better power point matching is achieved and near-sinusoidal current is obtained using AFPM generators in direct battery charging wind energy systems. The wind generator system's performance is verified with a Simplorer^{TM} simulation package and practical measurements. The calculations from theoretically derived equations are in good agreement with finite element and measured results.

Uittreksel

Analise en Ontwerp van 'n Aksiaalvloed Permanente Magneet Wind Generator Sisteem in Battery Laai Toepassings

("Analysis and Design of Axial Flux Permanent Magnet Wind Generator System for Direct Battery Charging Applications")

F.G. Rossouw

Departement Elektriese & Elektroniese Ingenieurswese
Universiteit van Stellenbosch
Privaatsak X1, Matieland, 7602, Suid-Afrika

Tesis: MScIng (Elek)

Maart 2009

In hierdie studie word gefokus op die analiese en ontwerp van 'n aksiaalvloed permanente magneet generator vir gebruik in windgenerator toepassings. Die probleme met direk gekoppelde batterylaaier toepassings soos maksimum drywingspunt passing en akoestiese lawaai, word ook bespreek.

Die aksiaalvloed permanente magneet generator word teoreties geanaliseer en verskillende tipe wikkelings topologieë word geëvalueer. Die evalusie is bevestig deur eindige element analiese, asook praktiese metings. Daar word bewys dat aksiaalvloed permanente magneet masjiene met nie-oorkruisende wikkelings dieselfde effektiwiteit kan gee as normale oorkruisende wikkelings, terwyl minder koper gebruik word.

'n Metode word bereken waarvolgens beter maksimum drywingspunt passing en amper-sinusvormige strome verkry word in aksiaalvloed permanente magneet generators in windgenerator toepassings. Die werksverrigting van die windgenerator word geverifieer met gebruik van Simplorer™ simulasie sagteware, asook praktiese metings.

Acknowledgements

I would like to express my sincere gratitude to the following...

- The heavenly Father for giving me the strength and willpower.
- My promoter Prof. M.J. Kamper for his academic guidance and patience during the course of the project.
- My colleagues, at EMLab and US electrical workshop, for their advice and friendship.
- My family, my parents and brother, for their constant encouragement.
- My girlfriend, for her love, understanding of the situation and her encouragement.

Contents

Declaration **1**

Abstract **2**

Uittreksel **3**

Contents **5**

List of Figures **8**

List of Tables **13**

1 Introduction **1**
1.1 Wind power 2
1.2 The implemented wind turbine 5
1.3 Wind generation system 6
1.4 Axial flux permanent magnet generator 7
1.5 Wind generator power curve 9
1.6 Problem statement 12
1.7 Approach to the problem 12
1.8 Thesis layout 13

2 Alternative methods of control **14**
2.1 Pitch control 14
2.2 Connection switch-over 15
2.3 DC-DC converter 16
2.4 Controlled rectifier 16
2.5 Vienna Rectifier 17
2.6 Series capacitance 18
2.7 High voltage transformer 18
2.8 DC-transmission 19
2.9 Twelve-pulse rectifier 19
2.10 Passive harmonic filtering 19

2.11 3rd harmonic injection 20
2.12 Harmonic mitigating transformers 20

3 Theoretical analysis of the AFPM generator 22
3.1 AFPM topologies 22
3.2 Components 23
3.3 Winding layouts 27
3.4 Equivalent circuit 31
3.5 Analytical analysis 37
3.6 Finite element analysis 38

4 Analysis of proposed system 44
4.1 Theoretical analysis 45
4.2 Maximum power point matching 48
4.3 Analysis under rated conditions 51
4.4 Harmonic current analysis 52

5 Simulated and measured results 58
5.1 Practical test station 58
5.2 Commercially available wind generators 58
5.3 Uncompensated system 65
5.4 Stator winding comparative tests 68
5.5 Improved system 71
5.6 Acoustic noise measurement 79
5.7 Vibration tests 81

6 Conclusions and recommendations 87

Appendices 90

A Harmonic mitigating transformers 91

B Phase-grouped non-overlapping winding 95
B.1 Overview 95
B.2 Practical measurements 96

C Inductance calculation 98
C.1 Inductance 98
C.2 Non-overlapping winding inductance 98

D Eddy currents 100
D.1 Skin effect 100
D.2 Proximity effect 101

D.3 Eddy-current losses in a stranded wire 102

E Lead-acid battery **103**
E.1 Overview 103
E.2 Specific factors affecting performance 103
E.3 Equivalent circuit models 104
E.4 Thevenin equivalent model 104
E.5 Linear and non-linear battery models 104
E.6 Model used 105

F Equivalent circuit model **106**
F.1 Overview 106

G Dq-analysis **109**
G.1 Park transformation 109
G.2 5^{th} harmonic current analysis 110
G.3 5^{th} harmonic q-axis voltage 110
G.4 Inductance calculation 111

H Internal inductance measurements **112**
H.1 Standstill frequency tests 112
H.2 Decay tests 114
H.3 Load tests 114

Bibliography **117**

List of Figures

1.1 Classical windmill used for water pumping. 2
1.2 Wind generator setup on a farm. 2
1.3 Factors contributing to the power developed by a wind turbine. 3
1.4 Figures of drag and lift devices. 5
(a) Drag device 5
(b) Lift device 5
1.5 Figures of HAWT and VAWT [1]. 6
(a) Horizontal axis wind turbine 6
(b) Vertical axis wind turbine 6
1.6 Radial- and axial flux machines. 8
1.7 Schematic of AFPM machine. 9
1.8 Output power curve of the wind turbine at various wind speeds. 10
1.9 Schematic diagram of the wind generator power system. 11
1.10 Turbine power when connected to the existing wind generator system. . 11

2.1 Schematic diagram showing the dc-dc converter connected to the wind generator system. 16
2.2 Schematic diagram showing the controlled rectifier directly connected to the wind generator system. 17
2.3 Schematic diagram showing the Vienna rectifier directly connected to the wind generator system. 17
2.4 Transformer mitigation. 21

3.1 PM mounting types. 24
(a) Surface-mounted PM 24
(b) Embedded PM 24
3.2 Different PM shapes. 25
(a) Rectangular PM shape 25
(b) Annular PM shape 25
3.3 Trapezoidal coil shape. 26
3.4 Winding topologies for radial flux machines. 28
(a) Distributed winding 28

(b) Concentrated winding 28
3.5 Winding topologies for axial flux machines. 28
(a) Coreless AFPM overlapping winding 28
(b) Coreless AFPM non-overlapping winding 28
3.6 Schematic of the coreless normal overlapping winding. 29
3.7 3D drawing of coreless overlapping winding. 29
3.8 Schematic of coreless non-overlapping winding. 30
3.9 3D drawing of coreless non-overlapping winding. 30
3.10 Equivalent circuit of an AFPM generator. 31
3.11 Transpositioning of stranded wire. 36
3.12 Figures showing the finite element model and the element triangles. . . 40
(a) Overlapping winding model 40
(b) Model showing elements 40
3.13 Figures showing the finite element model and the element triangles. . . 40
(a) Non-overlapping winding model 40
(b) Model showing elements 40
3.14 Magnetic flux lines in overlapping winding (see Fig. 3.12. 41
3.15 Magnetic flux lines in non-overlapping winding (see Fig. 3.13. 41

4.1 Per-phase equivalent circuit diagram of the wind generator system. . . 45
4.2 Per-phase ac-equivalent circuit diagram of the wind generator system. . 46
4.3 Phasor diagram of the wind power system. 47
4.4 Back-EMF voltage at base speed ad rated speed. 47
4.5 Simplified graph of the power matching showing operating points b and r. 48
4.6 Simplified equivalent circuit diagram of the system. 49
4.7 Simplified phasor diagram of the wind power system. 49
4.8 Equivalent circuit of the wind power system. 51
4.9 The fundamental equivalent circuit diagram. 53
4.10 The 5^{th} harmonic d-axis equivalent circuit diagram. 54
4.11 The 5^{th} harmonic q-axis equivalent circuit diagram. 55

5.1 Laboratory test setup. 59
5.2 Open- and short-circuit tests. 61
(a) Open-circuit test 61
(b) Short-circuit test 61
5.3 Competitor wind generator voltage and current with rectifier-resistor load. 62
5.4 Equivalent circuit of the wind generator connected to the rectifier-battery load. 62
5.5 Competitor wind generator voltage and current with rectifier-battery load. 63
5.6 Wind generator power point matching. 64
5.7 Harmonic current analysis of competitor unit at 50 Hz. 64
(a) Line current (Time domain) 64

(b) Line current (Frequency domain) 64
5.8 Uncompensated wind generator voltage and current with rectifier-battery load. 66
5.9 Power point matching of the uncompensated system. 67
5.10 Harmonic current analysis of the uncompensated system at 40 Hz. . . . 68
(a) Line current (Time domain) 68
(b) Line current (Frequency domain) 68
5.11 Normal overlapping winding. 69
5.12 Harmonic analysis of the back-EMF at 40 Hz. 70
(a) Back-EMF (Time domain) 70
(b) Back-EMF (Frequency domain) 70
5.13 Non-overlapping winding. 70
5.14 Harmonic analysis of the back-EMF at 40 Hz. 71
(a) Back-EMF (Time domain) 71
(b) Back-EMF (Frequency domain) 71
5.15 Equivalent circuit model of the wind generator system in Simplorer™. 73
5.16 Power point matching with varying L_e values. 74
5.17 Current harmonic with varying L_e values. 75
(a) Effect of L_e on line current waveform. 75
(b) Current harmonic component versus L_e values. 75
5.18 Practical measurements versus the fundamental analysis of the voltage and current waveforms of the wind generator system. 76
(a) Measured voltage and current waveforms. 76
(b) Analysed voltage and current waveforms. 76
5.19 Wind generator loaded with rectifier-battery load. 77
5.20 Wind generator power point matching with $L_e = 7.5$ mH. 77
5.21 Harmonic current analysis of the improved system at 40 Hz with $L_e = 7.5$ mH. 78
(a) Line current (Time domain) 78
(b) Line current (Frequency domain) 78
5.22 Acoustic measurement of the competitor unit in the audible spectrum. 80
5.23 Zoomed-in absolute acoustic measurement of the competitor unit. . . . 80
5.24 Zoomed-in absolute acoustic measurement of AFPM wind generator system. 82
(a) Without external inductance 82
(b) With external inductance 82
5.25 Determining the natural frequency of the rotor of the AFPM machine. 83
(a) Natural frequency (Time domain) 83
(b) Natural frequency (Frequency domain) 83
5.26 Determining the natural frequency of the stator of the AFPM machine. 84
(a) Natural frequency (Time domain) 84
(b) Natural frequency (Frequency domain) 84

5.27 Vibration measurement of the AFPM generator with resistive load. . . 85
(a) Output voltage (Time domain) 85
(b) Output voltage (Frequency domain) 85
5.28 Vibration measurement of AFPM generator with rectifier-battery load. 86
(a) Output voltage (Time domain) 86
(b) Output voltage (Frequency domain) 86
5.29 Vibration measurement of AFPM generator with rectifier-battery load and external inductance. 86
(a) Output voltage (Time domain) 86
(b) Output voltage (Frequency domain) 86

6.1 Wind generator power point matching. 88

A.1 Phasor diagrams of the fundamental currents on the primary sides of the transformers. 92
A.2 Phasor diagrams of the fundamental currents on the secondary sides of the transformers. 92
A.3 Phasor diagrams of the 5^{th} harmonic currents on the secondary sides of the transformers. 93
A.4 Phasor diagrams of the 5^{th} harmonic currents on the primary sides of the transformers. 93
A.5 Phasor diagrams of the 7^{th} harmonic currents on the secondary sides of the transformers. 94
A.6 Phasor diagrams of the 7^{th} harmonic currents on the primary sides of the transformers. 94

B.1 Schematic of phase-grouped non-overlapping winding. 95
B.2 Phase-grouped non-overlapping winding. 96
B.3 Harmonic analysis of the back-EMF at 40 Hz. 97
(a) Back-EMF (Time domain) 97
(b) Back-EMF (Frequency domain) 97

C.1 Cross-section of the round estimation of the coil. 99

D.1 Figures showing skin and proximity effect. 102
(a) Skin effect 102
(b) Proximity effect 102

F.1 Per-phase equivalent circuit diagram of the wind generator system. . . 107
F.2 Rectifier terminal voltage. 107
F.3 Per-phase ac-equivalent circuit diagram of the wind generator system. . 108

H.1 connection diagram for d and q-axis inductance measurement. 113
(a) d-axis alignment of the rotor. 113

(b) connection diagram for d-axis inductance measurement. 113
(c) connection diagram for q-axis inductance measurement. 113
H.2 Decay test setup. 115
(a) *d*-axis decay test 115
(b) *q*-axis decay test 115
H.3 Phasor diagram of the AFPM generator with balanced resistive load connected. 116
(a) Load test to calculate the inductance of the system. 116
(b) Sine method of solving triangles 116
(c) Sine method of solving triangles 116

List of Tables

5.1 Wind generator data 60
5.2 Design data 72
5.3 Power matching 74
5.4 Harmonic suppression 75

Nomenclature

Constants

$\rho_a =$ 1,225 kg/m^3 at sea level
$C_p =$ 0,593 Betz criterion
$\pi =$ 3,141 592 653 589 793 238 462 643 383 279 5
$\rho_{20} =$ 17 nωm at 20 °C
$\gamma_{Cu} =$ 8,94 g/cm^3

Variables

E_{wk}	Kinetic energy from the wind (J)
V_a	Volume of air (m^3)
P_a	Power extracted from wind (W)
A_s	Swept area of the wind turbine (m^2)
v_w	Wind velocity (m/s)
P_{max}	Maximum mechanical power (W)
λ_s	Tip speed ratio
r_t	Turbine blade radius (m)
ω_{mec}	Mechanical angular velocity of the turbine (m/s)
C_D	Drag coefficient of wind turbine
F_D	Drag force of wind turbine (N)
F_L	Lift force of wind turbine (N)
l_e	End-winding length of coil (m)
l_a	Active length of coil (m)
τ_c	Coil pitch
τ_p	Pole pitch
n	Number of coils per phase group
E_{gen}	RMS Back-EMF of AFPM generator (V)
R_{eddy}	Resistance of the eddy current loss component (Ω)

R_i	Internal resistance of the AFPM stator winding (Ω)
L_i	Internal inductance of the AFPM stator winding (H)
I_{ac}	Phase current of AFPM generator (A)
V_{gen}	Terminal voltage of AFPM generator (V)
E_o	Back-EMF of AFPM generator with overlapping stator winding (V)
q	Number of stator coils in series per phase
a	Number of parallel circuits per phase
p	Number of poles
ω_e	Electrical rotating speed of generator (rad/s)
B_p	Peak air-gap flux density (T)
N_t	Number of turns per coil
r_e	Average radius of AFPM stator winding (m)
k_{po}	Pitch factor of overlapping winding
Q	Number of stator coils per phase
B_g	Dc flux density in airgap (T)
r_i	Inner radius of AFPM stator winding (m)
r_o	Outer radius of AFPM stator winding (m)
θ_{re}	coil-width-angle at radius r_e ($^\circ$)
l_g	Axial length of airgap in AFPM (m)
E_c	Back-EMF of AFPM generator with non-overlapping stator winding (V)
k_{pc}	Pitch factor of non-overlapping winding
k_d	Distribution factor
ρ_t	Resistivity of copper at temperature t (Ωm)
l_{eo}	End-winding length of overlapping winding (m)
l_{ec}	End-winding length of non-overlapping winding (m)
k_f	Filling factor
w	Width of a coil-side (m)
h_a	Axial height of the AFPM stator winding (m)
L_o	Inductance of overlapping winding (μH)
L_c	Inductance of non-overlapping winding (H)
K_n	Nagaoka constant
P_{eddy}	Eddy-current losses in AFPM stator winding (W)
d	Diameter of round conductor (m)
N_p	Number of parallel strands
T_d	Developed torque (Nm)

k_s	Stator factor
k_e	End-winding factor
k_r	Radius factor
C_1	Machine parameter 1
k_{so}	Stator factor of overlapping winding
k_{sc}	Stator factor of non-overlapping winding
k_{wc}	Winding factor of non-overlapping winding
k_{eo}	End-winding factor of overlapping winding
k_{ec}	End-winding factor of non-overlapping winding
P_{Cu}	Copper losses of AFPM stator winding (W)
M_{Cu}	Total mass of copper in AFPM stator winding (kg)
k_m	Mass factor
C_2	Machine constant 2
Z_i	Internal impedance of AFPM stator winding (Ω)
Z_c	Impedance of connecting cable (Ω)
L_e	Inductance of external inductor (H)
T_m	Wind turbine mechanical torque (Nm)
ω_m	Mechanical rotating speed (rad/s)
R_e	Resistance of external inductor (Ω)
V_{rec}	Rectifier voltage (V)
R_{dc}	Battery internal resistance (Ω)
V_{bat}	Open-circuit voltage of battery bank (V)
V_{dc}	Dc-bus voltage (V)
I_{dc}	Dc battery charging current (A)
V_b	Fundamental RMS ac-equivalent battery voltage (V)
R_{ac}	Ac-equivalent battery internal resistance (Ω)
V_d	Forward conducting volt drop across a diode (V)
θ	Power angle ($^\circ$)
δ	Load angle ($^\circ$)
α	Phase angle ($^\circ$)
n_b	Cut-in rotating speed of wind generator (r/min)
n_r	Rated rotating speed of wind generator (r/min)
E_{gr}	Rated back-EMF of the wind generator (V)
P_{tr}	Rated output power of the wind turbine (W)
L_s	System inductance of wind generator system (H)

R_s	Phase resistance of wind generator system (Ω)
R_{cc}	Resistance of the connecting cable (Ω)
L_{cc}	Inductance of the connecting cable (H)
I_r	Rated current in wind generator system (A)
ω_{er}	Rated electrical rotating speed of wind generator (rad/s)
δ_r	Rated load angle
T_r	Rated developed torque of the wind generator (Nm)
ω_{mr}	Rated mechanical rotating speed of wind generator (rad/s)
η_{sys}	Wind power system efficiency (%)
P_{dc}	Rated power delivered to battery bank (W)
P_{rr}	Rated power at the rectifier (W)
V_{rr}	Rated rectifier voltage (V)
η_{gr}	Wind generator efficiency (%)
P_{gr}	Rated power of the wind generator (W)
h	Harmonic order
k	Any integer
E_{g1}	Fundamental back-EMF of wind generator (V)
I_1	Fundamental phase current (A)
V_{b1}	Fundamental harmonic source voltage (V)
i_{d5}	5^{th} harmonic d-axis current (A)
i_{q5}	5^{th} harmonic q-axis current (A)
v_{q5}	5^{th} harmonic q-axis voltage (A)
L_d	d-axis inductance of the wind generator (H)
E_d	d-axis back-EMF of the wind generator (V)
E_q	q-axis back-EMF of the wind generator (V)
E_{oc}	Open-circuit voltage of the wind generator (V)
I_{sc}	Short-circuit voltage of the wind generator (A)
X_{Li}	Internal inductive reactance of the wind generator (Ω)

Chapter 1

Introduction

In recent years there has been a renewed interest in wind as a source of energy due to energy consumers becoming more concerned for the environment. The environmental concerns are as a result of the damage inflicted on the environment due to the burning of millions of tons of fossil fuels. In order to limit the damage already done to the environment, massive wind farms are erected to serve as an alternative to the coal-fired power stations. It is vital that environmentally friendly alternatives to fossil fuel are investigated, not only at the high power generation levels but also at much lower power levels. Renewable energy sources that are suitable for small-scale power generation include, amongst others, wind and solar energy. These two complementary energy sources are steadily becoming more economically viable and are considered as viable alternatives to diesel powered generators for use in remote locations. A major benefit of wind generators for remote operators is that they do not occupy large areas of fertile land that could have been used for agricultural purposes.

Unlike diesel generators, wind generators generate electrical power from an unlimited and sustainable power source. The pollution-free power that is generated by wind turbines has already been used for many years. Wind power was first used in early windmills and later for pumping water in classical windmills. A photograph of a classical windmill is shown in Fig. 1.1.

In conventional large-scale wind generator power systems, the generated power from the wind farms is fed directly into the national grid. From the grid the power is used by the connected consumers [2]. The alternative to grid-connected wind generator systems is smaller, stand-alone wind generator systems. These stand-alone systems are used to supply power to private houses, farms and other remote locations where access to the electrical utility grid is impractical and/or expensive [3]. Such isolated, stand-alone wind generator systems are used mostly for the charging of storage batteries. This topology has been proven over the years to be simple, reliable and versatile [4]. Due to the popularity of such systems it would be advantageous if these stand-alone wind generator systems could be

Figure 1.1: Classical windmill used for water pumping.

Figure 1.2: Wind generator setup on a farm.

operated closer to their maximum efficiency.

To be able to practically test the wind generation system and evaluate its benefits and short-comings, a prototype was set up on a farm in Upington in the Northern Cape, South Africa. The small-scale power generation system consists of a 1 kW wind generator and panels of photo-voltaic cells, as shown in Fig. 1.2. It should be noted that only the wind generator is investigated in this thesis.

1.1 Wind power

The purpose of a wind turbine is to convert the kinetic energy available from the wind into rotating mechanical energy, while the purpose of the wind generator is to convert that mechanical energy into electrical energy [5]. The kinetic energy that is present in the wind is due to wind consisting of moving air. Although air has a low density, it has mass and therefore possesses kinetic energy. The kinetic energy of the wind, E_{wk}, can be calculated by

$$E_{wk} = \frac{1}{2}\rho_a V_a^2 \tag{1.1.1}$$

where ρ_a is the air density at sea level and V_a is the volume of air which is interacting with the turbine. The available power, P_a, that can be extracted from the given volume of wind can be calculated by

$$P_a = \frac{1}{2}\rho_a A_s v_w^3 \tag{1.1.2}$$

where A_s is the area swept by the blades and v_w is the wind velocity. These factors are shown in Fig. 1.3. P_a is the total power available from the wind, but only a fraction of this available power can be extracted. Some of the kinetic energy from the airflow must be retained so that the wind can travel through the wind turbine. Thus, a wind turbine cannot extract all of the energy available from a certain volume of wind [6]. The maximum mechanical power, P_{max}, that can be developed by a wind turbine can be calculated by

$$P_{max} = \frac{1}{2}C_p\rho_a A_s v_w^3 \tag{1.1.3}$$

where C_p is the turbine power coefficient which has a theoretical limit of 0,593. This limit is referred to as the Betz criterion. The Betz criterion is the maximum fraction of available power that can be extracted from the wind by an ideal turbine, which can also be understood as the wind turbine's efficiency. Any further possible mechanical and electrical inefficiencies must still be taken into account. Therefore C_p is the ratio of the mechanical power at the turbine shaft to the power available from the wind. Thus, in order to extract the maximum amount of power from the wind, it is necessary to keep C_p as high as practically possible [7].

Tip speed ratio

In order to obtain maximum wind turbine efficiency, the angular rotational velocity of the wind turbine should be matched to the incoming wind velocity. A wind

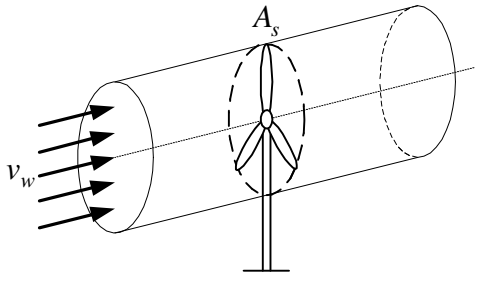

Figure 1.3: Factors contributing to the power developed by a wind turbine.

turbine that is rotating at a very low speed will allow the wind to pass through the gaps between the blades undisturbed, while a wind turbine that is rotating at a very high speed will appear as a solid barrier to the incoming wind [5]. Under both of the above-mentioned circumstances no or low power will be generated. A method that is used to optimise the wind turbine is to determine the tip speed ratio of the turbine. The tip speed ratio, λ_s, is the ratio of the linear velocity of the tip of the blade to that of the undisturbed wind velocity entering the wind turbine. This ratio can be calculated by

$$\lambda_s = \frac{r_t \omega_{mec}}{v_w} \tag{1.1.4}$$

where r_t is the radius of the turbine blade and ω_{mec} is the mechanical angular velocity of the wind turbine [8]. A higher tip speed ratio has the advantages of an increase in the power coefficient, C_p, as well as a reduction in the shaft torque and rotational wake losses. The disadvantages of high tip speed ratios are the low starting torque and the acoustic noise created by the fast-moving blade tips [9].

The classical windmills with their multiple blades, which are shown in Fig. 1.1, are referred to as high solidity turbines. This is where a large fraction of the swept area is occupied by the turbine blades. These turbines have low tip speed ratios, typically between 1 and 2, which delivers high starting torque at low wind speeds. The resultant C_p for these turbines is below 0.2, this is due its high drag coefficient, C_D. Hence, these turbines are referred to as drag devices. In a drag device the wind creates a drag force, F_D, perpendicular to the area of the turbine blade, as indicated by the diagram in Fig. 1.4a [10]. The drag force, F_D, is converted into mechanical power by the rotating wind turbine. The modern, narrow, three-bladed turbine rotors are lift devices, working on the principle of aerodynamic lift. Lift devices have a much lower C_D due to its airfoil profile. As the incoming wind hits the blade profile, the drag force, F_D, and a lift force, F_L, are created. The drag component is aligned with the incoming wind and the lift component perpendicular to it, as indicated by the diagram in Fig. 1.4b. Only the much larger F_L is converted into mechanical power, while F_D acts as a braking force. Nevertheless, lift devices can have a much higher C_p value, up to 0.5, and have much higher tip speed ratios, typically between 6 and 8. Compared to drag devices, lift devices operate at much higher rotational speeds and consist of a lower fraction of swept area giving them a higher λ_s, hence they are referred to as low solidity turbines.

Regardless of the wind turbine topology each wind turbine has a particular tip speed ratio that will produce the maximum turbine power coefficient, C_p, in order to obtain its maximum operating efficiency [5]. Therefore it is important to operate the wind turbine at or near to its maximum efficiency to extract the power from the available wind.

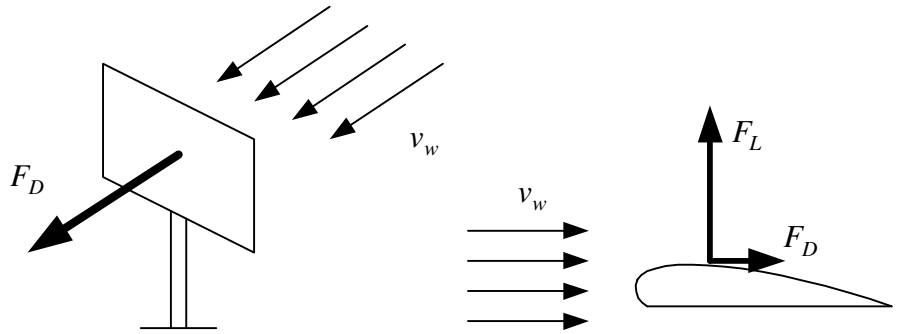

(a) Drag device (b) Lift device

Figure 1.4: Figures of drag and lift devices.

1.2 The implemented wind turbine

Wind turbines can be divided into two types and are distinguished by the turbine's orientation. The two types are the horizontal- (HAWT) and the vertical axis wind turbines (VAWT), which are shown in Fig. 1.5. Both the HAWT and the VAWT wind turbines operate on the principle of aerodynamic lift. Of the two types, the HAWT's are the most frequently used due to their simplicity and lower cost [2].

Horizontal-axis wind turbines featuring three blades have become extremely popular in recent years due to the smooth power delivery compared to that of one- and two-bladed wind turbines. Three-bladed wind turbines also feature improved dynamic stability compared to one-, two- or four-bladed wind turbines [9]. Another major factor of their popularity is that of the financial implications in the manufacturing of multiple blades [10]. Therefore it seems that three-bladed HAWT's are the obvious choice from both a power delivery and financial perspective.

There are many commercial wind generators in the 1 kW power level available on the South African market. Unfortunately, not many of them were designed for the low South African wind conditions they have to operate in. The South African wind speeds are typically in the order of 2 to 8 m/s, which is substantially lower than in European countries. Thus to maximise the power extracted from the low available wind, a wind turbine is needed that has a high aerodynamic efficiency at low wind speeds.

The turbine blade, that has been used in this study has been specifically designed and optimised for low wind speed efficiency, whilst restricting aerodynamic noise. The low speed efficiency has been achieved by keeping the tip speed of the turbine as low as practically possible. The relatively low tip speed ratio also results in greater starting torque in the targeted low speed area [11]. The tapered and twisted turbine blades are also comparatively broad, further enhancing the starting torque when compared to narrower high speed blades, while adding mechanical strength to the turbine.

(a) Horizontal axis wind turbine (b) Vertical axis wind turbine

Figure 1.5: Figures of HAWT and VAWT [1].

1.3 Wind generation system

The wind turbine forms just one part of the complete wind generation system. In this section the other required parts that make up a small-scale wind generator system are investigated. As mentioned in the previous section, the wind turbine implemented is a horizontal-axis wind turbine. There are various different HAWT topologies available on the market, which can mainly be divided into two groups, upwind- and downwind wind turbines. Horizontal-axis upwind wind turbines are referred to as such due to the orientation of the turbine's axis and due to the orientation of the wind turbine with respect to the tower mast. In upwind turbines, the wind turbine rotates in front of the mast while the turbine head is guided into the direction of incoming wind with the aid of a tail vane. This method of guidance is referred to as yawing. Downwind turbines have the wind turbine rotating behind the mast. This topology has the advantage of being able to orientate itself into the wind without depending on a tail vane. This method of guidance is referred to as free-yawing. The disadvantage of downwind wind turbines is that each of the turbine blades has to periodically pass through the turbulent airflow created by to the tower shadow. The turbulence can create problems regarding noise and an undesired turbine output power ripple [10]. Due to the problems associated with

downwind wind turbines, the most common topology for small-scale wind turbines is the horizontal-axis upwind wind turbine with passive tail vane control [4]. This topology is very simple and requires minimum maintenance.

The tail vane which is used for yawing in an upwind turbine was adopted from the classical windmills, which are shown in Fig. 1.1. The yawing is required for protection of the wind generator during high wind speed conditions which could be hazardous to the wind generator. During these particular conditions the tail vane of the generator, which is mounted off-centre from the axis of the turbine, pushes the wind turbine out of the direction of the incoming wind, thereby adjusting the angle of the wind turbine to the wind [4]. Yawing is a simple and inexpensive method of control because it does not require any external control or a wind velocity meter.

Other than the wind turbine and yaw head, another critical part of the wind generation system is the tower. The wind generator's mast serves other functions than purely keeping the wind generator aloft. In order to maintain the highest possible system efficiency in low voltage, low power generation, the wind generator has to be located physically as close to the load as practically possible. This minimises the transmission losses in the cable used to connect the wind generator to the load. Typically, the wind turbine should be mounted in an elevated physical position, as most sites have a positive wind shear. A positive wind shear is when the wind velocity increases with elevation [9]. A further need for the elevated physical position is to be clear of obstructions which would create turbulent airflow. As a rough estimate, if an air stream passes over an object of a certain height, the turbulence in the air stream only subsides sufficiently after fifteen times the length of the height of the object [10]. Therefore, a wind turbine should never be mounted on top of a building's roof. The airflow across a roof will be turbulent and the resulting thrust on the wind turbine may damage the turbine and/or the roof [12].

A further note is that when the wind generator is mounted high above the ground, on top of a supporting structure, it is subjected to undisturbed, high airflow. The cooling capabilities of this high airflow permit heavy loading of the wind generator. This is possible because during high wind speeds, the heat produced by the heavily loaded generator is high, while the heat transfer available from the wind is high [13].

1.4 Axial flux permanent magnet generator

In the wind generation system, the wind turbine and the electric generator are directly connected to each other. Direct-drive operation is performed in order to minimise the mechanical losses in the system by eliminating the use of a gearbox [13, 14]. Wind generator systems generally make use of a gearbox so that the turbine rotating speed can be geared-up which enables the generator to rotate at a higher rotating speed than the wind turbine. Thereby the wind generator

is able to generate higher power at low wind speed conditions [2]. A gearbox has the disadvantage of being expensive, heavy, inefficient and requiring routine maintenance and lubrication of its many internal moving parts. By removing the gearbox from the system, a direct-drive system can achieve higher performance with less mass compared to a generator-gearbox combination [15].

Directly connected, synchronous generators with permanent magnet excitation have been popularly used in the past as wind generators. But, the poor quality of the permanent magnets of that time nearly rendered the technology obsolete. The invention of high-energy rare-earth permanent magnets consisting of an alloy called Neodemium-Iron-Boron (NdFeB) created the possibility of topologies which were not practical in the past [1]. These rare-earth permanent magnets are highly effective but very expensive [16]. The use of permanent magnets as rotor excitation creates the possibility of higher generator efficiency by eliminating the excitation losses in the rotor. Therefore, no external power source is required for excitation, which eliminates the use of the carbon brushes in the machine [17]. The removal of the carbon brushes together with the removal of the gearbox results in a system requiring no maintenance. The disadvantage, however, of permanent magnet excitation is that the output voltage of the generator can only be manipulated by a change in the rotating speed of the rotor, as the rotor excitation voltage cannot be changed [10].

In conventional machines, the magnetic field is in the radial direction. These types of machines are referred to as radial flux machines (RFM). The generator that is implemented here is of the axial flux machine (AFM) topology. The magnetic field of an AFM is in the axial direction. Fig. 1.6 illustrates the different magnetic field directions of the RFM and AFM topologies.

An axial flux machine with permanent magnet excitation is referred to as an axial flux permanent magnet (AFPM) machine. A cross-sectional schematic of the AFPM machine is shown in Fig. 1.7. The rotor of the AFPM generator consists of two interconnected steel disks. The rotor disks house the surface-mounted, axially magnetised permanent magnets [18]. The iron-less stator of an AFPM is located between the two opposing steel rotor disks and consists of only epoxy encapsuated

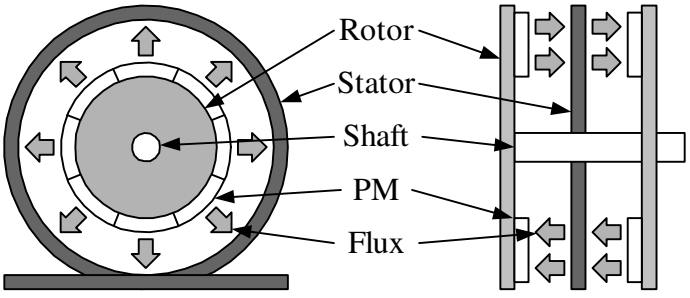

Figure 1.6: Radial- and axial flux machines.

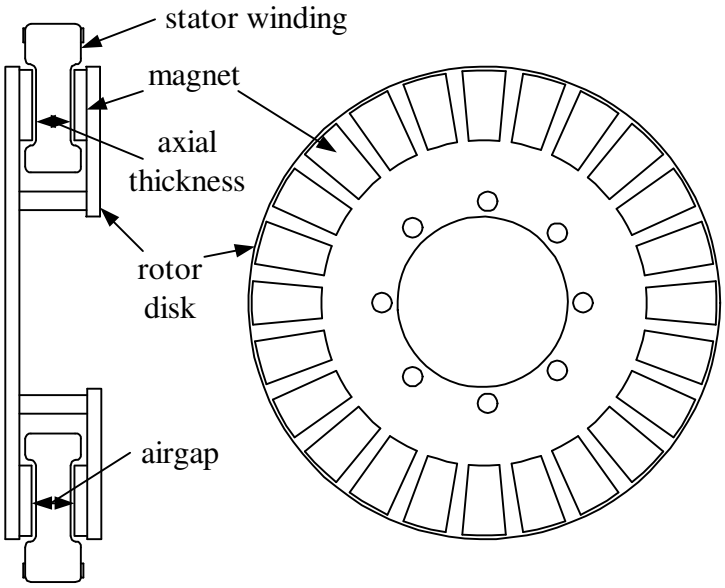

Figure 1.7: Schematic of AFPM machine.

conductors which are placed radially. The construction creates a compact, power dense machine with a short axial length and a comparatively large diameter. These compact machines with their disk shape make them ideal for small-scale wind generation [19]. The disk shape of an AFPM generator creates the ideal mounting plane for the blades of the wind turbine.

1.5 Wind generator power curve

The wind turbine used in this thesis is regarded as a fixed pitch turbine. A fixed pitch turbine has a constant angle of the orientation of the turbine blade to the incoming wind. A wind turbine with fixed-pitch turbine blades will produce a certain mechanical power output, which is a function of the rotating speed of the wind turbine, at each individual wind speed. This is illustrated by the solid lines in Fig. 1.8.

It can be seen in Fig. 1.8 that the wind turbine has a minimum wind speed which is required before the wind turbine will start to rotate. This minimum wind speed is referred to as the cut-in wind speed of the wind turbine. Thus, the cut-in wind speed is the wind speed at which the starting torque of the wind turbine is developed. It is obvious that for the design of a wind generator intended to suit low wind speed conditions, the starting torque should be developed at the lowest possible wind speed. This requirement will enable the wind generator the highest energy capture in low wind speed conditions. From wind turbine cut-in, the wind turbine rotating speed increases to a point where the maximum power is delivered

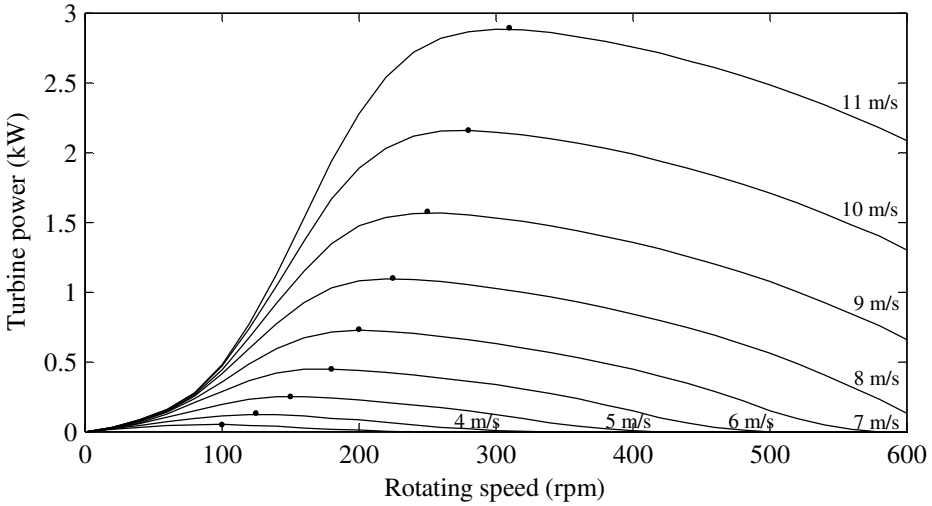

Figure 1.8: Output power curve of the wind turbine at various wind speeds.

for a particular wind speed. It is apparent that for each particular wind speed there is a certain point at which the wind turbine produces the maximum power. The maximum power points are indicated by the dotted peaks in Fig. 1.8. At rotating speeds greater than that of the maximum power points, the developed power starts to decrease as the wind turbine stalls aerodynamically. In this region there is a loss in the energy captured, which is due to the wind turbine operating away from its maximum C_p and therefore away from its maximum aerodynamical efficiency [4].

The wind generator is operated in a direct battery charging application, where the wind generator is directly connected to a rectifier-battery combination. The rectifier-battery combination consists of a three-phase full-bridge diode rectifier directly connected to a battery bank of three batteries. The wind generator system with the rectifier-battery load is illustrated by the block-diagram in Fig. 1.9, where Z_i, Z_c and Z_e are the internal impedance of the wind generator, the impedance of the cable and external impedance, respectively.

The output power generated by the existing wind generator system was measured practically and the result is shown in Fig. 1.10. It should be noted that the output power developed by the wind turbine could also be interpreted as the input power delivered to the wind generator.

From Fig. 1.10, the rotating speed of the wind generator increases from zero to a point where the wind generator starts generating power. This specific rotating speed can be referred to as the cut-in speed of the wind generator. At the wind generator cut-in speed, the ac-voltage produced by the wind generator is equivalent to the dc-voltage of the battery bank. This is also referred to as the clamping voltage of the battery bank. As the rotating speed of the wind generator increases from cut-in, the output voltage of the wind generator increases and phase current

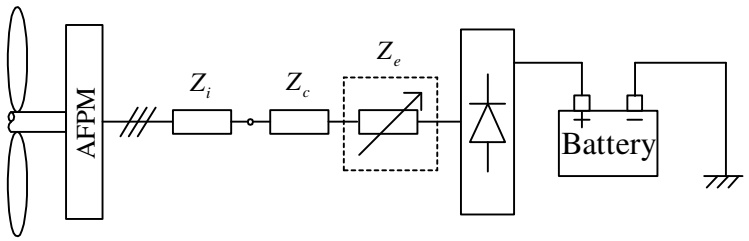

Figure 1.9: Schematic diagram of the wind generator power system.

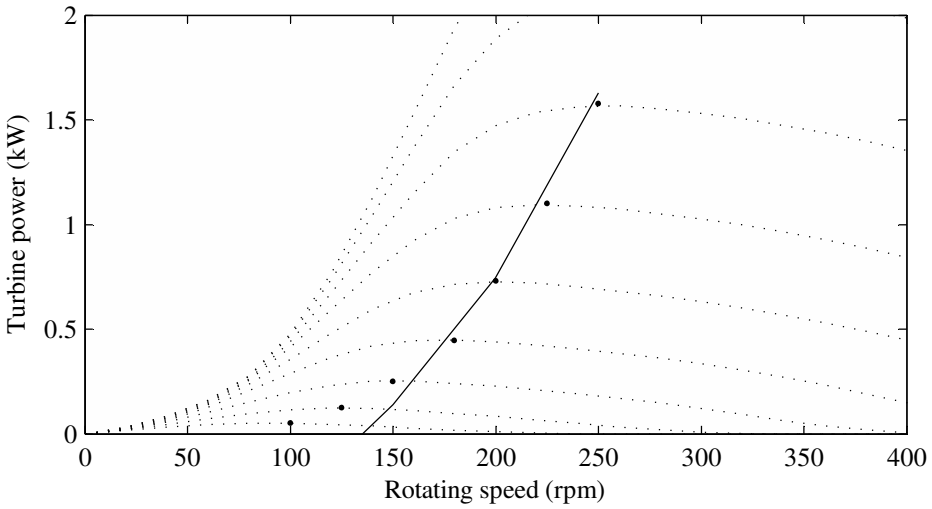

Figure 1.10: Turbine power when connected to the existing wind generator system.

starts flowing to the connected load. The power developed increases near-linearly to a point where the wind generator is operating under its rated conditions. At the rated conditions, the wind generator is operating at its rated rotating speed and generating rated power. At rotating speeds above the rated condition, the wind turbine is not operating at its optimum efficiency and output power developed diminishes. Due to safety concerns, it is necessary to limit the rotating speed of the wind generator to ensure its mechanical integrity. The power generated by the high rotating speed of the wind turbine should also be limited to the rated conditions of the wind generator.

From the load line indicated by the solid line in Fig. 1.10, it is shown that the existing wind generator system is operating at its maximum efficiency only in the medium to high wind speed range and not in the low to medium range. It is therefore obvious that in order to extract the highest output power from the wind turbine, the wind generator needs to follow the indicated maximum power points precisely. Maximum power point tracking is normally achieved with an electronic device designed to adjust the load connected to the wind generator so that the wind

turbine power matches the ideal maximum power points graph [20]. The purpose of this study is to create a method of passive power point tracking.

1.6 Problem statement

In this section the problems regarding the small-scale wind generator system are discussed. The first concern is the lower than anticipated levels of power generated by small-scale wind generator systems. This is due to wind being an inconsistent source of power as there is no continual flow. For this reason a good wind site has a capacity factor of roughly 25 %, which is calculated at an average wind speed of 6 m/s [20]. Southern Africa has much lower average wind speed, creating a capacity factor with an even lower value. Therefore, it has been shown in practice that the energy capture and power delivery of small variable-speed wind turbines, used for battery charging applications, very often fall short of expectations based on the ratings of the turbine and generator [4]. If the electrical load does not match the wind turbine, the performance of the system will be further degraded. The goal is to model and analyse the system, thereby predicting the performance improvements that can be made in order to alter the system configuration to better match the load to the wind turbine [7].

The second concern is the acoustic noise emitted by the AFPM generator. The acoustic noise is created as a result of the rectifier-battery load connected to the wind generator. The rectifier-battery load creates non-sinusoidal current flow in the system which is due the low internal inductance of the coreless stator winding. The low internal inductance of the AFPM is unable to create enough of a filtering effect in order to eliminate the current harmonics. The harmonics in the non-continuous current which are introduced into the system consist of odd, non-triplen harmonics. The 5^{th}, 7^{th}, 11^{th}, 13^{th}, 17^{th} and 19^{th} current harmonics are the most dominant.

1.7 Approach to the problem

To solve the problem of the low wind speed energy capturing ability of the wind generator, the cut-in speed should be lowered. The cut-in speed can be directly linked to the battery clamping voltage. In order to lower the cut-in speed of the wind generator, the battery voltage can be selected so that the cut-in speed can be obtained at a lower wind generator rotating speed. The outcome of the change to the lower battery voltage is a gain in power generated at low wind speeds. The drawback of this method of power matching is that there will be a substantial loss in the power generated at the higher wind speeds, due to the non-optimal loading [4].

To achieve closer to optimal loading of the wind generator, the characteristics of the wind generator need to be matched to those of the connected load. The

alternative to the adjustment of the battery bank voltage, thereby effectively adjusting the load to suit the wind generator, is to adjust the output voltage from the wind generator to suit the characteristics of the rectifier-battery load. This can be achieved by redesigning the stator winding of the wind generator so that the load can be provided by the standard voltage of a battery bank. The revised stator winding will achieve a higher output voltage in order to create a lower cut-in speed. As with adjustment of the battery voltage, the energy capture is only improved under the low wind speed conditions.

The higher output voltage of the revised stator winding is primarily achieved by increasing the number of turns on the stator coils. This also has the further benefit of increasing the low value of internal inductance of the coreless AFPM generator. The slight increase in internal inductance has a positive effect on the maximum power point tracking. Thus by adding some additional external inductance to the wind generator system, near-optimum passive maximum power point tracking can be achieved. The external inductor is connected in series on the ac-side of the rectifier, as shown in Fig. 1.9. A further benefit with the addition of the external inductance is that the side effect of the optimal system inductance will lead to the elimination of noise emission by the wind generator.

1.8 Thesis layout

Chapter 1: In this chapter the history of wind power is summarised. The types of wind turbines and the positioning of a good wind site are discussed. The AFPM generator which is to be used is introduced and the problem surrounding the power matching of the generator to the turbine is investigated.

Chapter 2: Alternative solutions to the problems that were discussed in Chapter 1 are discussed.

Chapter 3: The AFPM generator that is to be used is examined and new winding layouts are developed. A stator is redesigned and finite element analysis of the AFPM generator is performed.

Chapter 4: In this chapter the system is analysed and the effect of the additional series inductances is evaluated in terms of current harmonics and power matching. An optimum value of series inductance is calculated to obtain near-maximum power point matching.

Chapter 5: In this chapter the results of the simulations and practical results are evaluated.

Chapter 6: Conclusions

Chapter 2

Alternative methods of control

In this chapter other methods of solving the issues associated with a small-scale wind generator system with direct battery charging, such as power matching and noise emission, are discussed. None of these methods have been properly analysed and the reasons for their dismissal are mentioned.

2.1 Pitch control

Most small-scale wind turbines are of the fixed-pitch stall-regulated topology where the wind turbine relies on the inherent aerodynamic stall to limit the peak power. Stalling as a method of limiting the output power of small-scale wind generators is very popular due to the low cost and minimal maintenance.

In most medium to large scale horizontal-axis wind turbines pitch control is used to control the starting torque, braking torque and aerodynamic power of the wind turbine. Pitch control is a method of control where the pitch of the turbine blade is adjusted with respect to the angle of the incoming wind. As the angle of the turbine blade is adjusted the power coefficient, C_p, of the wind turbine changes. In order for the wind turbine to extract the maximum power available from the wind in all wind conditions, C_p should be kept at its maximum value. In order to achieve the maximum C_p under varying wind conditions the tip speed ratio should be actively controlled. To accomplish this the wind velocity and rotational speed of the wind turbine needs to be measured. During low wind speed conditions, the turbine blade operates at its optimum and during higher wind speed conditions, the pitch angle is adjusted in order to limit the aerodynamic power generated. This is referred to as pitched-to-feather [21].

The pitch adjustment of the turbine blade is mostly performed with the use of servo drives in the larger wind turbines. Unfortunately it is not a viable option to install heavy, power consuming servo drives in a small-scale, low power wind generator system. A less expensive and less power consuming method of achieving

pitch-control is possible with the use of flexible turbine blades. The pitch angle of the turbine blades is self-adjusting, as they twist and flatten out at higher rotating speeds. This method of pitch control can be referred to as passive pitch control [8]. The self-adjustment of the turbine blade is due to the flexing of the blade profile. The flexing is achieved due to the construction of the turbine blade from some composite material. The increasing rotating speed of the turbine results in an increase of centrifugal force on the wind turbine, which changes the blade shape into the feathered position which has a higher drag than the normal blade shape, thereby limiting the rotational speed and delivered power [9]. The disadvantages of passive pitch control are the financial implications, due to the use of composite material and the questionable reliability.

2.2 Connection switch-over

The stator winding of an electrical generator can be connected in different configurations, creating different characteristics. For example, as in larger conventional squirrel-cage induction motors, the motor is started with a star-connected stator in order to decrease the starting current of the motor. At the induction motor's rated speed the star-connected stator is switched-over to delta-connection to enable it to produce the rated torque of the motor.

In order to achieve some sort of passive mechanical switch-over for the AFPM generator, a centrifugal switch can be used. A centrifugal switch is a spring-loaded device connected partly to the rotor, that switches state at a certain rotating speed as the centrifugal forces overcome the force of the spring. The centrifugal switch can be used to switch the stator windings of the AFPM wind generator between series-connected and parallel-connected or a combination of the two. During lower wind speeds the generator is connected in series, where the voltage has a higher value. Thus, the AFPM wind generator will clamp to the battery voltage at a lower rotating speed. As the wind speed increases and the switch-over occurs, the parallel-connected stator winding will produce a lower phase voltage potentially lowering the load angle, δ. The load angle is the angle between the induced voltage and the phase current flowing out of the wind generator. This is advantageous as a decrease in the load angle, results in higher generator efficiency. The disadvantage associated with the use of the centrifugal switch, apart from the obvious maintenance required with mechanical switches, is the routine tensioning of the springs to insure correct operation.

It is not certain that the connection switch-over method will achieve the required maximum power point matching effect, and the non-sinusoidal current issue is not addressed.

2.3 DC-DC converter

The existing wind generator system utilises an uncontrolled rectifier which provides the power to the directly-connected battery bank. With this direct connection, the load connected to the wind generator cannot be adjusted. A dc-dc converter could be used to voltage-decouple the load from the wind generator. The dc-dc converter is connected between the rectifier and the battery bank, as shown in Fig. 2.1, to control the load connected to the wind generator, actively [4]. Thereby the maximum power point matching can be achieved.

In order for the power point matching to follow the ideal load line, the dc-bus voltage must be continually adjusted with any change in the rotating speed of the wind generator, thereby in effect regulating the wind generator's output power and maintaining the output voltage for maximum power transfer under all wind conditions [7, 22].

The disadvantages of implementing electronic converters, such as dc-dc converters, are the cost involved and the question regarding the reliability of such devices in severe conditions. The non-sinusoidal current will also still remain in the system.

2.4 Controlled rectifier

The problems associated with coreless AFPM generators in conjunction with uncontrolled rectifier-battery loads can be eliminated by replacing the uncontrolled bridge rectifier unit with a fully controlled active rectifier, as illustrated by Fig. 2.2.

During low wind speed conditions, the output voltage produced by the wind generator is not sufficient to breach the rectifier-battery bank equivalent voltage. In order to increase the wind generator output voltage the active rectifier is able to step-up the voltage so that the battery bank can be charged from a lower rotating speed. In high wind speed conditions, the controlled rectifier will clamp the output voltage of the wind generator, limiting the amount of power flowing to the battery

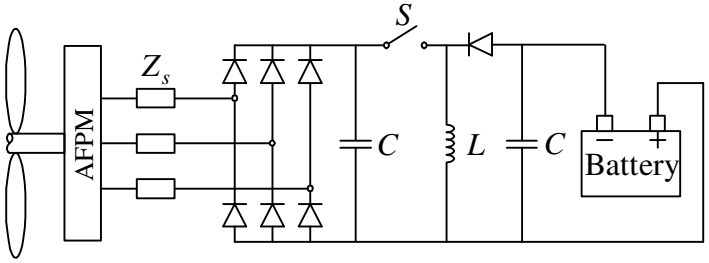

Figure 2.1: Schematic diagram showing the dc-dc converter connected to the wind generator system.

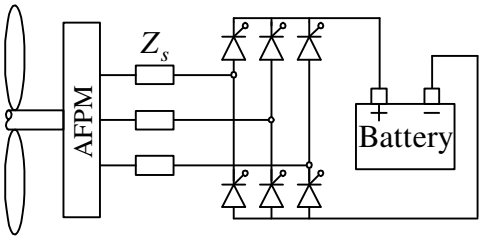

Figure 2.2: Schematic diagram showing the controlled rectifier directly connected to the wind generator system.

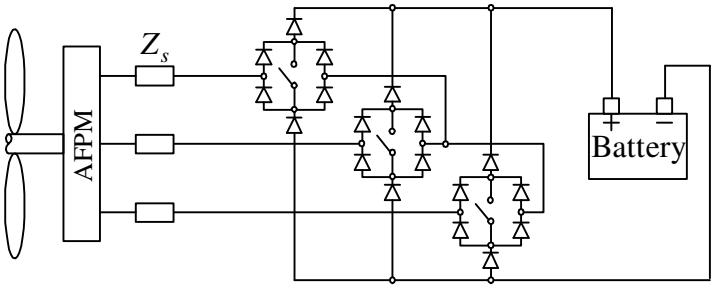

Figure 2.3: Schematic diagram showing the Vienna rectifier directly connected to the wind generator system.

bank.

This method of control not only addresses the maximum power point tracking issue of the wind generator system, but also the issue regarding the non-continuous current drawn by the directly connected rectifier-battery load. The disadvantage of the use of an active rectifier, as with most electronic converters, is that precise continuous control is necessary which increases the cost of the small-scale wind generator system [23].

2.5 Vienna Rectifier

A Vienna rectifier can be used to achieve a reduction of the line current harmonics [24]. As shown in Fig. 2.3, a Vienna rectifier has a much lower circuit complexity, consisting of only three active switches, compared to the six switches of a controlled rectifier. The reduction in switches reduces the total switching losses and improves the overall power factor of the system, compared to that of active rectifiers.

It is a highly efficient method of switching high current, making it ideal for three-phase ac-to-dc conversion at unity power factor [25]. A drawback of this control method is that it uses two diodes in series per phase instead of the one of an active rectifier, thus effectively doubling the conduction losses of the converter.

2.6 Series capacitance

In order to control the power generated by a wind generator properly, the output voltage of the wind generator needs to be controlled. To achieve this, the dc-bus should be separated from the wind generator. A series-connected capacitor could be inserted on the ac-side of the rectifier, as shown by the external impedance, Z_e, in Fig. 1.9. Now, the wind generator output voltage is not clamped by the dc-bus voltage. The capacitance is inserted into the system to lower the impedance of the system at higher rotating speeds and to increase the power transfer from the generator to the battery bank. The external capacitance is tuned to resonate with the internal inductance of the wind generator, L_i, at higher frequencies. The drawback of this topology is that the stator current is not naturally limited by the inductive reactance and therefore could exceed the current limit of the wind generator [22].

2.7 High voltage transformer

In the small-scale wind generator system, the transmission losses due to the length of connecting cable used to connect the wind generator to the three-phase rectifier, could become substantial under high wind conditions. In order to minimise the transmission losses in the connecting cable, the current flowing in the cable should be reduced by increasing the operating voltage of the wind generator if the power transferred is kept constant. To achieve this the stator winding of the wind generator is redesigned to develop a much higher voltage, i.e. 400 V at the rated speed of the wind generator. A high voltage transformer is thus required in order to still be able to use the standard 36 V battery bank.

The high voltage transformer would be connected to a variable speed wind generator, thus the resulting low rotating speed of the wind generator during low wind speed periods would necessitate the transformation of very low frequencies. Low frequency transformation would result in the need for a very large and heavy core to be used in the transformer. A rather significant benefit of this topology is the galvanic isolation between the primary and the secondary side of the transformer. The isolation is beneficial for blocking lightning surges.

It could even be possible to achieve harmonic cancellation with the use of a star-delta transformer and the correct selection of transformer vector groups. Harmonic cancellation is achieved when the transformer vector groups are so selected that current harmonics are captured in the delta-connected secondary side of the transformer and would not be induced on the star-connected primary side of the transformer [26]. The harmonic cancellation achieved only applies to triplen harmonics (3^{rd}, 9^{th}, etc.). Therefore it would have no effect on the current harmonics created by the three-phase bridge-rectifier which is of the odd, non-triplen variety

and the acoustic noise emitted by the coreless AFPM wind generator would remain. The maximum power point matching also would also not be achieved. Other factors to consider are the cost of the transformer sets and the resultant system efficiency with the addition of the transformers.

2.8 DC-transmission

The use of dc power transmission is another possible method to minimise the transmission losses in the connecting cable. With the use of dc-transmission, the reactive losses present in the connecting cable of ac-transmission systems, are eliminated. The three-phase bridge rectifier can be connected directly at the terminals of the wind generator, or the stator winding can even be manufactured with embedded diodes. But the noise and non-optimum power point matching would remain.

2.9 Twelve-pulse rectifier

As explained in the previous chapter, a six-pulse diode rectifier induces predominantly 5^{th}- and 7^{th} harmonic components in the phase current of the directly connected coreless AFPM wind generator system. With the use of a twelve-pulse diode rectifier in the place of the six-pulse rectifier, the lowest current harmonic components of the system change to 11^{th}- and 13^{th} harmonics. The higher frequency of these harmonic components could reduce the emitted noise of the wind generator. The disadvantages are that the conducting losses of the rectifier unit are doubled, while maximum power point matching is not achieved.

2.10 Passive harmonic filtering

As discussed in the previous section, the six-pulse diode rectifier causes predominantly 5^{th}- and 7^{th} harmonics in the phase currents of the wind generator system. It is possible to design a filter that would eliminate the specific harmonics that are present in the system [27]. These filters are referred to as trap filters. A trap filter can be designed to provide a low impedance path for that particular harmonic. In this particular case the 5^{th} harmonic is of highest concern. This filter would have the benefit of harmonic reduction in the phase currents resulting in lower levels of noise emitted by the wind generator. The drawback of such a steady-state method of harmonic reduction is that it functions only at a certain fixed fundamental frequency. Therefore as the rotating speed of the wind generator changes, the operating frequency changes, the fundamental frequency is not equal to the designed parameter and the trap filter is not functioning.

2.11 3rd harmonic injection

Opposed to passive harmonic filtering, harmonic injection is a method of active harmonic filtering where a measuring device is used to sample the incoming waveform and to inject harmonics into the wind generator system, in order to cancel the detrimental harmonics that were measured in the system. 3rd harmonic injection is a method of reducing the harmonic component of the current on the ac-supply side of the three-phase rectifier. This is achieved by installing a transformer on the ac-side of the rectifier and injecting a compensating current into the star-point of the transformer. By injecting a 3rd harmonic into the transformer a 3rd harmonic current is created in the secondary phase current flowing towards the rectifier. The secondary currents are reflected onto the primary currents. The 3rd harmonic current cancels the predominantly 5th- and 7th harmonic currents that already exist on the generator side [27].

The disadvantage of 3rd harmonic injection is that any change in the connected load will affect the effectiveness of the compensation of the 3rd harmonic injection system.

2.12 Harmonic mitigating transformers

Any presence of harmonic content in the wind generator system is unwanted and therefore the harmonics created by the rectifier need to be reduced. The reduction of the harmonic content can be achieved with the use of harmonic mitigating transformers. Harmonic mitigating transformers are transformers connected in different combinations in order to create phase-shifted sine waves. This method of phase shifting of the sine waves can be referred to as sine wave recombination [28]. Unlike harmonic cancellation where a reduction in the triplen harmonics in a system is achieved, harmonic mitigation could reduce the odd, non-triplen harmonics.

Phase shift transformers are implemented in the wind generator system to cancel the lower order harmonics, such as the 5th- and 7th harmonics. The harmonic mitigation is achieved by using two transformers, a star-delta and either a star-star or a delta-delta transformer. A star-delta transformer has an inherent phase shift of 30° across the transformer, where the primaries and secondaries of the star-star or delta-delta transformers are in phase with each other. The 30° phase shift causes the 5th- and 7th harmonic components of the star-delta transformer to cancel with the 5th- and 7th harmonic components of the other transformer [29].

As shown in Fig. 2.4, TX1 is a delta-delta connected transformer and TX2 is a delta-star connected transformer. The transformers are connected in parallel to the generator bus, which is connected to the wind generator. The battery bank is connected to the dc-bus, which is fed from the secondaries of the two bridge rectifiers. The process of harmonic mitigation is explained in Appendix A.

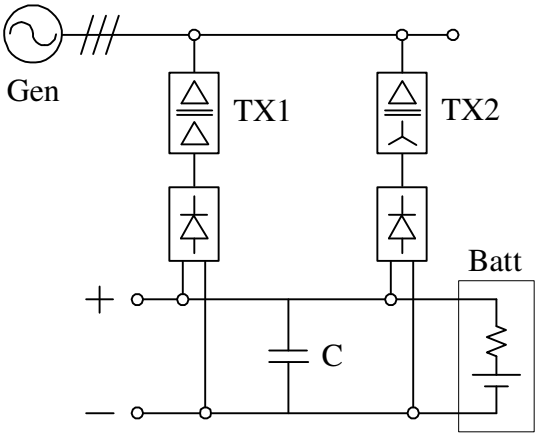

Figure 2.4: Transformer mitigation.

Harmonic cancellation will occur for the 5^{th}- and 7^{th} and the 17^{th}- and 19^{th} harmonics. The disadvantages of using this topology is that the delta-delta transformer has no ground point and the star-star transformer does not have the required delta winding in order to trap the 3^{rd} harmonic components [28]. Fortunately, the wind generator system has no need for a ground point and no 3^{rd} harmonic components are generated by the 6-pulse rectifier. Therefore harmonic mitigation will reduce the acoustic noise emitted by the wind generator system.

To implement this type of topology into the wind generator set-up, the single 6-pulse rectifier has to be replaced with two separate units. Each rectifier would be fed by a transformer, thereby effectively dividing the power of the wind generator system equally in two.

The use of harmonic mitigation would be a suitable solution for the acoustic noise concern, but does not address the maximum power matching issue. Further concerns which were not discussed are the leakage inductance caused by the transformers and power losses in the extra cabling.

Chapter 3

Theoretical analysis of the AFPM generator

In this chapter the machine that is implemented as the electrical generator in the small-scale wind generator system is analysed. The machine is an axial flux permanent magnet (AFPM) generator with an air-cored stator winding.

In an air-cored stator winding the windings are not kept in position within iron slots, but with the use of epoxy resin. Therefore, with the absence of stator teeth and the stator back yoke there is no cogging torque and no iron losses in the stator. Slotless AFPM machines can be regarded as high efficiency machines due to the absence of the rotor core losses which are normally present in the rotor back yoke and permanent magnets [30].

The AFPM machine is used in a direct-driven wind generator application which requires a low operating speed. In order to maintain frequency at low rotating speeds, high pole numbers are required [14]. The drawback of a low-speed direct-drive AFPM generator is that it requires high torque which requires a larger diameter, which affects the material cost of the machine. If the diameter of the wind generator is too large it will disturb the airflow around the turbine hub and have a negative effect on the cooling capabilities of the AFPM generator [17].

3.1 AFPM topologies

Over the years coreless AFPM machines have been developed in a number of different topologies, namely the single-sided machine, the double-sided machine with twin external stators and internal rotor and the double-sided machine with internal stator and twin external rotors.

The single-sided coreless AFPM machine has a single-sided permanent magnet (PM) rotor and a coreless stator. This creates a simple construction with no attractive forces between the rotor and the coreless stator. The disadvantage of

the single-sided topology is the low torque production capacity when compared to the double-sided variants. The double-sided AFPM machine with the inner PM-rotor has higher torque capabilities but is limited by its large effective airgap. The large airgap is due to the lack of a back-yoke for the permanent magnets. The double-sided AFPM machine with the double outer PM-rotor has the highest torque production capacity due to the higher volume of PM material used [1]. The disadvantage of the double-rotor topology is the huge attractive forces between the two opposing PM-rotor disks. These attractive forces cause a safety hazard during the machine's construction. If the rotor disks are not sufficiently thick, the disks could bend, effectively closing the airgap. Regardless of the disadvantage of the elevated cost of the increased volume of permanent magnet material, the double-sided outer-rotor topology is the coreless AFPM machine of choice for small-scale wind generator applications.

For the practical tests two different designs of double-sided outer-rotor AFPM generators were used. The differences are mainly in the rotor designs, where one is a 24-pole and the other a 32-pole machine. The 24-pole AFPM generator was used to test the principle of the new windings in the laboratory, while the 32-pole AFPM generator was used to implement the entire system practically in the field. There are slight mechanical differences in these AFPM generators, which will be discussed later in this chapter. The reason for the differences is mainly due to the availability of components in the laboratory.

3.2 Components

An AFPM generator, like all conventional electrical machines, consists primarily of a rotor and a stator. The rotor comprises of two opposing steel disks which are interconnected. The stator is of the coreless variety and is located between the two rotor disks. The rotor and stator components forming the AFPM generator can be identified in Fig. 1.7 and will be discussed briefly in the following sections.

3.2.1 Rotor

The rotor of the AFPM machine consists of two interconnected steel disks with permanent magnets attached on the outside circumference on the inner surfaces of the opposing rotor disks. The steel rotor disks are multifunctional, as the rigid steel construction maintains the necessary airgap length between the opposing magnet poles while providing the flux return path between the rotor poles [31]. As the iron losses in the rotor are very small and can for all practical reasons be neglected, the rotor disks can be manufactured from solid iron, as opposed to laminated iron [16]. The combination of the coreless stator and the permanent magnets, both having a permeability of close to unity, creates a large effective airgap. In order to maintain

acceptable values of magnetic flux within the large airgap, a much higher volume of permanent magnets is required. This has a negative effect on the mass and the manufacturing cost.

The AFPM generator was intended for use in a direct-drive wind generator application. Therefore the low rotating speed requires the AFPM generator to be optimised for low speed operation, using high pole numbers. This was done in order to avoid the need for a gearbox [13]. The disadvantage associated with the use of higher pole numbers is the inherent risk of excessive leakage flux between neighbouring permanent magnets, which is caused by the small pole pitch [16].

Magnet placement

There are mainly two possible ways of mounting the permanent magnets in AFPM machines. The permanent magnets can either be mounted on the surface of the rotor disk or they can be embedded into the rotor disk. These mounting possibilities are illustrated in Fig.'s 3.1a and 3.1b. The AFPM generators discussed in this study are of the surface-mounted topology. Surface mounting of permanent magnets is the preferred placement type due to the ease of the manufacturing of the smooth rotor disks, thereby, lowering the cost of the machine. Another advantage is that the surface-mounted permanent magnets naturally act as fans which has an ventilation effect on the stator windings at higher rotating speeds. The added cooling feature of the spinning permanent magnets allow for higher stator current densities before excessive stator winding temperatures damage or irreversibly demagnetise the permanent magnets [32].

As the direct-drive AFPM generator has a low rotating speed, the resulting centrifugal force on the magnets created by the spinning rotor is relatively low. Lower centrifugal forces allows for the permanent magnets to be glued onto the surface of the rotor disks, instead of requiring further mechanical means such as through-magnet fastening screws.

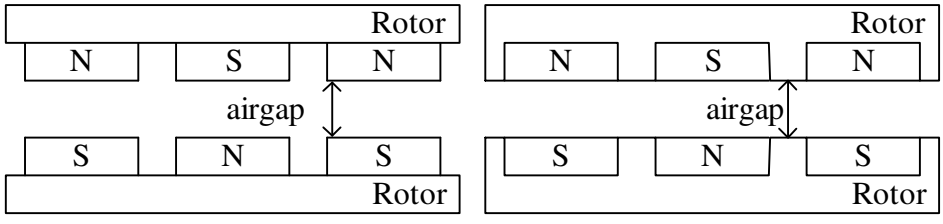

(a) Surface-mounted PM (b) Embedded PM

Figure 3.1: PM mounting types.

Pole shape

There are various different pole shapes used in AFPM machines, amongst which the rectangular-, circular- and sector shaped poles are the most popular. The two AFPM generators that are investigated utilise different pole shapes. The 24-pole generator is of the rectangular permanent magnet pole shape which is illustrated in Fig. 3.2a. The 32-pole generator's annular sector pole shape is illustrated in Fig. 3.2b. The rectangular pole shape is used in an attempt to reduce the material cost of the AFPM machine by reducing the mass and volume of permanent magnet material. The cost of the permanent magnet is further reduced as a result of the simpler manufacturing process of the rectangular shape. The other benefit of this pole shape is that the overlapping between the permanent magnet and the conductors takes place more gradually, resulting in a more sinusoidal induced EMF waveform. The disadvantage is that there is less useful flux per pole created by the rectangular pole shape. The annular sector pole shape is the most popular choice for surface-mounted AFPM machines because it produces more useful flux per pole. The permanent magnet sweeps the stator in a relative motion all along its length, creating a more rectangular flux distribution. The disadvantage is the extra mass of permanent magnet material and the associated cost of manufacturing the more complex sector-shaped permanent magnet [32].

3.2.2 Stator

In iron-cored electrical machines, the stator consists of a stack of punched laminations which forms a slotted iron core with the coils wound inside the stator slots.

In a coreless AFPM machine the stator is located between the two opposing

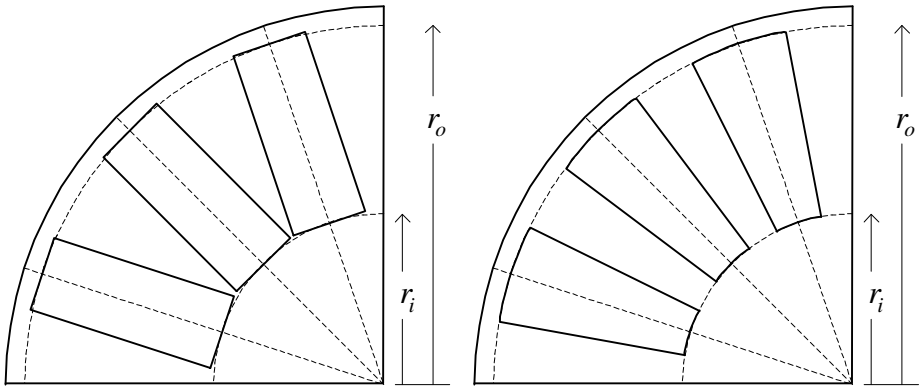

(a) Rectangular PM shape (b) Annular PM shape

Figure 3.2: Different PM shapes.

rotor disks. The coreless nature of the stator eliminates the need for lamination stamping during the manufacturing process of the stator winding [13]. This leads to a much simpler manufacturing process. The absence of an iron core for the coils of the stator winding creates a low flux density in the magnetic circuit of the coil, resulting in a low value of inductance for the coil in the coreless stator. The low phase inductance of coreless AFPM machines creates various problems, which are discussed in more detail later in this chapter.

Coil profiles

A popular coil shape for AFPM machines is the toroidal-shape coil wound around an iron core. The stator windings of the AFPM machines in this thesis are of the single-layer trapezoidal coil shape. The advantage of the trapezoidal coil shape is that it allows for the maximum coil flux linkage [32]. The trapezoidal coil shape is illustrated in Fig. 3.3. As shown, the end-winding length, l_e, indicated by the dashed line, can be of significant length compared to the active length, l_a, of the trapezoidal coil. It is obviously preferable that the end-winding length be as short as possible to minimise the resistive losses in the inactive part of the coil.

Due to the construction of the coreless AFPM machine it is possible to manufacture the stator winding of the AFPM machine with the use of preformed trapezoidal coils. The preformed coils are packed in sequence, connected accordingly and placed in the required physical position within the stator mould. The stator is cast with a composite material of epoxy resin and hardener which provides the structural support required for the flat, disk-shaped stator. The preformed coils of the coreless stator of the AFPM machine are individually bobbin-wound using round, enamel coated wire. The use of round wire is preferred in the coil due to its

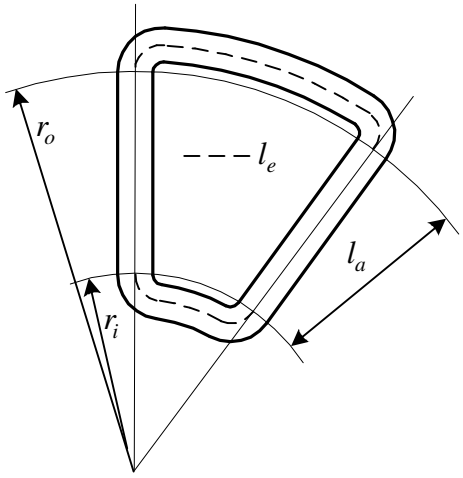

Figure 3.3: Trapezoidal coil shape.

low cost and availability, but it creates a low filling factor for the coil. The filling factor of a coil can be understood as the percentage of copper in the cross-section of a coil-side. The alternative to round wire is the use of rectangular wire. With the use of rectangular wire the filling factor of each coil would increase substantially, thereby reducing the resistance of the coil. The disadvantage of the use of rectangular conductors, apart from it being the more expensive option, is the possibility of an increase in eddy current losses in the coil.

3.3 Winding layouts

The winding topologies that are discussed in this section, are referred to in the field of electrical machines as distributed and concentrated windings. In this section the adaptation of these winding layouts to AFPM machines is discussed. In order to illustrate the differences of the two above-mentioned winding layouts, these winding layouts are discussed referring to the iron-cored radial flux machine.

The most common stator winding topology for an iron-cored radial flux permanent magnet (RFPM) machine is the distributed winding layout which comprises of normal overlapping stator coils [15]. Fig. 3.4a shows the winding sequence of a distributed winding in a RFPM machine. In order to realise the stator poles of a distributed winding, it is required that the end-windings of the different phase coils overlap each other, effectively creating long end-windings. Recent studies in radial flux machines have shown the benefit of incorporating concentrated windings in RFPM machines. Concentrated windings does not require the overlapping of the end-windings as the stator coil is concentrated around a tooth of the iron-cored stator, as shown in Fig. 3.4b. Amongst the benefits of the non-overlapping concentrated winding layout is a shorter overall axial length of the machine due to the shorter end-windings, reduced stator winding cost due to the lower number of coils and overall simpler winding structure [30]. By shortening the length of the end-windings, the volume of copper used in the stator windings is also reduced. Thus, the copper losses are reduced and the efficiency of the iron-cored non-overlapping concentrated machine is improved compared to a iron-cored machine equipped with distributed overlapping windings [33].

Therefore it is desirable to implement the non-overlapping winding configuration in coreless AFPM machines. The disadvantage of the coreless AFPM machines with normal overlapping winding, as is the case with iron-cored overlapping RFPM machines, is the long end-windings. The winding topologies of the overlapping and non-overlapping windings for an AFPM machine are illustrated in Fig. 3.5. The linearised AFPM model that is shown in Fig. 3.5 is a side view with the axial mirrored section removed. In the following section the normal overlapping and non-overlapping winding topologies as used in coreless AFPM machines are

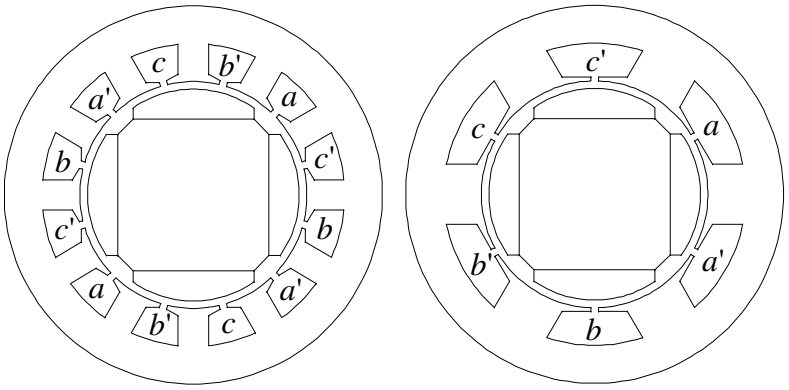

(a) Distributed winding (b) Concentrated winding

Figure 3.4: Winding topologies for radial flux machines.

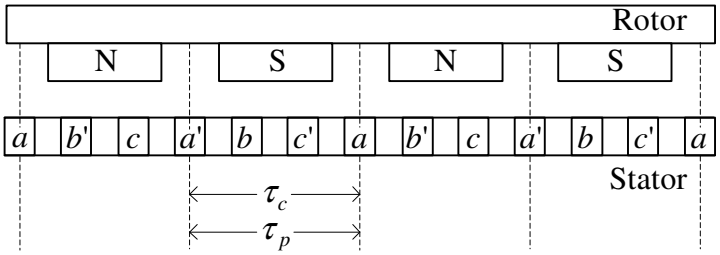

(a) Coreless AFPM overlapping winding

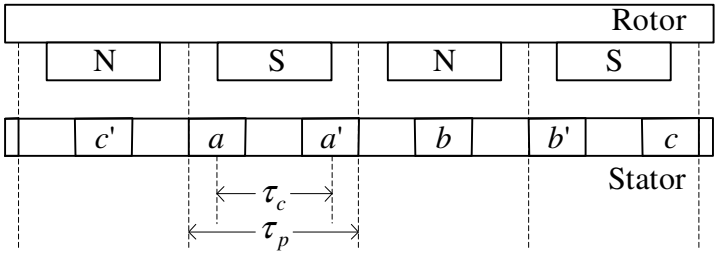

(b) Coreless AFPM non-overlapping winding

Figure 3.5: Winding topologies for axial flux machines.

discussed.

3.3.1 Coreless normal overlapping windings

The coils of the coreless normal overlapping stator winding lie next to each other in the same plane, as shown in the schematic drawing in Fig. 3.6. To ensure the correct sequence and polarities of the stator winding coils, the end-windings of the coils are required to overlap with each other. The overlapping of the end-windings

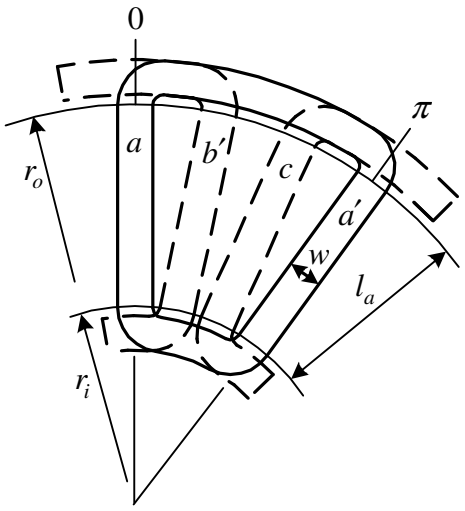

Figure 3.6: Schematic of the coreless normal overlapping winding.

Figure 3.7: 3D drawing of coreless overlapping winding.

of the coils are realised by physically bending the end-windings of the coils upwards and downwards respectively, creating the long end-windings shown by the sector of the stator winding in Fig. 3.7. The bent end-windings of the coils occupy space in the inactive part of the stator for the end-windings of the different coils to cross over each other.

From Fig. 3.5a it is shown that the overlapping winding only occupies one fictitious slot per pole per phase. A winding with one slot per pole per phase creates the ideal winding factor of 1, as the coil pitch, τ_c, and the pole pitch, τ_p, are equal.

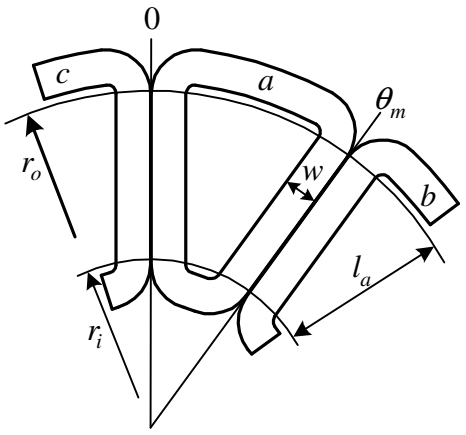

Figure 3.8: Schematic of coreless non-overlapping winding.

Figure 3.9: 3D drawing of coreless non-overlapping winding.

3.3.2 Coreless non-overlapping concentrated windings

The concentrated coils of the non-overlapping stator winding lie entirely next to each other in the same plane, as shown in Fig. 3.8. Therefore no bending of the end-windings is required during the manufacturing process, reducing the length of the end-windings and reducing the total volume of copper used. A reduction in the volume of copper results in a reduction in stator winding copper losses and an increase in machine efficiency [34]. A sector of the flat, non-overlapping windings are shown in Fig. 3.9.

As shown in Fig. 3.5b, the AFPM machine equipped with concentrated, non-overlapping windings have a fractional number of fictitious slots per pole per phase. Therefore the coil pitch, τ_c, can be calculated as only $\frac{2}{3}$ of the pole pitch, τ_p, in this case. This results in a low winding factor of only 0.866 [35]. A winding factor of less than one is created when the geometrical sum of all the winding EMF phasors is less than the arithmetical sum [36].

The result of low winding factors are machines developing lower levels of torque. Therefore, it is important that the winding factors of non-overlapping windings be increased by proper design. This can be achieved with an increased pole number and the optimal combination of pole and slot numbers [35]. As a result, non-overlapping windings are considered as mandatory in AFPM machines with high pole numbers [16].

In this study the non-overlapping winding layout can be divided into two variations, non-overlapping windings and phase-grouped windings. The non-overlapping windings has one coil per phase group ($n = 1$), while the phase-grouped non-overlapping windings has more than one coil per phase group ($n > 1$) [30]. The phase-grouped winding type is discussed in more detail in Appendix B.

3.4 Equivalent circuit

The steady-state performance of the AFPM generator is calculated with the use of an equivalent circuit in generator mode. It is sufficient to model only a single phase of an electrical generator [22]. The fundamental steady-state equivalent circuit model showing all the parameters is shown Fig. 3.10 [32].

The induced electro-motive force (EMF), which is created by the air-gap flux linkage, is represented by an ac-voltage source, E_{gen}. E_{gen} is connected in parallel with a resistor, R_{eddy}, which models the eddy current losses in the stator. This parallel combination is connected in series with a resistor and an inductor, R_i and L_i, which represents the internal impedance of the AFPM generator. The internal inductance of the generator, L_i, actually consists of the combination of mutual, leakage and end-winding leakage inductance, but it is difficult to distinguish between these inductances in a coreless AFPM machine [19]. The resultant current, I_{ac}, is chosen as flowing out of the generator model, while the voltage measured across the terminals of the generator is V_{gen}. In the following sections the parameters of the equivalent circuit are determined. This is done to calculate the performance of the AFPM machine accurately.

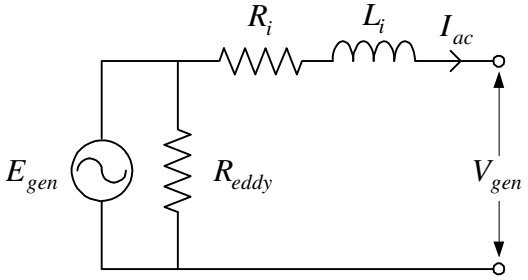

Figure 3.10: Equivalent circuit of an AFPM generator.

3.4.1 Induced phase voltage

The two types of winding structures, overlapping and non-overlapping windings, have different equations for calculating the back-EMF voltage, E_{gen}, of the generators. The RMS-value of sinusoidal phase voltage of the normal overlapping winding, E_o, can be calculated by [30]

$$E_o = \frac{q}{a}\frac{2\sqrt{2}}{p}\omega_e B_p N_t r_e l_a k_{po} \tag{3.4.1}$$

where q is the number of stator coils per phase, a is the number of parallel connected circuits, p is the number of poles, ω_e is the electrical rotating speed, B_p is the peak air-gap flux density and N_t is the number of turns per coil, r_e is the average radius of the stator winding, l_a is the active length of the stator winding and k_{po} is the pitch factor of the overlapping winding.

The number of stator coils per phase can be calculated by

$$q = \frac{Q}{3} = \frac{p}{2} \tag{3.4.2}$$

where Q is the total number of stator coils. The flux density in the airgap of the coreless AFPM machine has a trapezoidal waveform. Therefore the peak value of the fundamental component of the airgap flux density, B_p, can be calculated as

$$B_p = \frac{2\sqrt{3}B_g}{\pi} \tag{3.4.3}$$

where B_g is the dc-value of the plateau of the flux density waveform in the airgap. This can either be practically measured or estimated analytically from the demagnetisation curve of the permanent magnet material; the demagnetisation curve is also more commonly referred to as the B-H curve. The average radius of the stator winding, r_e, can be calculated by

$$r_e = \frac{r_i + r_o}{2} \tag{3.4.4}$$

where r_i and r_o are the inner and outer radii of the stator respectively. The active length of the stator winding, l_a, can be calculated by

$$l_a = r_o - r_i. \tag{3.4.5}$$

The pitch factor of the overlapping winding can be calculated by

$$k_{po} = \frac{\sin(\theta_{re}/2)}{(\theta_{re}/2)} \tag{3.4.6}$$

where θ_{re} is the coil-width-angle at radius r_e. In an AFPM machine with coreless windings the coils touch each other at a radius smaller than the inner radius, r_i, as

shown in Fig. 3.6. The point at which the coils touch each other can be assumed as $r_i - l_g$, where l_g is the length of the airgap which is measured between the opposing permanent magnets on the rotor. Therefore, θ_{re} can be calculated by

$$\theta_{re} = (\frac{r_i - l_g}{r_e})\frac{\pi}{3}. \tag{3.4.7}$$

The RMS-value of the sinusoidal phase voltage of the non-overlapping winding, E_c, can be calculated by [30]

$$E_c = \frac{q}{a}\frac{2\sqrt{2}}{p}\omega_e B_p N_t r_e l_a k_{pc} k_d \tag{3.4.8}$$

where k_{pc} is the pitch factor of the non-overlapping winding and k_d is the distribution factor. The pitch factor can be calculated by [30]

$$k_{pc} = \frac{\sin(\theta_m[1-\kappa]/2)\sin(\kappa\theta_m/2)}{(\kappa\theta_m/2)} \tag{3.4.9}$$

where

$$\theta_m = \frac{\pi p}{Q} \tag{3.4.10}$$

and

$$\kappa = \frac{\theta_{re}}{\theta_m}. \tag{3.4.11}$$

The distribution factor, k_d, can be calculated by [30]

$$k_d = \frac{\sin(n[\theta_m - \pi]/2)}{n\sin([\theta_m - \pi]/2)}. \tag{3.4.12}$$

3.4.2 Stator resistance

The phase resistance models the copper losses in the stator winding of the AFPM machine. The per-phase stator resistance, R_i, can be calculated by [30]

$$R_i = \frac{N_t^2 q \rho_t (2l_a + l_e)}{a^2 k_f h_a w} \tag{3.4.13}$$

where ρ_t is the resistivity of copper at temperature t. The average length of a turn of the winding is calculated by the term in brackets where, l_e is the end-winding length of the over- or non-overlapping windings, k_f is the filling factor, h_a is the axial height and w is the width of a coil-side. ρ_t can be calculated by

$$\rho_t = \rho_{20}(1 + 0.0039(t_c - 20)) \tag{3.4.14}$$

where ρ_{20} is the resistivity of copper at 20 °C and t_c is the operating temperature of the machine.

The end-winding length of the normal overlapping winding, l_{eo}, can be calculated by [30]

$$l_{eo} = \frac{4\pi r_e}{p} + 4l_g, \tag{3.4.15}$$

while the end-winding length of the non-overlapping winding, l_{ec}, can be calculated by [30]

$$l_{ec} = 2\theta_m(r_o + r_i)\frac{1 - 0.6\kappa}{p}. \tag{3.4.16}$$

The filling factor, k_f, is defined as the ratio of copper in the area of a coil-side. k_f was found from practice to be calculated as 0.42. The coil-side width, w, can be calculated by

$$w = 2r_e \sin\frac{\theta_{re}}{p}. \tag{3.4.17}$$

3.4.3 Stator inductance

The inductance of a phase winding consists mainly of mutual- and leakage inductances. The AFPM generator utilises a coreless stator winding topology, which results in a stator winding with a low internal inductance, L_i. The low value of the inductance is very difficult to measure accurately. Therefore, it would be advantageous to calculate the value. The derivation is discussed in further detail in Appendix C.

In the normal overlapping winding topology, the width of the coil-side, w, is roughly equal to the axial height, h_a, of the coil, as shown in Fig. C.1. Under these circumstances the Brookes coil method can be adapted for use. With the Brookes coil method the inductance of the normal overlapping winding, L_o, can be calculated by using the dimensions of the generator as [37]

$$L_o = \frac{1.699q\pi(r_o - r_i + l_g)N_t^2}{2pa}. \tag{3.4.18}$$

As described in Appendix C.2, the inductance calculation in equation (3.4.18) is not valid for the non-overlapping type winding. The reason for this is due to the coils not having the above mentioned square profile. The coil-side width of the

coil is much greater than its axial height. As a result a formula for calculating the inductance of the non-overlapping winding was adapted from the air-cored multi-layer solenoid formula. The inductance of the non-overlapping winding, L_c, can be calculated as [38]

$$L_c = \frac{q(2l_a + l_{ec})^2 N_t^2}{h_a} 10^{-7} K_n. \tag{3.4.19}$$

During operation the coil is magnetised, which results in the magnetic field no longer being uniform in the winding and therefore a correction factor, referred to as the Nagaoka constant, K_n, is required. The K_n constant can be expressed as [38]

$$K_n = \frac{1}{1 + 0.9\frac{2l_a + l_{ec}}{2\pi h_a} + 0.32\frac{2\pi w}{2l_a + l_{ec}} + 0.84\frac{w}{h_a}}. \tag{3.4.20}$$

3.4.4 Eddy current loss component

The electromagnetic losses in an electrical machine can be divided into iron losses and copper losses, where the iron losses consist of hysteresis and eddy-current losses and the copper losses consist of ohmic and eddy-current losses [17]. Due to the coreless nature of the AFPM machine there are no iron losses present in the stator core. Also, in a synchronous AFPM machine, the rotor disks rotate at the same speed as the rotating magnetic field in the stator. Therefore, the iron losses in the permanent magnets and the rotor disks can be ignored as there is no change in the flux direction in the rotor back yoke. As a result, the iron loss components for both the rotor and the stator, do not need to be modelled and are therefore ignored. The ohmic loss component of the copper losses of the stator windings is modelled by the resistor, R_i, of which the value is calculated by equation (3.4.13).

The eddy current loss component of the copper losses is created by the alternating magnetic fields in the stator winding. The alternating field is created by the permanent magnets sweeping over the conductors in the stator windings. Therefore, if the machine is operated at relatively high frequencies, the induced eddy-currents can result in substantial losses within the machine. These losses will result as an increase in the temperature of the stator windings and effectively decrease the efficiency of the machine. The effects of the eddy current losses in the stator windings, such as skin effect, are discussed in greater detail in Appendix D.

It should be noted that the eddy current loss effect can be minimised with the use of proper methods in the design of the stator conductors. In equation (D.1.1), it is shown that the skin effect eddy-current losses can be minimised by splitting the conductor into several, thin, parallel-connected strands. The dimensions of these parallel conductors should be lower than the skin depth of the conductor [18]. Unfortunately, circulating eddy currents are induced in the parallel paths. The circulating eddy currents can be minimised by twisting and transposing of the

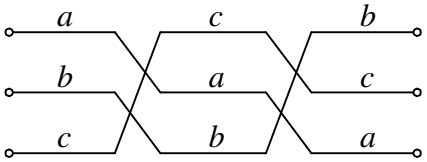

Figure 3.11: Transpositioning of stranded wire.

strands, as illustrated in Fig. 3.11. The twisting and transposing is performed so that every parallel strand occupies all the possible positions in the active length of the coil. This is due to the conductor closer to the permanent magnet experiencing a higher magnetic flux density compared to the conductor in the axial centre of the stator winding which therefore experiences higher eddy current losses [18]. From [32] it is shown that the circulating eddy currents can be greatly reduced when the bundle is twisted. It is also shown in [38] that if coils which have more than 10 turns in close proximity, transposition of these conductors is not necessary and axial twisting is sufficient to reduce the eddy-currents. Circulating currents also occur in machines with parallel-connected stator windings, but that is beyond the scope of this study.

The eddy current loss effect in an AFPM machine of this particular size is negligible due to the combination of twisting and low frequency operation. But, if the AFPM machine is to be operated at higher rotating speeds or has a higher pole number, thereby effectively increasing the operating frequency, the eddy current loss component will increase and cannot be ignored. The eddy-current losses in the AFPM stator winding, P_{eddy}, can be calculated from [18]

$$P_{eddy} = \frac{\pi l_a d^4 B_p^2 \omega_e^2 Q N_t N_p}{32\rho} \tag{3.4.21}$$

where l_a is the active length of the winding, d is the diameter of the round conductor, B_p is the peak of the flux density, ω_e is the electrical speed, Q is the total number of coils in the stator and N_t is the number of turns per coil, N_p is the number of parallel strands per conductor and ρ is the resistivity. From equation (3.4.21) it is shown that P_{eddy} is directly dependent on the 4^{th} power of the diameter of the conductor, showing the importance of the stranded conductors.

The eddy current losses in the stator winding of the AFPM machine can be modelled with the use of a resistor, R_{eddy}, which is connected in parallel with the back-EMF. The value of the resistor, R_{eddy}, can be calculated by

$$R_{eddy} = \frac{3E_{gen}^2}{P_{eddy}} \tag{3.4.22}$$

where E_{gen} is the RMS value of the back-EMF.

3.5 Analytical analysis

In this section the performance of the coreless AFPM machine is analysed.

3.5.1 Electromagnetic torque

The developed torque of the machine, T_d, can be calculated by [30]

$$T_d = k_s k_e k_r C_1 \tag{3.5.1}$$

where k_s is the stator factor, k_e is the end-winding factor, k_r is the radius factor and C_1 is a machine parameter. The stator factor of the overlapping winding, k_{so}, is calculated by

$$k_{so} = k_{po}\sqrt{\theta_{re}\frac{q}{p}} \tag{3.5.2}$$

where k_{po} is the pitch factor of the overlapping winding.

The stator factor of the non-overlapping winding, k_{sc}, is calculated by

$$k_{sc} = k_{wc}\sqrt{\frac{\kappa\pi}{3}} \tag{3.5.3}$$

where the winding factor of the non-overlapping winding, k_{wc}, is calculated by

$$k_{wc} = k_{pc}k_d \tag{3.5.4}$$

where k_{pc} and k_d is the pitch factor and distribution factor respectively of the non-overlapping winding.

To develop maximum torque in iron-cored machines, the general electrical machine winding factor, k_w, should be maximised. In a coreless AFPM machine the combination of $k_s k_e$ should be maximised to develop the maximum possible torque. This is achieved by optimising κ.

The end-winding factor of the overlapping winding, k_{eo}, is calculated by

$$k_{eo} = (2 + \delta_o)^{-\frac{1}{2}} \tag{3.5.5}$$

where δ_o is calculated by

$$\delta_o = \frac{l_{eo}}{l_a}. \tag{3.5.6}$$

The end-winding factor of the non-overlapping winding, k_{ec}, is calculated by

$$k_{ec} = (2 + \delta_c)^{-\frac{1}{2}} \tag{3.5.7}$$

where δ_c is calculated by

$$\delta_c = \frac{l_{ec}}{l_a}. \tag{3.5.8}$$

The radius factor, k_r, is calculated by

$$k_r = \sqrt{(1+\sigma_r)^3(1-\sigma_r)} \tag{3.5.9}$$

where σ_r is calculated by

$$\sigma_r = \frac{r_i}{r_o}. \tag{3.5.10}$$

The machine parameter, C_1, is calculated by

$$C_1 = r_o^2 B_p \sqrt{1.5 P_{Cu} k_f h_a / \rho_t} \tag{3.5.11}$$

where P_{Cu} is the copper losses of the machine, which is calculated by

$$P_{Cu} = 3 I_{ac}^2 R_i. \tag{3.5.12}$$

3.5.2 Copper mass

The total mass of the copper used in the stator winding of the coreless AFPM machine, M_{Cu}, can be calculated by [30]

$$M_{Cu} = k_m (2+\delta) C_2 \tag{3.5.13}$$

where k_m is the mass factor, δ is either the δ_o or δ_c of the overlapping or non-overlapping windings and C_2 is a machine constant. The mass factor is calculated by

$$k_m = \frac{(1-\sigma_r^2)\theta_{re} q}{p}. \tag{3.5.14}$$

The machine constant, C_2, is calculated by

$$C_2 = 3 r_o^2 k_f h_a \gamma_{Cu} \tag{3.5.15}$$

where γ_{Cu} is the density of copper.

3.6 Finite element analysis

In the following section the two different coreless AFPM stator winding layouts, overlapping and non-overlapping windings, are analysed using the finite element method. The phase-grouped winding layout is not discussed in the finite element model.

Finite element analysis is used to solve electro-magnetic problems. These complex problems are usually too difficult to be solved with the use of analytical or empirical methods [2]. The method of finite element analysis requires that the problem area be divided into a number of small triangles or elements, as shown in Fig's 3.12b and 3.13b for each of the different stator windings. The elements are accurately solved in the finite element analysis with the use of Maxwell's equations.

3.6.1 Model description

The magnetic field geometry in an AFPM machine varies along its radius. Thus, the finite element analysis is conducted at a radial cutting plane at the average radius, r_e. As a result the AFPM machine is analysed as a linear machine with the use of two-dimensional finite element analysis [18]. This method of analysis is implemented for both of the overlapping and non-overlapping winding layouts as both stators were designed for operation with the same AFPM rotor.

The AFPM machine has axial symmetry, therefore allowing for a two-dimensional finite element analysis to be created, modelling only one half of the machine. The centre plane in the middle of the stator mirrors the AFPM machine in the axial direction. Thus only one of the disks forming the rotor, the surface-mounted permanent magnets attached to it, one of the airgap clearances and half of the stator need to be modelled. This is achieved whilst applying the Neumann condition to the top boundary [19]. The finite element model of the overlapping winding is shown in Fig. 3.12.

It is not necessary to model the entire AFPM machine due to the symmetry in the coil groups. The symmetrical pie-slice sectors in an AFPM machine can be calculated by the pole/coil side ratio. Therefore only one pole-pitch is required for the normal overlapping winding, whilst applying negative periodic boundaries to the left and right boundaries. For the non-overlapping winding, two pole-pitches have to be modelled whilst applying positive periodical boundary conditions [30]. Fig.'s 3.12a and 3.13a shows the two-dimensional finite element models of the overlapping and non-overlapping windings respectively.

3.6.2 Flux

The finite element analysis was used to calculate the flux path in the AFPM machine. As previously mentioned, the coreless AFPM machine has a large effective airgap which is due to the lack of iron in the stator. This results in a high magnetic reluctance which prevents saturation of the magnetic circuit. In order to overcome the large airgap reluctance a high magnetomotive force (MMF) is required, resulting in higher flux density in the airgap. Thus, in the finite element model, the generated mesh needs to be denser in areas of special interest for increased

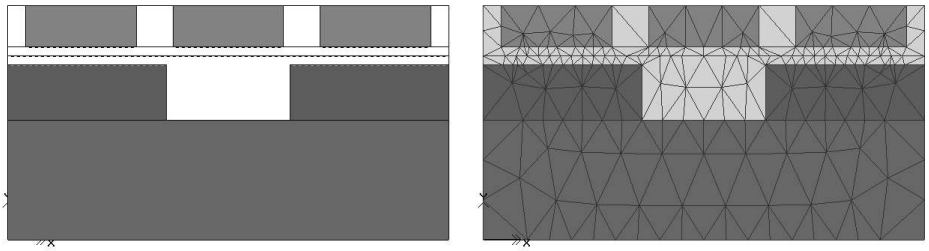

(a) Overlapping winding model (b) Model showing elements

Figure 3.12: Figures showing the finite element model and the element triangles.

(a) Non-overlapping winding model

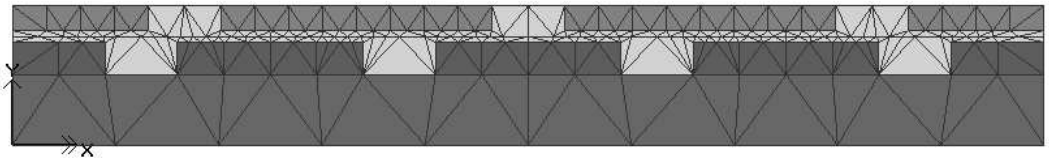

(b) Model showing elements

Figure 3.13: Figures showing the finite element model and the element triangles.

accuracy [13, 17]. Fig's 3.14 and 3.15 show the magnetic flux lines of the coreless overlapping and non-overlapping machines respectively.

In a coreless AFPM machine the effects of armature reaction, which is the demagnetising effect of the MMF created by the currents flowing in the stator winding, can be ignored due to the length of the airgap. The armature reaction is caused by the armature flux opposing the main flux, which creates a demagnetising effect. Due to the lack of armature reaction, the flux density in the rotor is constant and can be regarded as a dc-component. Thus the flux pulsations can be almost completely ignored in a coreless AFPM machine [30]. In iron-cored machines flux pulsations create additional core-losses in the rotor back yoke and permanent magnets due to changes in the airgap reluctance. In a coreless AFPM machine the combination of the ironless stator and the large airgap means that there is no change in the flux direction in the back yoke. Therefore there are no eddy-currents circulating in the permanent magnets or iron losses in the rotor. Thus, there is no need for the use of a laminated rotor or permanent magnets made up of small pieces [39].

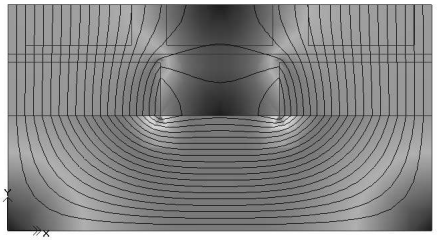

Figure 3.14: Magnetic flux lines in overlapping winding (see Fig. 3.12.

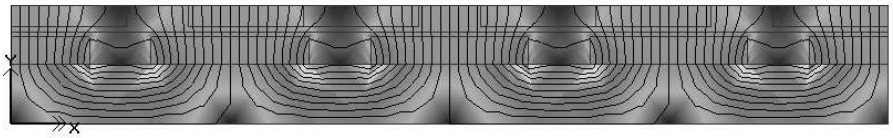

Figure 3.15: Magnetic flux lines in non-overlapping winding (see Fig. 3.13.

The flux density on a plane in the centre of the airgap is calculated in the finite element analysis. The waveform of the flux density is close to trapezoidal shape with some inherent 3^{rd}- and 5^{th} harmonic content. The 3^{th}- and 5^{th} harmonics that are present in the flux density waveform are due to the amplitudes of axial and tangential flux components varying with the air gap position [18].

In a coreless AFPM machine the flux linkage waveform is close to sinusoidal shape. The flux linkage harmonics normally created due to the presence of an iron stator core and magnetic saturation are absent. As the effects of armature reaction are ignored, the only source of flux linkage harmonics are the permanent magnets [1]. The flat-shaped permanent magnets create some 3^{rd}-, 5^{th} and 7^{th} harmonic components in the flux linkage waveform [19].

3.6.3 Back-EMF

The back-EMF can be predicted by the open-circuit magnetic field solution [14]. If a constant linear velocity is assumed for the rotational component of the AFPM machine, the back-EMF waveform can be calculated from the flux component in the finite element model. This was done for each of the winding topologies and the findings are discussed in Chapter 5.

3.6.4 Torque

The electromagnetic torque of the AFPM machine is a magnetic force in the tangential direction interacting between the rotor and the stator. The torque developed by each of the different stator winding topologies in the AFPM machine is calculated

with the use of finite element analysis. The rated current of the overlapping and non-overlapping stator windings is used in the respective finite element models to determine the torque delivered by the AFPM winding topologies. In the analysis only fundamental sinusoidal phase currents are assumed [40].

In an AFPM generator, using surface-mounted permanent magnets, the maximum torque is achieved when the angle between the current and flux linkage vectors is 90° [39].

Torque ripple

In iron-cored machines the electromagnetic torque ripple consists of cogging torque and mutual torque ripple. The cogging torque component of the torque ripple is created by the rotor flux interacting with the stator slots. The mutual torque ripple component is due to the magnetic saliency of the rotor [14].

In coreless AFPM machines the cogging torque component is non-existent due to the absence of stator slots [30]. An absence of cogging torque is very beneficial as it allows a wind generator to start rotating at very low wind speeds [34]. The mutual torque ripple in an AFPM machine is caused by the current waveform that repeats every 60°. The 60° repetition causes a 6^{th} harmonic component in the torque waveform. The 6^{th} harmonic component is created by the product of the fundamental current component and the 5^{th}- and 7^{th} harmonic components present in the airgap flux density waveform [41]. The sub-harmonic components of the torque ripple can be ignored due to the large airgap of coreless AFPM machines.

It was found that iron-cored machines that have a number of slots per pole equal to $\frac{1}{2}$ have relatively low performance and a high torque ripple. As the number of slots per pole per phase decrease the winding factor typically increases and the performance increases while the torque ripple decreases. By using the correct combination of slots and poles the low performance and high torque ripple issues normally associated with concentrated windings can be eliminated. This is done by realising the highest possible winding factor [33]. Thus, it is shown that the concentrated winding equipped iron-cored machine will have lower torque ripple compared to the distributed winding equipped iron-cored machine [39].

Magnetic noise

Axial forces are by far the most dominating source of magnetic noise in iron-cored AFPM machines. The attractive magnetic force is in the axial direction between the rotor and the stator. If these axial magnetic forces in the AFPM machine are not symmetrical, the resulting magnetic force will vibrate the stator and generate an acoustic noise [36, 39, 42]. The sound level of this noise depends on the rigidity of the machine. Relatively low vibration frequencies can coincide with the natural frequency of the machine structure and result in resonance. This is particularly the

case in higher pole number machines which tend to have thinner back yokes that can easily act as undesired loudspeakers [43].

In coreless AFPM machines this is not of concern. However, the current that flows in the coreless stator winding causes an axial magnetic force on each half of the coil. Normally the axial forces on each side of the stator winding cancel each other out. This causes a concern that if the stator winding is not located precisely on the centre plane between the two rotor disks, these axial magnetic forces on each side will not cancel each other out. The magnetic forces would result in an unbalanced force on the stator which could cause vibration of the stator winding [32]. Upon examination of the magnitude and frequency of the magnetic forces they were found to be of the 3^{rd} harmonic order and not of the odd, non-triplen harmonic orders as have been identified in this thesis as the harmonic orders responsible for the acoustic noise.

Chapter 4

Analysis of proposed system

In this chapter the specifications and requirements of the wind generator power system for direct battery charging applications are analysed. The purpose of the analysis is to achieve better matching between the wind turbine, wind generator and the power system, which will yield higher overall performance.

As discussed in the first chapter, the wind power system consists of the wind turbine which is directly connected to the AFPM wind generator. The wind generator is connected to the three-phase diode bridge rectifier unit, with the use of an armoured cable. In a direct battery charging application the rectifier is directly connected to the battery bank which is used for storage of the generated power. These components are illustrated in Fig. 1.9. The main disadvantage of direct battery charging is that maximum power from the turbine under variable wind speed conditions is not obtained and is largely affected by the internal impedance of the generator, Z_i, and to some extent the impedance of the cable, Z_c. The connecting cable has a certain impedance that has an influence on the wind power system and therefore should not be ignored. The power obtained thus depends very much on the design and the characteristic-impedance of the generator [44].

There are a couple of issues regarding the use of a low-impedance coreless AFPM generator in a direct battery charging system. Amongst these are the non-optimal turbine power matching and the non-sinusoidal line currents created due to the use of the diode rectifier. The harmonic line currents created by the non-linear load that is connected, cause the AFPM generator to emit a severe acoustic noise under loaded conditions. The noise can be rather annoying to persons and livestock in the vicinity of the operating wind generator. In the setup that is currently implemented, good turbine power matching is obtained at higher wind speeds, while no power is generated at the frequently occurring lower wind speeds. In order to obtain high annual energy capture, the wind generator system requires a high system efficiency at the low wind speeds as those are the conditions under which the system operates most of the time. Therefore the ideal would be for the wind generator to follow the optimum power points of the wind, as indicated by the dotted peak power points

in Fig. 1.8.

In order to provide a more accurate wind turbine power matching and to reduce the harmonic line current components of a coreless AFPM generator direct battery charging system sufficiently, the effects of adding external series inductors, L_e, to the ac-side of the rectifier are investigated [44].

4.1 Theoretical analysis

In this section the direct battery charging wind power system is analysed in order to predict its performance capabilities. An electronic battery charging controller is normally connected just before the battery bank and is used to control the rate of charge of the battery bank. The controller is only active during high states of charge of the battery and is otherwise inactive, therefore for the purpose of analysis, the dynamics of the controller was ignored. In this study battery charging dynamics are not considered. The aim is to achieve maximum performance from an AFPM wind generator for direct uncontrolled battery charging applications.

The equivalent circuit of the wind power system incorporates the equivalent circuit of the AFPM generator, a description of which is given in the previous chapter. The steady-state per-phase equivalent circuit diagram of the wind generator system is shown in Fig. 4.1.

The wind turbine is directly connected to the wind generator and generates a mechanical torque, T_m, at a mechanical rotating speed of ω_m. The wind generator system equivalent circuit consists of the generator EMF, E_{gen}, in series with the internal resistance and inductance, R_i and L_i, of the AFPM wind generator. The voltage at the terminals of the wind generator is indicated by V_{gen}. The wind generator is connected to a three phase bridge rectifier through the proposed external inductor, with its inductance, L_e, and resistance, R_e. The terminal voltage on the

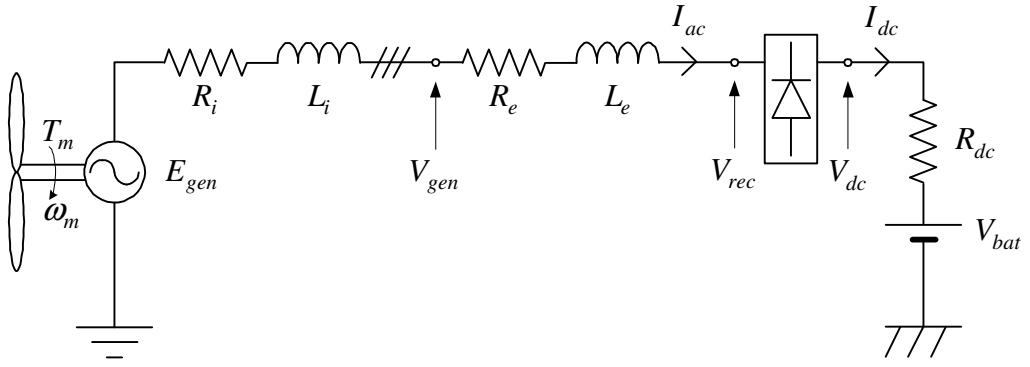

Figure 4.1: Per-phase equivalent circuit diagram of the wind generator system.

ac-side of the rectifier is indicated by V_{rec}. As is described in Appendix E.6, the battery bank model consists of the battery's internal resistance, R_{dc}, connected in series with the open-circuit dc-voltage source, V_{bat}, of the battery bank. The battery bank is directly connected to the rectifier. The voltage on the dc-side of the rectifier is the battery terminal voltage or more commonly referred to as the dc-bus voltage, V_{dc}. The ac- and dc-currents which flow in the system are indicated by I_{ac} and I_{dc}, respectively.

In order to analyse the steady-state behaviour of this circuit, the non-linear rectifier-battery load was replaced by an ac-equivalent linear load. The ac-equivalent of the rectifier-battery load is represented by an ac-voltage source, V_b, representing the battery-bank, and a series resistance, R_{ac}, representing the internal resistance of the battery bank. The fundamental RMS phase ac-equivalent voltage of the battery, V_b, can be calculated by

$$V_b = \frac{\sqrt{2}(V_{bat} + 2V_d)}{\pi} \tag{4.1.1}$$

where V_d is the forward conducting voltage drop across a diode in the bridge rectifier [45]. Therefore, the ac-voltage of the wind generator is equal to the combination of the open-circuit dc-voltage of the battery and the forward-conducting voltage of the bridge rectifier. The frequency of V_b is fixed to the operating frequency E_{gen} of the generator [7, 22]. The internal resistance of the battery, R_{dc}, is converted to the ac-equivalent internal resistance of the battery, R_{ac}, as

$$R_{ac} = \frac{6R_{dc}}{\pi^2}. \tag{4.1.2}$$

The ac-equivalent per phase equivalent diagram is shown in Fig. 4.2. The ac-equivalence of the battery model is discussed in more detail in Appendix F.

From the ac-equivalent circuit in Fig. 4.2, a phasor diagram representation of the wind generator system is shown in Fig. 4.3. In this analysis the AFPM wind

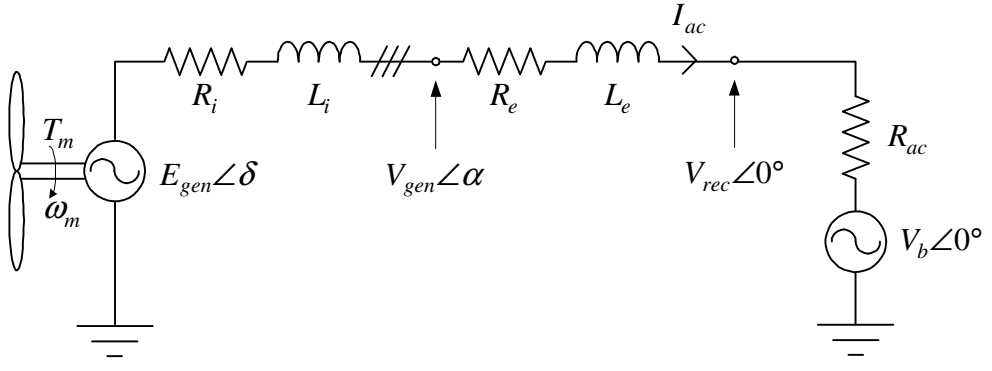

Figure 4.2: Per-phase ac-equivalent circuit diagram of the wind generator system.

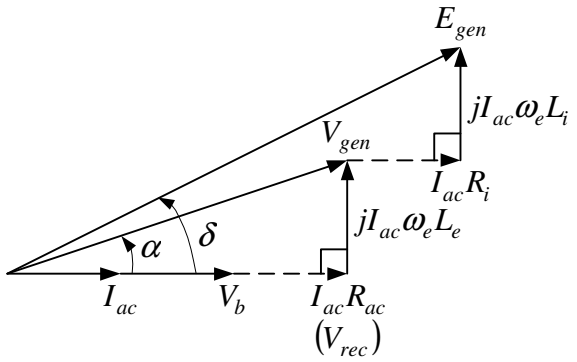

Figure 4.3: Phasor diagram of the wind power system.

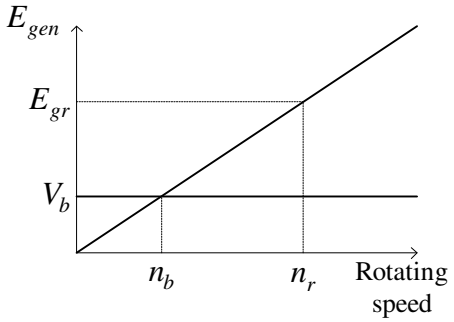

Figure 4.4: Back-EMF voltage at base speed ad rated speed.

generator is investigated as part of the wind power system, therefore the rectifier voltage, V_{rec}, is the reference. In the wind power system the phase current, I_{ac}, is in phase with the rectifier voltage, V_{rec}, and lags the back-EMF voltage. Thus, the ac-equivalent of the battery load, V_b, is in phase with the phase current resulting in $\theta = 0°$ and unity power factor of the system. The angle measured between the generator voltage, E_{gen}, and the line current, I_{ac}, is referred to as the wind generator system load angle, δ, while the angle measured between generator terminal voltage, V_{gen} and the line current, I_{ac}, is referred to as the phase angle, α.

The induced back-EMF of the synchronous AFPM generator, E_{gen}, is a function of the rotating speed and the magnetic flux in the airgap, as described by equations (3.4.1) and (3.4.8), respectively. As shown in Fig. 4.4, the generated voltage, E_{gen}, is equal to the ac-equivalent battery voltage, V_b, at the base rotating speed n_b. At the rated rotating speed of the wind generator, n_r, the generated voltage, E_{gen}, is equal to the rated generator voltage, E_{gr}.

4.2 Maximum power point matching

In this section a formula is derived to calculate the value of external inductance, L_e, which would provide close to maximum power point matching.

It is of utmost importance that the power curves of the wind turbine and of the wind generator used, are matched. If power matching is not achieved, the expected power levels will not be reached. The maximum power points at each particular wind speed are indicated on the wind turbine power graph in Fig. 1.8. From this it can be observed that the wind generator does not start delivering power to the battery load until the reverse bias of the diodes that are imposed by the battery voltage, is reached. The dc-bus voltage, V_{dc}, determines the frequency at which the generator starts delivering power to the battery bank. Therefore, a reduction in the value of the dc-bus voltage will result in a reduction of the wind generator cut-in speed [7].

A simplified graph of the maximum power point curve is shown in Fig. 4.5. In this simplified graph, two operating points, b and r, are selected on the maximum power point curve. Operating point b is chosen at the desired cut-in speed, n_b, of the system, while operating point r is at a selected rated power of the turbine, P_{tr}, developed at rated speed, n_r. The latter speed should be at the highest wind speed likely to occur. Note that r is a fixed operating point that is dependent on the specific wind turbine used. Operating point b will be chosen in the region of maximum turbine power at low wind speeds, which is also wind turbine specific [44].

It is necessary to calculate the required value of L_e to guide the delivered power curve to plot through the two operating points, b and r. The simplified ac-equivalent circuit diagram consists of a series connected circuit, where the elements are grouped, as shown in Fig. 4.6. The per-phase system inductance, L_s, and resistance, R_s, consist of

$$L_s = L_i + L_{cc} + L_e \tag{4.2.1}$$

and

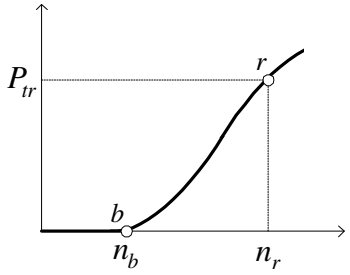

Figure 4.5: Simplified graph of the power matching showing operating points b and r.

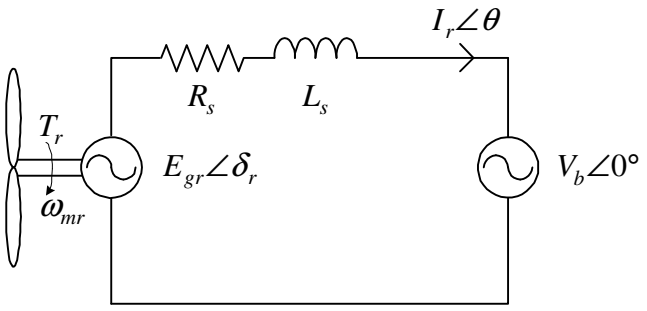

Figure 4.6: Simplified equivalent circuit diagram of the system.

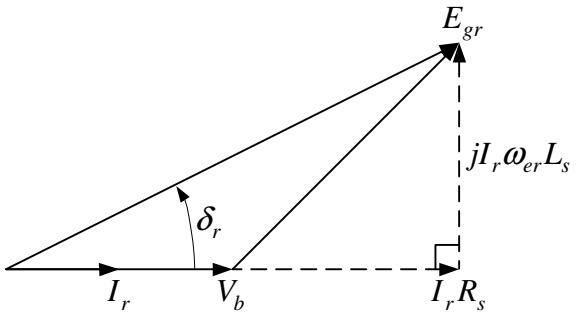

Figure 4.7: Simplified phasor diagram of the wind power system.

$$R_s = R_i + R_{cc} + R_e + R_{ac} \tag{4.2.2}$$

where R_{cc} and L_{cc} are the per-phase resistance and inductance, respectively, of the cable used to connect the generator to the rectifier-battery load. L_e is the per-phase inductance of the external inductor, which, in practise, has some built-in resistance which is represented by R_e. Under all of the above-mentioned conditions, the line current in the system, I_{ac}, is the rated current flowing in the system, I_r. Under rated conditions the electrical speed of the system is ω_{er}, while the rated load angle is δ_r. The corresponding phasor diagram for this simplified circuit diagram is shown in Fig. 4.7.

The rated output voltage of the wind generator, E_{gr}, at the rated speed, n_r, is a function of the cut-in speed of the generator, n_b, and can be calculated by

$$E_{gr} = V_b \frac{n_r}{n_b}. \tag{4.2.3}$$

From the operating point r on the wind turbine power curve, the rated torque delivered by the wind turbine, T_r, can be calculated by

$$T_r = \frac{P_{tr}}{\omega_{mr}} \tag{4.2.4}$$

where P_{tr} is the rated turbine power and ω_{mr} is the rated mechanical speed which can be calculated by

$$\omega_{mr} = \frac{\pi n_r}{30} \tag{4.2.5}$$

while

$$\omega_{er} = \frac{p\omega_{mr}}{2}. \tag{4.2.6}$$

In a coreless AFPM wind generator the core losses are non-existent and the wind-and-friction losses are assumed to be negligibly small, therefore the rated turbine power, P_{tr}, can be calculated from Fig. 4.6 as

$$P_{tr} = 3E_{gr}I_r \cos\delta_r \tag{4.2.7}$$

where from Fig. 4.7

$$\cos\delta_r = \frac{V_b + I_r R_s}{E_{gr}}. \tag{4.2.8}$$

From equations (4.2.7) and (4.2.8) the rated current, I_r, can be calculated by

$$\begin{aligned} P_{tr} &= R_s I_r^2 + V_b I_r \\ I_r &= \frac{\sqrt{V_b^2 + \frac{4}{3}R_s P_{tr}} - V_b}{2R_s}. \end{aligned} \tag{4.2.9}$$

From equations (4.2.1), (4.2.3), (4.2.5) and (4.2.6) the value of the external inductance, L_e, required in order for the wind turbine power graph to pass through both operating points b and r, can be calculated by

$$L_e = \left(\frac{60V_b}{\pi p n_b}\right)\frac{\sin\delta_r}{I_r} - L_{cc} - L_i. \tag{4.2.10}$$

In this power system, the output power has to be limited at speeds above the rated turbine rotating speeds to ensure that the current limit of the wind generator is not exceeded. This is realised by the resistive losses in the wind generation system and the increasing impedance due to the increasing operating frequency of the wind generator through the external inductor, L_e. The increase in system impedance restricts the obtained power levels to within the cooling limitations of the AFPM wind generator.

4.3 Analysis under rated conditions

In this section the wind generator system, shown in Fig. 4.8, is analysed under rated conditions.

As discussed in Appendix F, the dc-current charging the battery bank, I_{dc}, can be calculated by

$$I_{dc} = \frac{3\sqrt{2}}{\pi} I_r, \tag{4.3.1}$$

where I_r is the rated phase current on the ac-side of the rectifier. The dc-bus voltage on the dc-side of the rectifier, V_{dc}, can be calculated by

$$V_{dc} = V_{bat} + I_{dc} R_{dc}, \tag{4.3.2}$$

where V_{bat} is the open-circuit voltage of the battery bank and R_{dc} is the internal resistance of the battery bank. The efficiency of the entire wind generator system, η_{sys}, can be calculated by

$$\eta_{sys} = \frac{P_{dc}}{P_{tr}} \times 100\% \tag{4.3.3}$$

where P_{dc} is the power delivered to the battery bank under rated conditions and can be calculated by

$$P_{dc} = I_{dc}(I_{dc} R_{dc} + V_{bat}). \tag{4.3.4}$$

The power dissipated in the bridge rectifier can be calculated by

$$P_d = 2 V_d I_{dc} \tag{4.3.5}$$

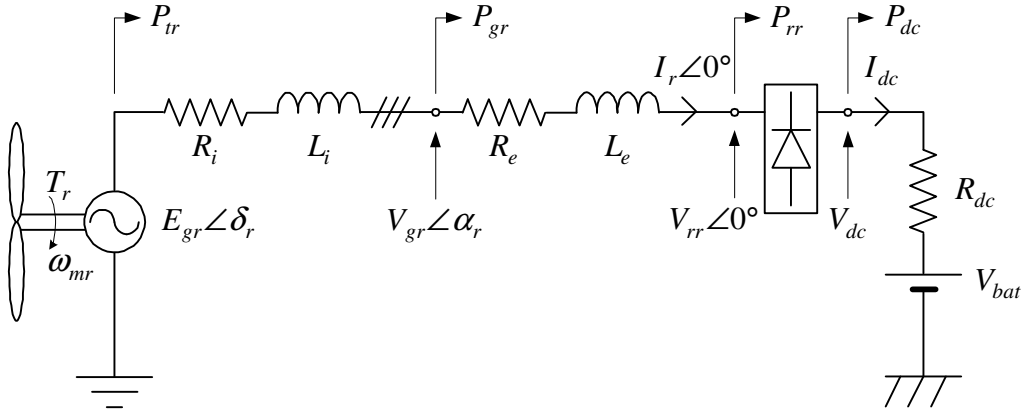

Figure 4.8: Equivalent circuit of the wind power system.

where V_d is the forward conducting voltage of the diodes in the rectifier. The power at the rectifier under rated conditions, P_{rr}, can be calculated by

$$P_{rr} = P_d + P_{dc} \tag{4.3.6}$$

and

$$P_{rr} = 3V_{rr}I_r \tag{4.3.7}$$

as $\theta_r = 0°$.

From equations (4.3.1), (4.3.2) and (4.3.5) - (4.3.7), the rated fundamental RMS phase voltage at the terminals of the ac-side of the bridge rectifier, V_{rr}, can be calculated as

$$V_{rr} = \frac{\sqrt{2}}{\pi}(V_{dc} + 2V_d). \tag{4.3.8}$$

The efficiency of the AFPM wind generator under rated conditions, η_{gr}, can be calculated by

$$\eta_{gr} = \frac{P_{gr}}{P_{tr}} \times 100\% \tag{4.3.9}$$

where the rated wind turbine power, P_{tr}, can be calculated from equation (4.2.7) and the rated wind generator output power, P_{gr}, can be calculated by

$$P_{gr} = 3V_{gr}I_r \cos\alpha_r. \tag{4.3.10}$$

4.4 Harmonic current analysis

It was found that the current harmonics in the wind generator system are a function of the value of system inductance and a function of the difference between the generated voltage of the wind generator and ac-equivalent voltage of the battery bank. It was also found that the current harmonics are independent of frequency, in this particular operating frequency range.

As previously discussed, to lower the voltage difference between the wind generator and the battery bank an electronic controller can be installed which will monitor and actively control the battery bank voltage. This will, to a certain extent, limit the current harmonics in the system. The other method, which was followed in the previous section, was to increase the generated voltage of the wind generator by designing a new stator winding, in conjunction with an inductor. This combination was used to achieve the maximum power matching and suppress the harmonic content of the current.

4.4.1 Harmonic order

In the wind generator system the rectifier-battery load creates non-sinusoidal current waveforms on the ac-side of the rectifier. The current harmonics are due to the non-linear relationship between the voltage and the current in circuits with diode rectifiers [46]. The order of these current harmonics, produced by a three-phase rectifier with six-pulse switching characteristics, can be calculated by [47]

$$h = 6k \pm 1 \tag{4.4.1}$$

where h is the order of the harmonics and k is any integer. From equation (4.4.1), the harmonic components are calculated as the 5^{th}, 7^{th}, 11^{th}, 13^{th}, etc. harmonics, with the 5^{th} harmonic being the most dominant. These non-triplen current harmonics are responsible for the acoustic noise that is emitted from the wind generator.

4.4.2 *dq*-analysis

In this section a value of the external inductance, L_e, is calculated that will, instead of achieving passive maximum power point matching, minimise the harmonic content of the current to within predefined limits.

In the wind generator system, the wind generator can be regarded as the power source whilst the bridge rectifier is the harmonic source. The simplified equivalent circuit that is presented in Fig. 4.6, can be modified to represent the circuit used for the *dq*-analysis in Fig. 4.9.

The power source is the AFPM generator which is represented by the fundamental value of the back-EMF, E_{g1}. The power source is connected to the phase resistance, R_s, and the system inductance, L_s, resulting in the fundamental component of the phase current, I_1. The harmonic source is represented by the fundamental component of the ac-equivalent battery voltage, V_{b1}.

From Fig. 4.9, the *dq*-transformation could be achieved. The *dq*-analysis is performed with the purpose of transforming the time-varying variables, such as the

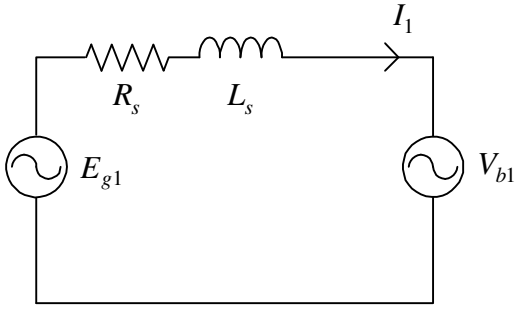

Figure 4.9: The fundamental equivalent circuit diagram.

voltage and currents of the wind generator system, into dc-values [20]. The ABC-parameters of the voltage and the current were transformed to the $dq0$-reference frame at a base frequency equal to the 5$^{\text{th}}$ harmonic frequency. That results in the 5$^{\text{th}}$ harmonic current in the system being transformed to direct current. The ABC - $dq0$ transformation is discussed in Appendix G.1.

The parameters of the dq-equivalent circuit, such as the 5$^{\text{th}}$ harmonic d- and q-axis speed dependent back-EMF can be calculated as [19]

$$E_{d5} = -\lambda_{q5}\omega_5 \tag{4.4.2}$$

and

$$E_{q5} = \lambda_{d5}\omega_5 \tag{4.4.3}$$

where

$$\lambda_{d5} = L_d i_{d5} \tag{4.4.4}$$

and

$$\lambda_{q5} = L_q i_{q5} \tag{4.4.5}$$

where λ_{d5} and λ_{q5} are the 5$^{\text{th}}$ harmonic d- and q-axis flux linkage respectively, ω_5 is the electrical rotating speed, L_d and L_q are the d- and q-axis phase inductance, respectively and i_{d5} and i_{q5} are the 5$^{\text{th}}$ harmonic d- and q-axis phase currents, respectively.

From equations (4.4.2) - (4.4.5), the steady-state d- and q-axis 5$^{\text{th}}$ harmonic equivalent circuits can be developed, as shown in Fig.'s 4.10 and 4.11, respectively.

From Fig.'s 4.10 and 4.11, the 5$^{\text{th}}$ harmonic d- and q-axis currents, i_{d5} and i_{q5}, can be calculated by [G.2]

$$i_{d5} = \frac{\omega_5 L_d v_{q5}}{R_s^2 + \omega_5^2 L_d^2} \tag{4.4.6}$$

and

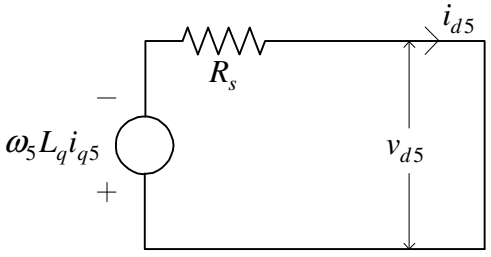

Figure 4.10: The 5$^{\text{th}}$ harmonic d-axis equivalent circuit diagram.

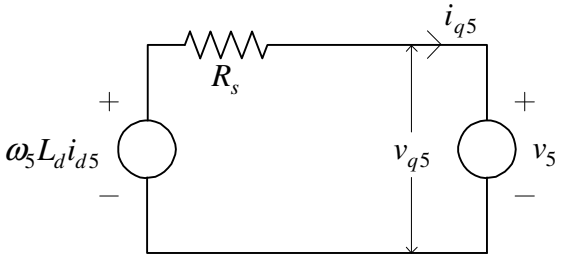

Figure 4.11: The 5th harmonic q-axis equivalent circuit diagram.

$$i_{q5} = -\frac{v_{q5}}{R_s + (\frac{\omega_5^2 L_q^2}{R_s})}. \tag{4.4.7}$$

In the dq-model of a conventional machine, the rotor reference frame will have the magnetic flux in the d-axis direction while the q-axis leads by 90° electrical, as the machine is the reference point [41]. In this analysis the rectifier-battery load is the harmonic source, therefore, the rectifier terminal voltage, V_{rec}, is taken as reference. The 5th harmonic q-axis voltage, v_{q5}, is a function of the rectifier terminal voltage, V_{rec}. Therefore, v_{q5} can be calculated by [G.3]

$$v_{q5} = \frac{\sqrt{2}V_{rec}}{5} \tag{4.4.8}$$

where

$$V_{rec} = \frac{V_b + \sqrt{V_b^2 + \frac{4}{3}P_{rec}R_{ac}}}{2} \tag{4.4.9}$$

where V_b is ac-equivalent of the battery voltage calculated in equation (4.1.1), P_{rec} is the rectifier power and R_{ac} is the ac-equivalent internal resistance of the battery calculated in equation (4.1.2).

As the 5th harmonic of the current is the most dominant harmonic, the value of system inductance, L_s, can be calculated that will be required to limit the 5th harmonic current in the wind generator system. It can be assumed that $L_s = L_d = L_q$ as the coreless AFPM machine has surface mounted permanent magnets creating negligible magnetic saliency [16, 41]. The value of the d-axis inductance, L_d, can be calculated by [G.4]

$$L_s = L_d = \frac{v_{q5} + \sqrt{v_{q5}^2 - 4i_{d5}^2 R_s^2}}{2i_{d5}\omega_5} - L_{cc} - L_i \tag{4.4.10}$$

where the value of i_{d5} should be kept to within 5% of I_{ac}, calculated in equation (4.2.9), to achieve the required harmonic supression.

4.4.3 Acoustic noise analysis

In this section the effects of the harmonic currents on the acoustic noise are investigated. The harmonic currents are due the direct relationship between the acoustic noise emitted by the wind generator and the wind generator loading conditions [48]. The noise emission associated with wind generators is a major concern and needs to be investigated.

In the field of electrical machines there are primarily four types of noise, magnetic, mechanical, electronic and aerodynamic noise. The magnetic noise is minimised by ensuring symmetrical axial forces in the stator windings. The mechanical noise which is created by wind turbines is restricted with the use of relatively low tip speed ratios and modern advances in turbine blade trailing edge and tip design [49]. The electronic noise can be ignored since the wind generator system does not make use of any electronic controllers. The aerodynamic noise from the AFPM generator is also negligibly small due to the low rotating speed of the wind generator.

The source of the acoustic noise is the presence of the harmonic components in the line current. These current harmonics are due to the use of the non-linear rectifier-battery load. The combination of the magnetic forces created by the current harmonics, together with the inherent natural frequency of oscillation of the mechanical structure of the AFPM generator, creates a mechanical vibration resulting in acoustic noise [50]. This is due to the natural frequency of the mechanical structure which coincides with the frequency of the emitted sound waves [51]. The inherent natural frequency of the machine is determined by the parameters of the mechanical system [52]. Thus, by changing, for example, the thickness of the rotor yoke, the natural frequency of that component can be changed. That change in natural frequency of the component will possibly no longer coincide with the frequency of the vibration, which will result in a decrease of the acoustic noise. The disadvantages of stiffening the machine structure are the added mass and resulting cost to the system.

In the previous section methods were derived for restricting the harmonic content of the current to within predefined limits. When the harmonic content are within these limits the wind generator's emitted noise should be inaudible over the existing wind noise.

The acoustic noise measurements were performed in the range that is audible to the human ear. The human ear has an audible range of between 20 Hz and 20 kHz, but is most sensitive to sounds in the frequency range of 1 - 5 kHz. As a result, measuring equipment incorporates an A-weighting filter, which replicates the filtering process of a human ear [51]. Sound pressure levels are normally measured in the unit decibel (dB). When an A-weighting filter is used, the sound pressure levels are measured in units of dBA. The measurement device that was used for the practical tests had a built-in analogue-to-digital converter which has a full-scale

deflection of 1 V. Therefore, it is convenient to measure sound levels in decibel-Volts (dBV). All tests were performed using this scale for comparison purposes.

Chapter 5

Simulated and measured results

In this chapter the uncompensated wind generator system is investigated and an improved system is developed. The development is performed with the use of the analysis in the previous chapter, compared to simulations and finally confirmed with practical results. The practical tests were performed on a test set-up at Stellenbosch University's Electrical Machines Research Laboratory.

5.1 Practical test station

The test set-up consists of a variable speed drive (VSD) controlling the power to a 4-pole asynchronous motor. The motor is used as the prime mover for the wind generator in order to emulate the mechanical characteristics of the wind turbine. The input power to the wind generator is measured with the use of a torque sensor, while the output power is measured using a variety of different techniques. Fig. 5.1 shows the AFPM wind generator connected to the drive motor.

5.2 Commercially available wind generators

There are a couple of small-scale, stand-alone wind generators that are available for purchase on the South African market. The wind generator that was designed and built at Stellenbosch University will be compared to, and evaluated against, a popular competitor unit.

The competitor unit is a radial flux, horizontal-axis wind generator, which has a maximum power rating of 1.2 kW. The radial flux generator has the stator windings wound inside the slots of the steel stator. The single-sided rotor is constructed with the permanent magnets surface mounted to the inside of the rotor yoke.

The advantages of the competitor unit is its very competitive pricing which results in excellent value for money. The disadvantage, as with all iron-cored permanent magnet machines, is the inherent torque ripple and the possibility of high

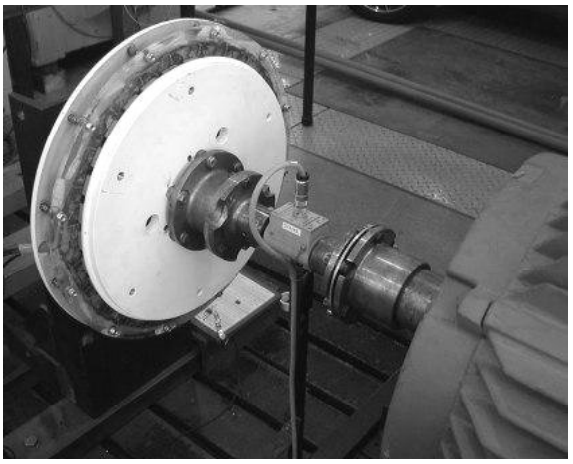

Figure 5.1: Laboratory test setup.

cogging torque. A further possible disadvantage of this type of wind generator is non-optimal power matching which is due to the fixed value of system inductance, L_s. The fixed value of L_s is as a result of the iron-cored stator creating the high value of the internal inductance, L_i. The high value of L_i leaves little room for finer adjustment of the value of L_s in order to obtain closer to optimal power point matching.

5.2.1 Equivalent circuit

In this section the electrical parameters of the equivalent circuit of the competitor unit are discussed.

The internal resistance of the competitor unit, R_i, was calculated by applying a dc-voltage across two phases of the stator winding and the resultant current measured after the steady-state temperature had been reached. This method was needed as the wind generator does not have an external star-point. From this, with the use of Ohm's Law, the internal resistance was calculated and tabulated in Table 5.1. For the purpose of comparison all the tests were performed at the same mechanical rotating speed of 200 rpm. The rotating speed was chosen as the fixed parameter for the tests, as the different machines were intended for wind generator applications using the same wind turbine.

During the open-circuit test the unloaded wind generator was driven at its rated mechanical rotating speed. This was done to establish the value of the back-EMF of the synchronous generator, E_r, at rated speed, as shown in Fig. 5.2a. As explained in previous chapters, a synchronous machine has a fixed relationship between the back-EMF and its frequency. Due to this relationship the pole number, p, can be calculated as

Table 5.1: Wind generator data

Design data	*Competitor*	*Uncompensated*	*Improved*
Flux direction	RFPM	AFPM	AFPM
Number of poles p	30	24	32
Rotating speed n_r, rpm	200		
Rated frequency f_r, Hz	50	40	53.3
Back-EMF E_r, V	28.3	22.9	45.9
Internal resistance R_i, mΩ	375	175	680
Internal inductance L_i, mH	5.07	0.2	0.65
Cut-in speed n_b, rpm	100	135	75
Rated turbine power P_{tr}, kW	0.57	0.74	1.19
Rated output power P_{dc}, kW	0.49	0.63	0.74
System efficiency η_{sys}, %	86	84	62

$$p = \frac{120 f_r}{n_r} \tag{5.2.1}$$

where f_r is the frequency of the rated electrical speed and n_r is the rated mechanical rotating speed of the wind generator. It should be noted that as this particular wind generator has no external star-point, the measured line values had to be converted to phase values for the equivalent circuit analysis. The measuring equipment being used creates a virtual star-point so that the analysis and tests can be performed with phase values.

Like with the open-circuit test, the short-circuit test was also performed at the rated speed in order to establish the short-circuit phase current of the wind generator, I_{sc}. The three terminals of the wind generator were shorted and the short-circuit current flowing in the phases was measured, as shown in Fig. 5.2b. It should be noted that the short-circuit test has to be performed whilst ensuring the resultant currents stay within safe levels.

From the open- and short-circuit tests the per-phase internal impedance of the wind generator, Z_i, can be calculated by

$$Z_i = \frac{E_{oc}}{\sqrt{3} I_{sc}}. \tag{5.2.2}$$

From the Z_i, the internal inductive reactance, X_{Li}, and therefore, the value of the per-phase internal inductance of the wind generator, L_i, can be calculated by

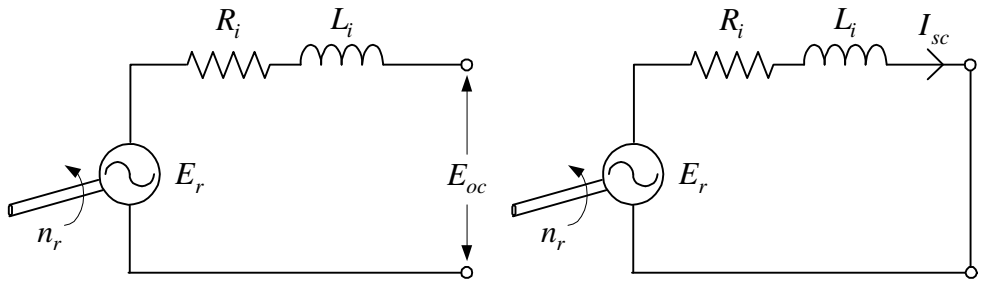

(a) Open-circuit test (b) Short-circuit test

Figure 5.2: Open- and short-circuit tests.

$$X_{Li} = \sqrt{Z_i^2 - R_i^2}$$
$$L_i = \frac{X_{Li}}{2\pi f_r}, \tag{5.2.3}$$

where f_r is the rated frequency of the wind generators. The results of all the tests are tabulated in Table 5.1. This method of determining the generator parameters obtains good results in machines where $R_i << X_{Li}$.

5.2.2 Rectifier-resistor tests

In this section the wind generator was loaded by a resistive load which was connected through a three-phase bridge-rectifier. The test was performed at a rated mechanical speed of 200 rpm. The waveforms of the line current, I_r, and the phase terminal voltage, V_r, all measured at the rated speed, are shown in Fig. 5.3. From this it is shown that the terminal voltage waveform is forced into a stepped square-wave pattern, with the plateau of the waveform sporting the familiar six-pulse dc-ripple curves which are due to the presence of the six-pulse rectifier. The resultant line current waveform has a close to sinusoidal shape which can be attributed to the high internal inductance which are associated with iron-cored machines.

5.2.3 Rectifier-battery tests

In this section the rectifier-resistor load was replaced with a rectifier-battery load. The object of this test was to duplicate, in the laboratory, the typical scenario for any small-scale wind generator which would be installed on a wind site. The wind generator was loaded with a 36 V battery bank which was directly connected on the dc-side of a three-phase bridge rectifier, as shown in Fig. 5.4.

Again, the wind generator battery charging system was tested at a rated rotating speed of 200 rpm. The waveforms of the line current, I_r, and the terminal voltage,

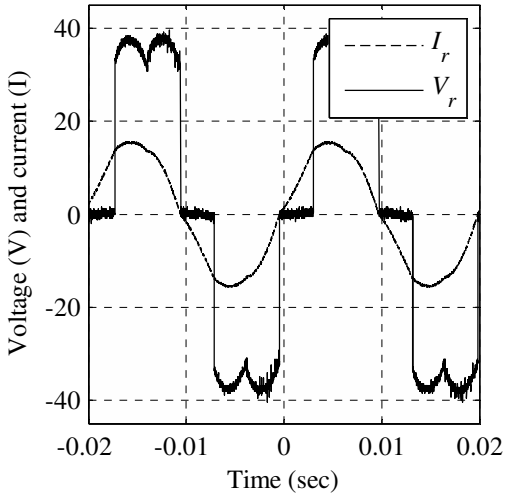

Figure 5.3: Competitor wind generator voltage and current with rectifier-resistor load.

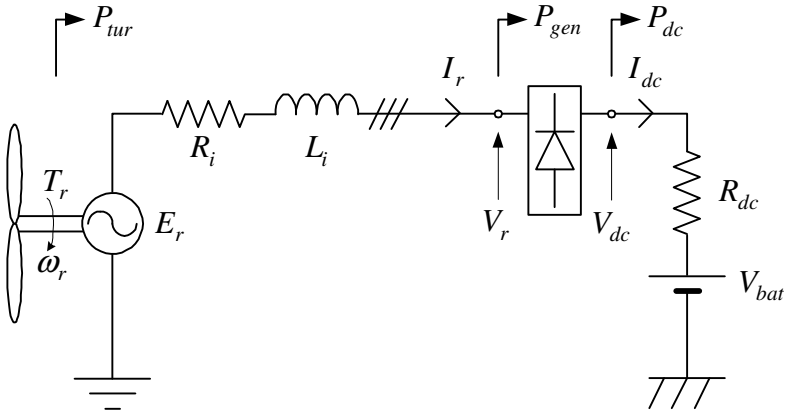

Figure 5.4: Equivalent circuit of the wind generator connected to the rectifier-battery load.

V_r, are shown in Fig. 5.5. From this it is clear that the waveform of the terminal voltage of the wind generator was again square-wave shaped but with a plateau which is due to the presence of the battery bank. Note how the flat-topped terminal voltage rose from the 36 V dc-value of the battery bank, to a dc-value over 40 V, due to the voltage drop across R_{dc}. The line current waveform retained its rather sinusoidal shape.

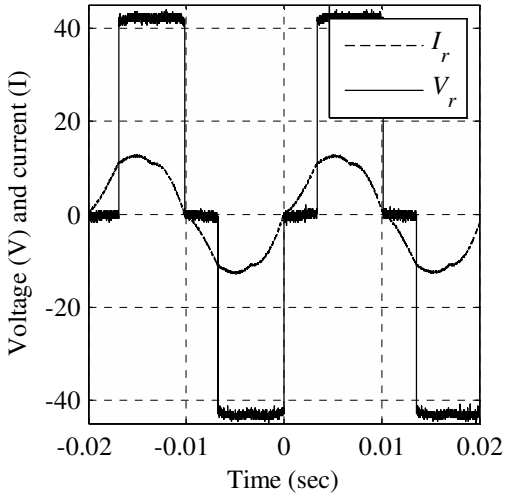

Figure 5.5: Competitor wind generator voltage and current with rectifier-battery load.

5.2.4 Power delivery test

The power delivery test was conducted by measuring the power at various points in the wind generator system, at different rotating speeds. The test was done to determine how well the wind generator system matched the wind turbine to which it would be connected. The results of this test were plotted on the wind turbine power graph as shown in Fig. 1.8.

The input power generated by the wind turbine, P_{tur}, was measured on the shaft connected to the wind generator, the output power of the wind generator, P_{gen} was measured at its terminals, while the power delivered to the battery bank, P_{dc}, was measured at the battery terminals. The difference between P_{tur} and P_{gen} can be understood as the efficiency of the wind generator, while the difference between P_{gen} and P_{dc} is the efficiency of the rest of the wind generator power system. From these measurements a graph of the power delivery capabilities of the wind generator with the rectifier-battery load connected is shown in Fig. 5.6. From this it is clear that the wind generator has good power capturing capabilities at the frequent occurring lower wind speeds. As the wind speed increases, however, the power capturing drifts away from the optimum load line which is indicated by the dotted peaks. The values of the rated power, P_{tr}, and system efficiency, η_{sys}, are tabulated in Table 5.1.

5.2.5 Harmonic Analysis

A harmonic analysis of the current was done at the rated rotating speed of 200 rpm. From equation (5.2.1), the rated frequency of the wind generator can be

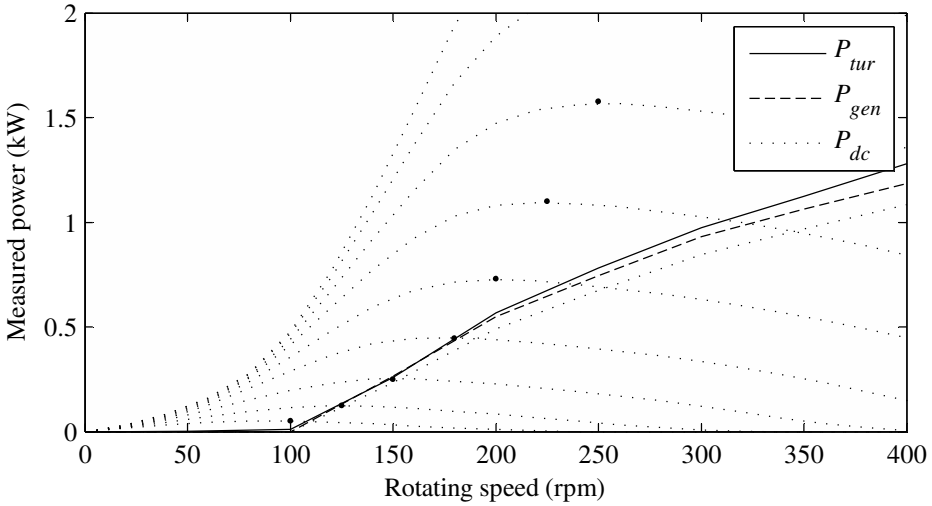

Figure 5.6: Wind generator power point matching.

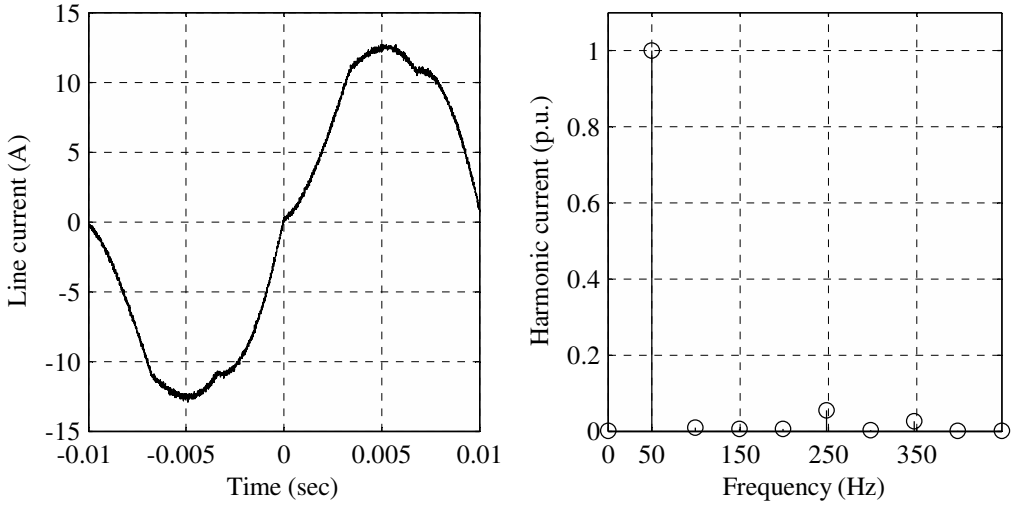

(a) Line current (Time domain) (b) Line current (Frequency domain)

Figure 5.7: Harmonic current analysis of competitor unit at 50 Hz.

calculated as 50 Hz. The line current which was measured is displayed in the time domain in Fig. 5.7a. With the use of a Fast Fourier Transform analysis the line current is also displayed in the frequency domain, as shown in Fig. 5.7b. As shown there is some harmonic content present in the line current at 250 Hz and 350 Hz, which can be calculated, with equation 4.4.1, as the 5^{th}- and 7^{th} harmonics of the 50 Hz fundamental frequency. The 5^{th}- and 7^{th} harmonic components are due to the presence of the six-pulse rectifier in the system.

5.2.6 Conclusions

As is clear from the power matching graph in Fig. 5.6, the competitor wind generator is not utilising the full potential of the wind turbine during higher wind speeds. But, as mentioned earlier, the power delivery is very close to the optimal and can not be altered by simply adjusting the value of L_s. This implies that if a different wind turbine is used or if the wind generator is moved to another location which has different wind characteristics, the profile of the wind power graph, shown in Fig. 1.8, changes substantially. The effect of the change is that the competitor unit will not be able to adjust its power delivery to the different wind power profile. But, under the present conditions, it performs very well.

5.3 Uncompensated system

In this section the uncompensated wind generator, that was designed and developed at the Stellenbosch University's Electrical Machines Laboratory, is discussed and evaluated. The machine is a 24-pole AFPM generator which incorporates a coreless overlapping stator winding. The cross-sectional schematic diagram of the wind generator is shown in Fig. 1.7.

5.3.1 Equivalent circuit

The parameters of the equivalent circuit of the coreless AFPM wind generator are calculated and measured in this section. For comparative purposes the tests are conducted on the uncompensated system at the same rated rotating speed as the competitor unit.

The internal resistance of the wind generator, R_i, was determined by applying a fixed dc-voltage across a phase of the stator winding and measuring the current. This test of the resistance was performed after the machine had been operating and the temperature had reached its steady-state value.

The open-circuit test was conducted to measure the rated back-EMF of the wind generator, E_r, at its rated rotating speed, n_r, and the results are tabulated in Table 5.1.

The short-circuit test could not be conducted to measure the internal inductance, L_i, of the wind generator accurately, as this machine has $R_i >> X_{Li}$. As mentioned in previous chapters, it is extremely difficult to measure the low values of internal inductance of a coreless AFPM machine accurately. As a result the internal inductance of the machine was calculated with the use of a number of different tests. These tests are discussed in more detail in Appendix H. The internal inductance, L_i, as determined from these tests is tabulated in Table 5.1.

5.3.2 Rectifier-battery tests

In this section the behaviour of the wind generator while it is loaded by a battery bank connected through a three-phase bridge rectifier, is discussed. The rectifier-battery load represents the load placed on the wind generator on a small-scale, low power wind site. The rectifier-battery tests were performed at the rotating speed of 200 rpm, which equals a frequency of 40 Hz, as calculated by equation (5.2.1). From Fig. 5.8 it is clear that the phase current is forced into a completely non-sinusoidal waveform. The resultant waveform has two pulses of the six-pulse rectifier for each half cycle, with very little filtering. This is due to the low internal impedance of coreless AFPM machines having very little filtering effect on the line currents.

5.3.3 Power delivery test

In this section the wind generator was loaded by the rectifier-battery load while the rotating speed was increased from standstill. As shown in Fig. 5.9, the wind generator matched the optimum load line very well at the higher wind speeds. Unfortunately, the wind generator was only designed for a maximum power output of 1.5 kW. Therefore, during the seldom occurring higher wind speeds, a threat of over-heating of the stator windings exists. The power and efficiency of the wind generator system under rated conditions are tabulated in Table 5.1. Due to the low average South African wind speeds, the power delivery capabilities are seriously compromised by the non-optimum power matching at lower wind speeds.

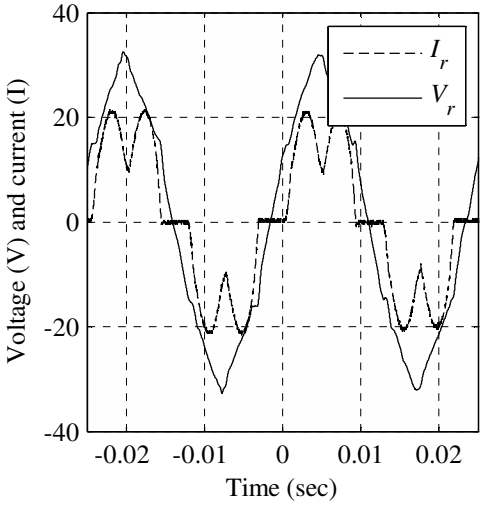

Figure 5.8: Uncompensated wind generator voltage and current with rectifier-battery load.

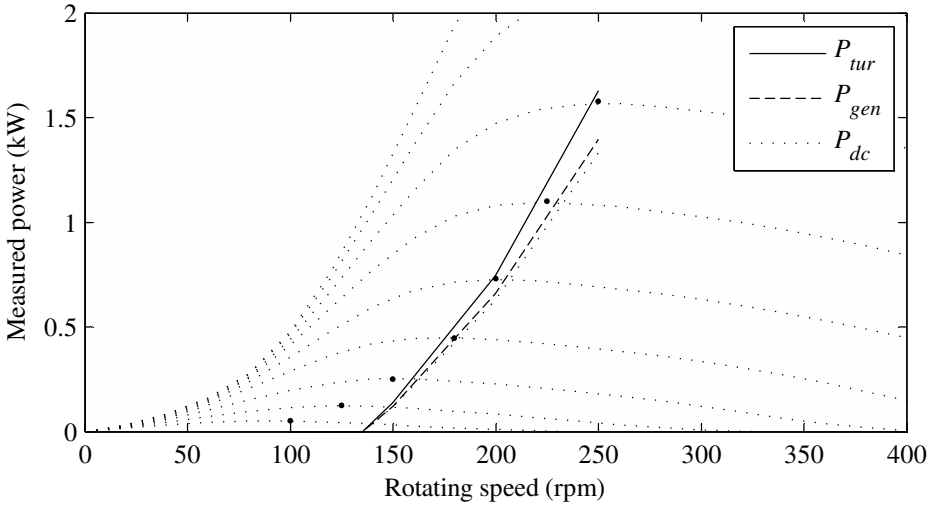

Figure 5.9: Power point matching of the uncompensated system.

5.3.4 Harmonic analysis

A harmonic analysis was performed on the line current in a wind generator system with the rectifier-battery load, at a frequency of 40 Hz. The line current is displayed in Fig. 5.10a in the time domain. As previously mentioned, the shape of the line current waveform is non-sinusoidal and the resultant harmonic content is shown in Fig. 5.10b. As shown, the wind generator system has a very high 5^{th}- and 7^{th} harmonic content. These high values of harmonic components are created by the six-pulse rectifier that is installed in the wind generator system. These current harmonics which are introduced into the system are responsible for the bothersome whining noise emitted from the wind generator under loaded conditions, as discussed in the previous chapters.

5.3.5 Conclusion

The first concern regarding the uncompensated wind generator system is that it does not utilise the frequently occurring, low wind speed power that is generated by the wind turbine. As a result, the wind generator system yields a lower annual power delivery compared to the competitor unit discussed in the previous section. The second concern is the very dangerous over-current situation, which is due to the low inductance of the machine. The linear rise in the generated power will ultimately result in fatal damage of the stator windings. The third concern is the sharp-pitched noise emitted by the wind generators under loaded conditions. This is due to the high harmonic content of the line current that is present in the system. The noise concern, which is commonly associated with this type of machine, is discussed in further detail later in this chapter.

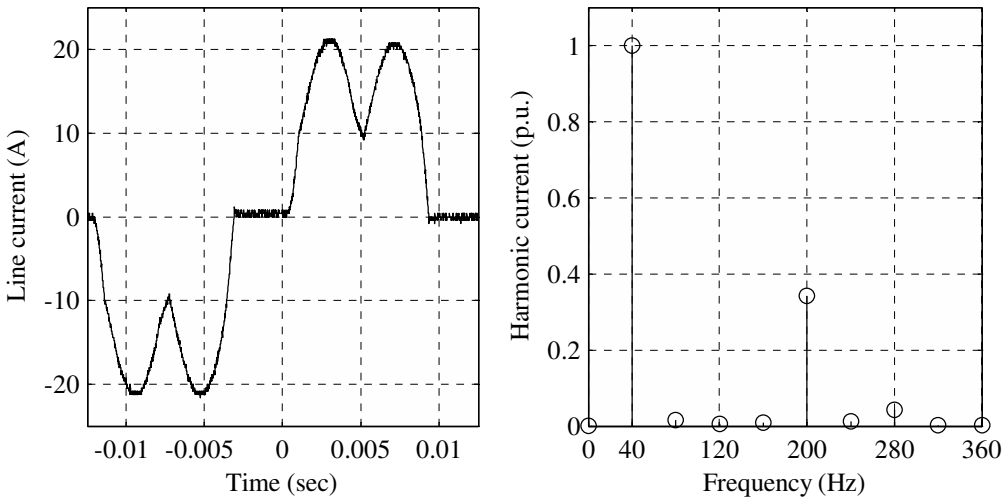

(a) Line current (Time domain) (b) Line current (Frequency domain)

Figure 5.10: Harmonic current analysis of the uncompensated system at 40 Hz.

5.4 Stator winding comparative tests

From the analysis in Chapter 3, it is shown that from a manufacturing point of view it would be sensible to implement the non-overlapping winding configuration for the stator windings. In this section there is a description of how the performance capability of the aforementioned stator topologies was tested. The stators were designed and constructed to be able to be tested on the same 24-pole AFPM machine. Therefore, nothing on the rotor design could be altered [30].

In order to obtain the friction losses, consisting of bearing and windage losses, a no-load test was performed on the AFPM generator at its rated speed. During the no-load operation, the no-load rotational losses, P_{oc}, could be measured and calculated by

$$P_{oc} = P_w + P_{fr} \tag{5.4.1}$$

where P_w and P_{fr} are the mechanical wind- and friction losses respectively. The no-load losses are the same for all the stator windings and can therefore be ignored in the comparative study. The comparative study was performed with the use of a balanced resistive load, while the copper losses in the stator windings were kept constant. The results of these tests are tabulated in Table 5.2.

Also tabulated in Table 5.2 are the calculated and measured results of the mass of copper required in the stator windings for the different winding topologies. The delivered torque, T_d, of the different stator windings were also compared and good agreement is found between the results of the calculations, practical measurements and finite element analysis.

In the next sections the normal overlapping winding and the non-overlapping winding topologies are investigated.

5.4.1 Normal overlapping winding

The coreless normal overlapping stator of the AFPM machine is shown in Fig. 5.11. Note that the circular indent in the surface is the space where the permanent magnets rotate.

Back-EMF

The AFPM generator was driven at an electrical frequency of 40 Hz to record the shape of the back-EMF waveform, as shown in Fig. 5.12a. From this, with the use of FFT analysis, the back-EMF could be calculated in the frequency domain, as shown in Fig. 5.12b. Here it is shown that there is some 3^{rd}- and 5^{th} harmonic content present in the back-EMF waveform of the normal overlapping winding.

5.4.2 Non-overlapping winding

The coreless non-overlapping stator winding is shown in Fig. 5.13. Note the completely flat surface of the stator, unlike in the overlapping winding stator, i.e. no indentation is required for the rotating permanent magnets.

Back-EMF

In the comparative study, the AFPM generator was again driven at an electrical frequency of 40 Hz to record the shape of the back-EMF waveform, as shown in

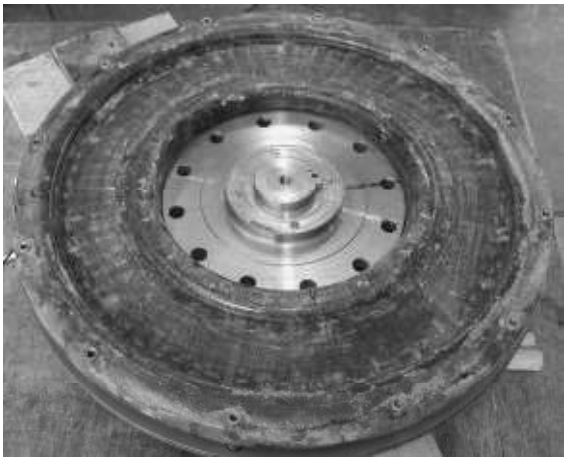

Figure 5.11: Normal overlapping winding.

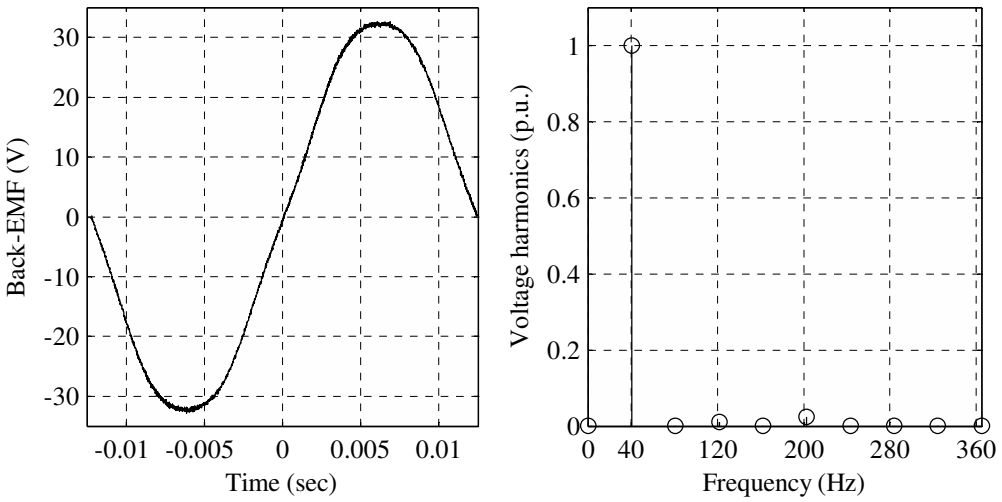

(a) Back-EMF (Time domain) (b) Back-EMF (Frequency domain)

Figure 5.12: Harmonic analysis of the back-EMF at 40 Hz.

Figure 5.13: Non-overlapping winding.

Fig. 5.14a. The harmonic content of the back-EMF waveform was calculated in the frequency domain as shown in Fig. 5.14b. From this it is clear that the non-overlapping winding has a reduction in the harmonic content of the back-EMF waveform, compared to the normal overlapping winding. Only a trace amount of the 3^{rd} harmonic is present in the back-EMF waveform.

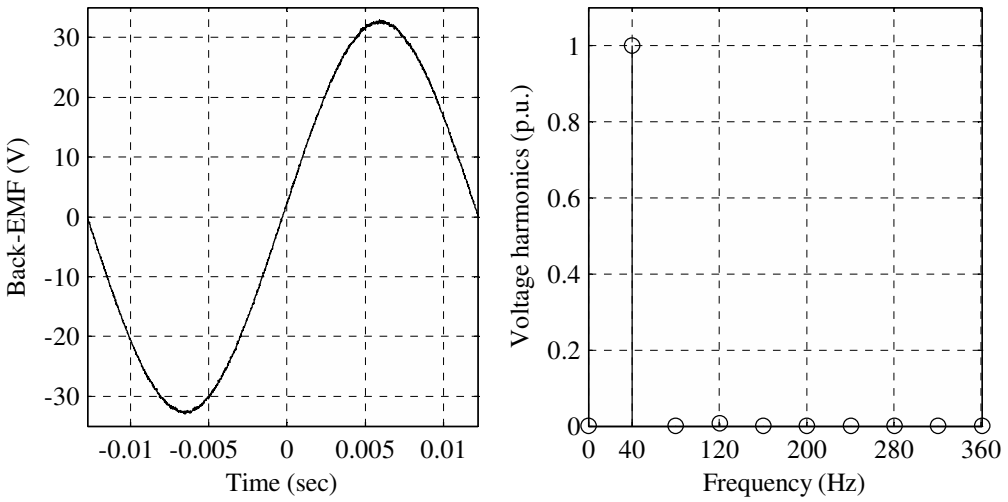

(a) Back-EMF (Time domain) (b) Back-EMF (Frequency domain)

Figure 5.14: Harmonic analysis of the back-EMF at 40 Hz.

5.4.3 Phase-grouped winding

Another variation of the non-overlapping winding topology is the phase-grouped winding topology. As the name suggests, the coils which form the phase of the stator winding are grouped together. For comparative purposes the results of the tests are included in Table 5.2. This winding topology is discussed in more detail in Appendix B.

5.4.4 Conclusion

In Table 5.2 it is shown that non-overlapping winding topology can achieve similar efficiency compared to the normal overlapping winding topology, in terms of developed torque and power. The non-overlapping winding even shows an improved sinusoidal voltage waveform, as there are less harmonic content present in the back-EMF. Another advantage that the non-overlapping winding has over the overlapping winding is that it requires much less copper in its construction.

5.5 Improved system

In this section the design of the improved system is discussed. The improved system consists of an AFPM wind generator, similar to that of the uncompensated system, as well as a series-connected external inductor, as has been suggested in the previous chapter. It is explained in the previous section that a machine equipped with a non-overlapping winding can achieve similar efficiency compared to the normal

Table 5.2: Design data

Design data	Over-lapping	Non-over-lapping	Phase-grouped
Output power P_{out}, kW		1	
Speed n, rpm		200	
Number of phases		3 (Star)	
Rated line voltage, V	19.88	19.56	18.43
Rated phase current, A	13.79	14.23	13.06
Output power, W	810.3	817.67	711.62
Efficiency, %	87.8	87.4	85.5
Frequency f, Hz		40	
Number of pole pairs p		12	
Number of stator coils (3 phases)	36	18	21
Air gap magnetic flux density B_{mg} under load, T		0.527	
PM outer diameter D_{out}, mm		400	
$k_d = D_{in}/D_{out}$ ratio		0.6	
Class of insulation		F	
Winding temperature rise, ^{o}C	9.9	12.1	8.3
Cooling system		Self air-cooled	
Number of coils in phase group n	-	1	7
T_d, Calculated, Nm	45.87	45.31	40.59
T_d, FEA, Nm	44.36	45.13	39.54
T_d, Measured, Nm	43.9	44.6	39.7
M_{Cu}, Calculated, kg	3.245	2.891	2.217
M_{Cu}, Measured, kg	3.484	2.977	2.175

overlapping winding equipped machine, while being simpler and less expensive to manufacture. Therefore, it would be sensible to incorporate the non-overlapping winding topology into the improved system.

In order to extract most of the power available from the low wind speeds, the stator winding had to be redesigned in order to develop the ac-equivalent of the battery voltage at a lower rotating speed. To achieve the required optimal power matching, as well as the required reduction in current harmonics, an external

inductance was connected in series in the wind generator system, as shown in Fig. 4.8. The effects of the external inductance on the wind generator system were investigated with the use of an electronic simulation package, Simplorer^{TM}.

5.5.1 Effect of system inductance on power matching

In this section it will be shown how a variation in the value of the system inductance in the wind generator system has an impact on its power matching capabilities.

The three-phase equivalent circuit of the wind generator system was simulated in Simplorer^{TM}, as shown in Fig. 5.15.

The non-overlapping stator winding of the AFPM wind generator was designed so that it would start delivering power to the battery bank at a rotating speed of 75 rpm. To achieve the variable power matching capabilities, the system inductance was varied by increasing the value of the series-connected external inductance on the ac-side of the bridge-rectifier. By changing the value of the external inductor, the load that is connected to the wind turbine is varied resulting in a change in the generated turbine power, as shown in Fig. 5.16. From here the effect of the various values of L_e can be seen. From this can be decided what value of external inductance is required in order to achieve the power matching that is desired.

Calculating the parameters

In this section the value of L_e that is required to achieve the desired power matching was analytically calculated. It was decided that the wind generator should have the lowest possible cut-in speed. It was also decided that the rated conditions of the wind generator system should be reached at a wind speed of 8 m/s. Referring to Fig. 4.5, the two operating points, b and r, could be selected and were tabulated in Table 5.3. With the use of equations (4.1.1) - (4.2.10), it was calculated that an external inductance with a value of 6.9 mH was required to achieve the desired power matching.

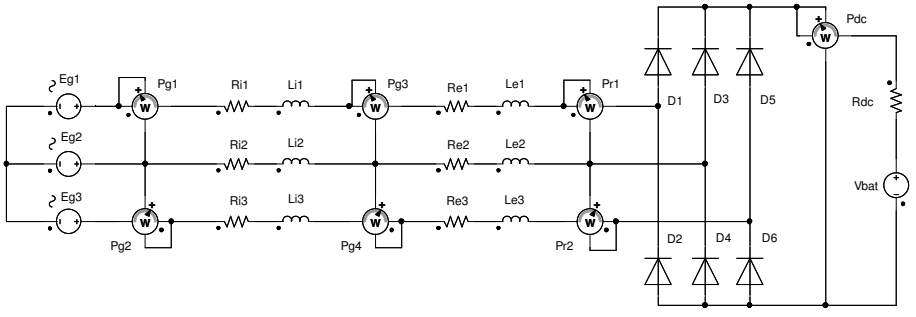

Figure 5.15: Equivalent circuit model of the wind generator system in Simplorer^{TM}.

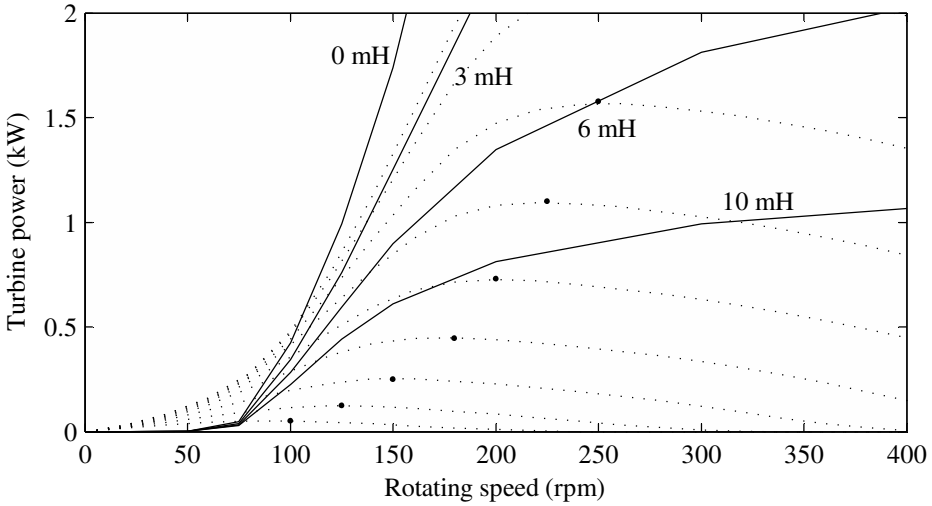

Figure 5.16: Power point matching with varying L_e values.

Table 5.3: Power matching

Parameters	Values
Cut-in speed n_b, rpm	74.4
Cut-in voltage V_b, V	16.9
Cut-in frequency f_b, Hz	19.8
Rated speed n_r, rpm	220
Rated turbine power P_{tr}, kW	1.3
External inductance L_e, mH	6.89

5.5.2 Effect of system inductance on current harmonics

In this section it is shown how a variation in the system inductance of the wind generator system has an impact on the current harmonics of the system.

The simulation which was described in the previous section was repeated with the attention focussed on the line current harmonics, as shown in Fig. 5.17a. From this, with the use of a FFT analysis, the harmonic content present in the line current waveforms was calculated. As discussed in previous sections, the rectifier-battery load induces 5^{th}- and 7^{th} current harmonics in the system. It is shown in Fig. 5.17b that with an increase in the value of L_e there is a corresponding decrease in harmonic content of the line current. From this can be decided what value of external inductance is required to sufficiently reduce the harmonic content in the wind generator system.

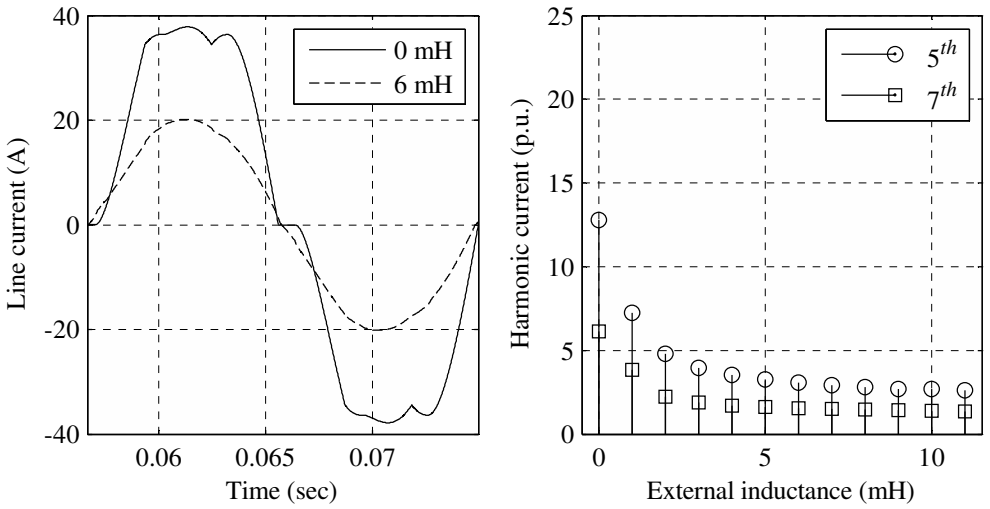

(a) Effect of L_e on line current waveform. (b) Current harmonic component versus L_e values.

Figure 5.17: Current harmonic with varying L_e values.

Table 5.4: Harmonic suppression

Parameters	Calc
Cut-in speed n_b, rpm	75
Cut-in voltage V_b, V	16.9
Line current I_r, A	13.7
External inductance L_e, mH	3.5

Calculating the parameters

In this section the required value of external inductance is analytically calculated in order to achieve the desired reduction in harmonic current of the wind generator system. The cut-in speed was again chosen as 75 rpm. With the use of equations (4.2.1), (4.4.8) - (4.4.10), L_e was calculated and tabulated in Table 5.4. The value of L_e required for adequate harmonic suppression was calculated as 3.5 mH, which agrees well with Fig. 5.17b.

There is some approximation in the calculation as the analysis is done on the fundamental value of the harmonic components only. This is indicated by the graph showing the practically measured parameters in Fig. 5.18a compared to the analysed parameters shown in Fig. 5.18b.

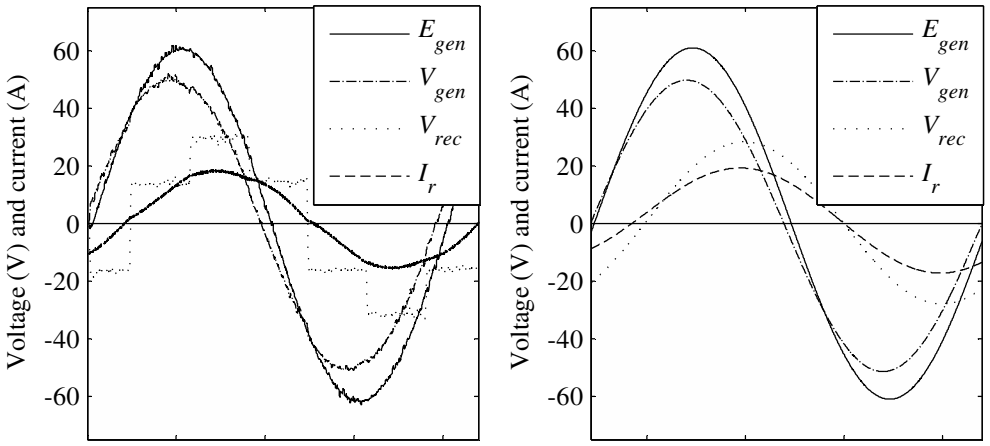

(a) Measured voltage and current waveforms.

(b) Analysed voltage and current waveforms.

Figure 5.18: Practical measurements versus the fundamental analysis of the voltage and current waveforms of the wind generator system.

5.5.3 Rectifier-battery tests

In this section the improved wind generator system, as designed for power matching in Table 5.3, is evaluated. The external inductance, using both methods of calculating the required value, was calculated as 6.9 mH and 3.5 mH. It is therefore sufficient to evaluate the higher value as that would satisfy both criteria.

The non-overlapping winding equipped AFPM wind generator was designed to have a cut-in speed of 75 rpm. The required power matching was practically achieved with an external inductor with the value of 7.5 mH. This was the closest value available in the laboratory, which had the required current-carrying capability. The improved system, including the external inductance, was connected to a rectifier-battery load. The rectifier-battery test was performed to evaluate the wind generator as it would be operating on a small-scale, low power wind site.

In Fig. 5.19 it is shown that the wind generator has close-to-sinusoidal line current and terminal voltage waveforms under rated conditions. The voltage and current waveforms of the wind generator system has been much improved upon when compared with the uncompensated system.

5.5.4 Power delivery test

In this section the power delivery of the improved wind generator system is evaluated. From Fig. 5.20 it is clear that the power developed by the wind turbine, P_{tur}, is greatly improved in the low to medium wind speed areas, compared to the uncompensated system. In the medium to high wind speed areas the power

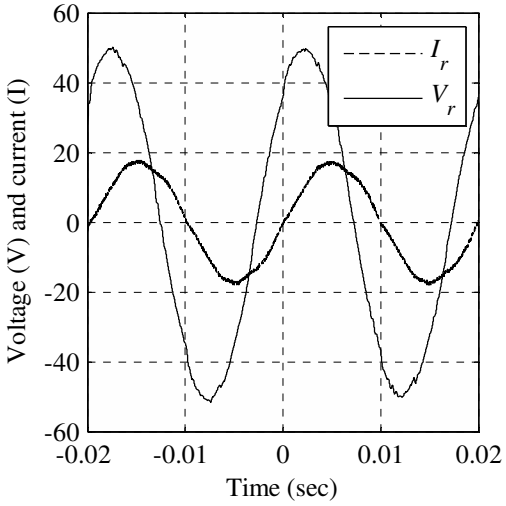

Figure 5.19: Wind generator loaded with rectifier-battery load.

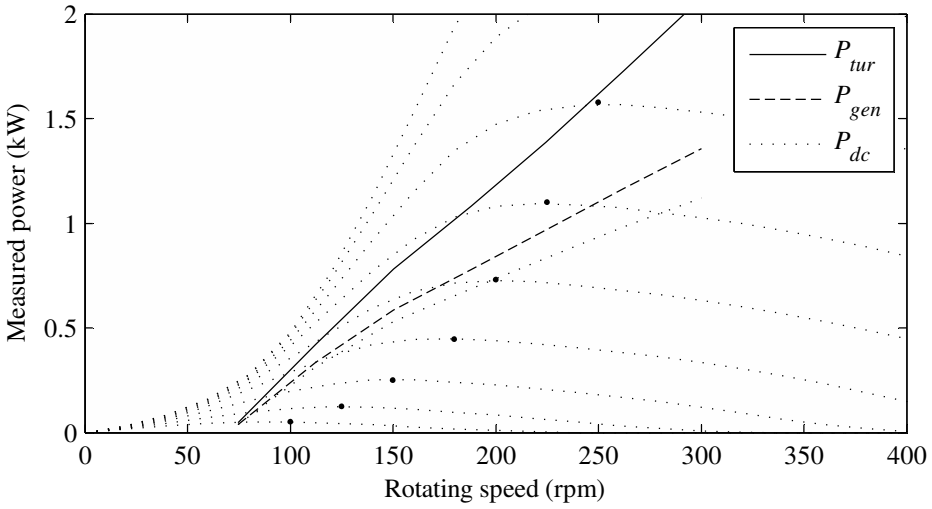

Figure 5.20: Wind generator power point matching with $L_e = 7.5$ mH.

point matching is not optimal before it crosses the optimal load line at operating point b. At operating point b, the turbine power of the improved system matches the turbine power of the uncompensated system, as shown in Table 5.1. Unlike in the uncompensated system, the power delivered to the battery load, P_{dc}, does not increase as steeply as the rotating speed increases. Thus, the wind generator will be able to sustain high wind speeds electrically, without the fear of burning the stator windings as the copper losses do not increase much.

5.5.5 Harmonic analysis

A harmonic analysis was conducted on the line current of the wind generator at the rated frequency of 50 Hz. The line current is shown in Fig. 5.21a in the time domain. The line current of the improved system has a much more sinusoidal waveform than that of the uncompensated system. This is confirmed with the line current in the frequency domain, as shown in Fig. 5.21b. From this it is clear that there is a substantial decrease in the 5^{th}- and 7^{th} harmonic content of the current. This would certainly have a major positive impact on the noise emitted from the AFPM wind generator.

5.5.6 Conclusion

The improved wind generator system has a close-to-sinusoidal line current waveform, which results in a reduction of the emitted noise of the coreless AFPM wind generator. It is also shown that the wind generator can have a much better maximum power point matching at the all-important low to medium wind speed areas, which yields a higher annual power capturing capability, compared to the uncompensated system shown in Fig. 5.9.

From Table 5.1 and the power delivery graph shown in Fig. 5.20, it is clear that the modifications made to the wind generator make the wind generator system very inefficient at its rated rotating speed. It should be noted that although the wind generator system is not operating efficiently, the overall power delivered at

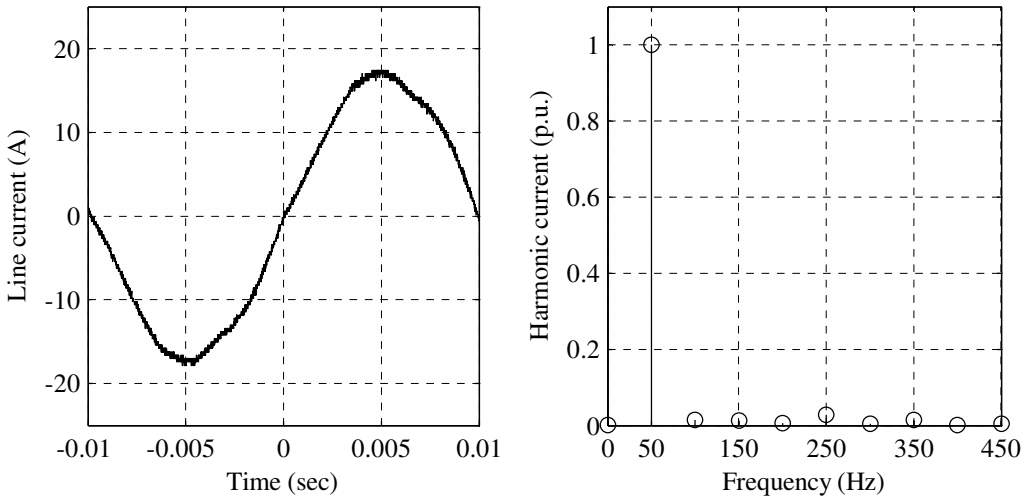

(a) Line current (Time domain) (b) Line current (Frequency domain)

Figure 5.21: Harmonic current analysis of the improved system at 40 Hz with L_e = 7.5 mH.

the battery bank is higher than that of the competitor unit, shown in Fig. 5.6.

5.6 Acoustic noise measurement

In this section the acoustic noise measurement analysis that is conducted on the wind generators is discussed. It can be assumed that at the low rotating speeds of the wind generators, the aerodynamic noise is negligible.

The acoustic tests were performed according to the standards specified in the ISO 1680 for rotating electrical machines. Therein it states that the machines should be tested under steady-state conditions [48]. Furthermore, according to the specification for acoustic measurement (IEC 61400-14), it is required that acoustic measurements be performed on the wind generator at a height of 1 m, with a wind speed of 8 m/s. The latter was not possible in the laboratory. Therefore, it was decided that, for comparative purposes, the wind generators would be tested at rated rotating speed, with the use of a VSD-controlled electrical motor on the practical test setup.

5.6.1 Acoustic measurement of the competitor unit

Firstly, the 30-pole competitor unit was driven, under no-load, at its rated speed of 200 rpm and the acoustic measurements were taken. This was performed so that the aerodynamic noise, ambient noise floor, prime mover noise and VSD switching noise could be established. After the no-load test, the competitor unit was loaded with the rectifier-battery load and driven at its rated frequency of 50 Hz, and the required measurements were taken. The results of the two above-mentioned tests, no-load and load, were displayed in the audible spectrum of between 20 Hz and 20 kHz using a logarithmic scale, as shown in Fig. 5.22. Note, the peaks at 2,5 kHz and multiples thereof. These peaks are due to the 2,5 kHz switching frequency of the VSD that was used.

As the results shown in Fig. 5.22 are not very clear, the no-load test measurement was subtracted from the load test measurement. This result is the actual impact of the loaded conditions on the noise measurements. The result of the actual loaded conditions is displayed in a zoomed-in frequency range where only the frequency range of most concern is displayed, as shown in Fig. 5.23. The 6^{th}-, 12^{th}- and 18^{th} harmonic components are indicated by small arrows. From this it is shown that there is some 15 dBV difference between the loaded and no-load measurements at the 6^{th} harmonic of the fundamental frequency of 50 Hz. It should also be noted that there are some 12^{th}- and 18^{th} harmonics present in the noise measurement. These harmonics, which are multiples of six, are induced by the six-pulse rectifier that is used as load in the tests.

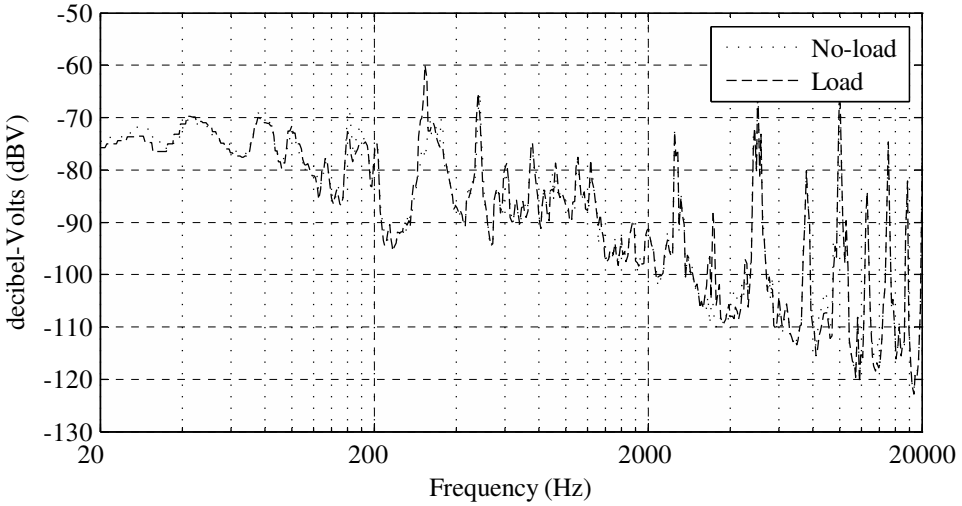

Figure 5.22: Acoustic measurement of the competitor unit in the audible spectrum.

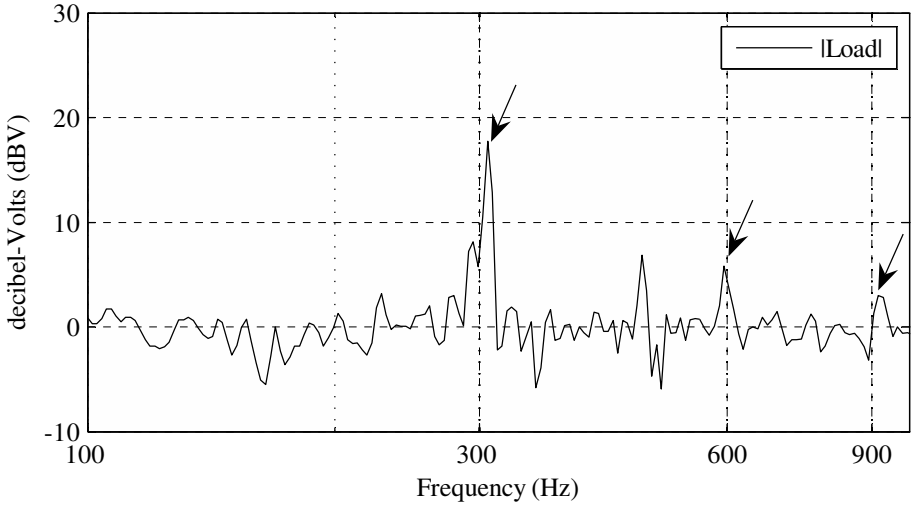

Figure 5.23: Zoomed-in absolute acoustic measurement of the competitor unit.

5.6.2 Acoustic measurement of the uncompensated system

The competitor unit was replaced by the uncompensated AFPM wind generator system. This was done in order to establish the possibility that with the addition of an external inductance, the acoustic noise emitted by the wind generator could be reduced.

The acoustic measurements were again performed under the rated conditions of the wind generator. As this is a 24-pole generator the comparative rotating speed of 200 rpm equals to a frequency of 40 Hz. As above, the no-load test

was performed so that the unwanted data could be subtracted and the zoomed-in frequency range could be focused upon. Then the uncompensated system was tested under rated load conditions, and the results of the recording are shown in Fig. 5.24a. It is clear that there are harmonic peaks at 240, 480 and 720 Hz, as shown by the arrows. These peaks can therefore be calculated as the 6^{th}-, 12^{th}- and 18^{th} harmonic components respectively, as the wind generator is connected to the six-pulse rectifier.

To investigate the impact of the external inductance on the noise emitted by the uncompensated system, the test was repeated with an external inductance of 3 mH connected, as shown in Fig.5.24b. It is clear that the same harmonic peaks still exist, as indicted by the arrows, but at much reduced magnitudes. A reduction of 20 dBV was measured at the 6^{th} harmonic after the addition of the external inductance. A reduction of only 12 dBV was measured at the 12^{th} harmonic and a reduction 35 dBV at the 18^{th} harmonic. This non-linear relationship in the damping could be as a result of the inherent natural frequency of the AFPM machine.

5.6.3 Conclusion

In this section it has been shown that even with a relatively low value of external inductance, such as 3 mH, a substantial reduction in the noise emitted can be obtained in the AFPM wind generator system.

5.7 Vibration tests

In this section the results of the vibration tests which were performed on the wind generators are discussed. The vibration tests were conducted on the wind generator on the practical test setup. It was assumed that for all practical purposes the platform of the test station was stable enough. The vibrations of the different wind generator parts were measured with the use of a surface mounted vibration sensor. The sensor was fixed to a vibrating surface of the wind generator part, while the amplitude and frequency of the vibrating surface was measured. The vibration sensing unit consists of a sensing element which is constructed of piezo film. The piezo film generates a potential difference which is proportional to the strain imposed on the film [53]. The piezo film unit has a very low voltage output signal which needs to be amplified.

In the following section the process of determining the wind generator part that is responsible for the noise emission, is discussed.

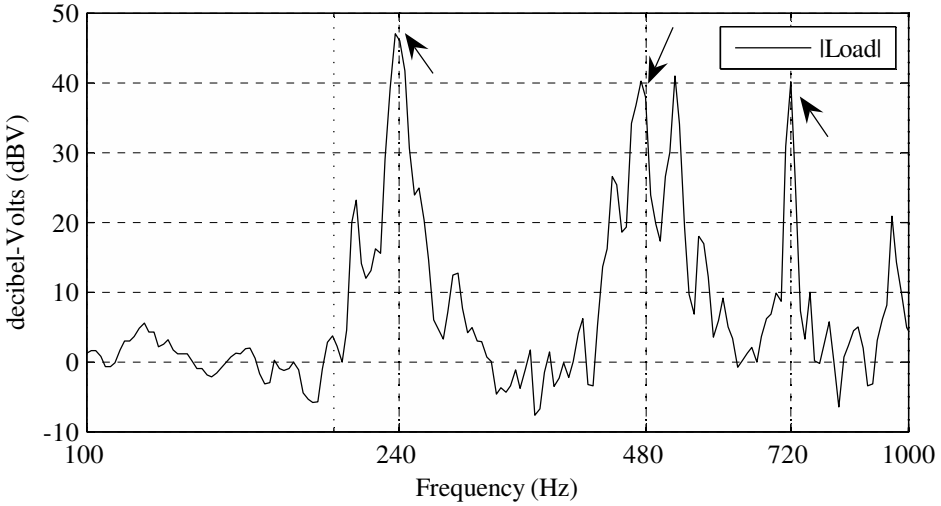

(a) Without external inductance

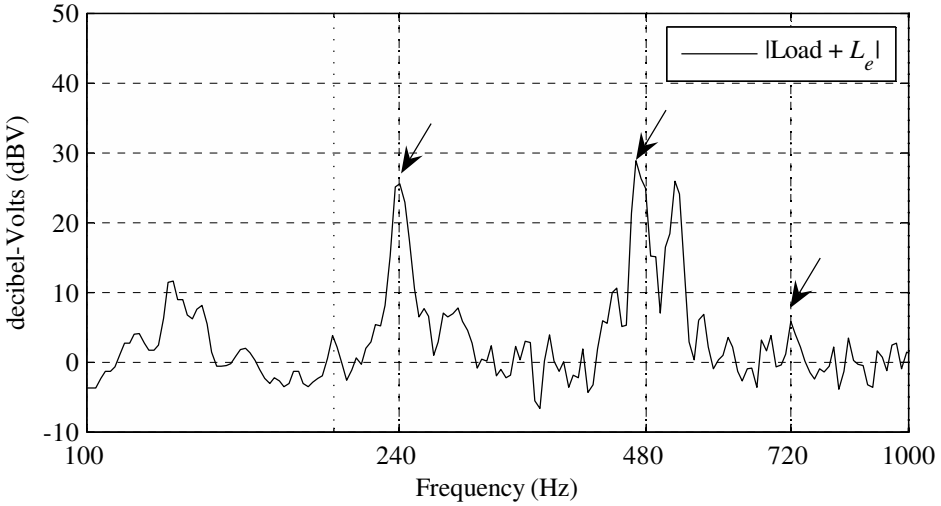

(b) With external inductance

Figure 5.24: Zoomed-in absolute acoustic measurement of AFPM wind generator system.

5.7.1 Impulse test

The piezo film vibration sensor was attached to various parts of the wind generator, while an impulse force was applied to that part. With the use of this method the damped natural frequency of the various wind generator parts could be measured. From the acoustic measurements of the AFPM wind generator shown in the previous section it is clear that there is a non-linear relationship noise reduction in the frequency range of 400 Hz to 500 Hz.

Rotor

The measurement strip was connected to one of the rotor disks and an impulse was applied with the use of a hammer blow. The amplified output vibration voltage of the piezo sensor was recorded. The force created an attenuated vibration which occurred at the inherent damped natural frequency of the part, as shown in Fig. 5.25a [52]. With the use of a Fast Fourier Analysis (FFT) the frequency components of the vibration could be calculated, as shown in Fig. 5.25b. From this it is clear that the damped natural frequency of the rotor disks could be calculated as around 40 Hz. It can therefore be assumed that the rotor disks are not responsible for the noise emission of the wind generator.

Stator

Next, the vibration sensor was connected to the stator of the wind generator and an impulse force was applied to the stator. The measured output of the vibration sensor and frequency components of the waveform are shown in Fig.'s 5.26a and 5.26b, respectively. From this it is clear that the damped natural frequency of the stator can be calculated as around 200 and 400 Hz. These two frequency values are created by the two different parts of the stator; the stator consists of the epoxy encapsulated stator winding as well as the steel backplate onto which the stator winding is mounted. Thus, it is clear that the stator has a much higher natural frequency than the rotor and is responsible for the acoustic noise emission.

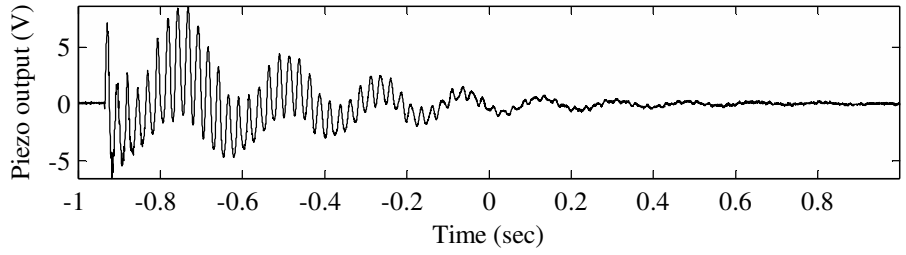

(a) Natural frequency (Time domain)

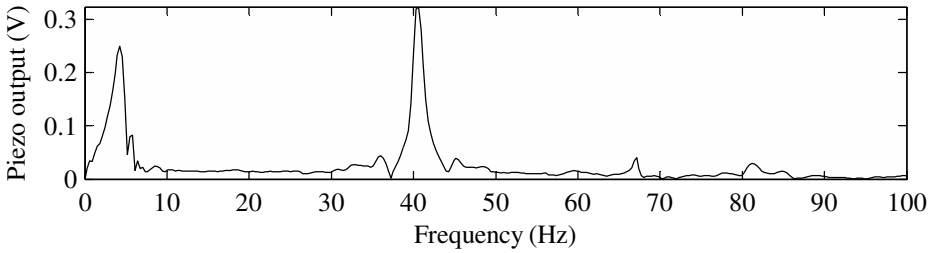

(b) Natural frequency (Frequency domain)

Figure 5.25: Determining the natural frequency of the rotor of the AFPM machine.

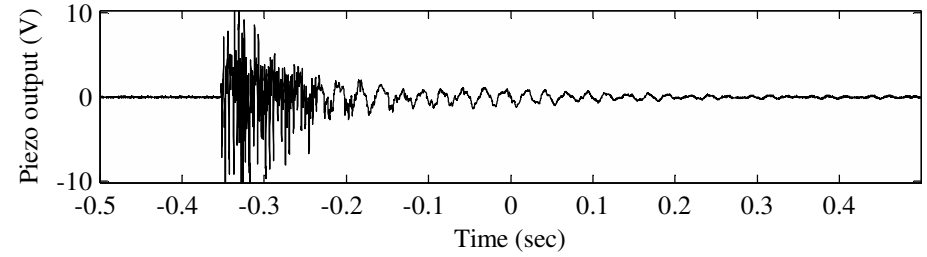

(a) Natural frequency (Time domain)

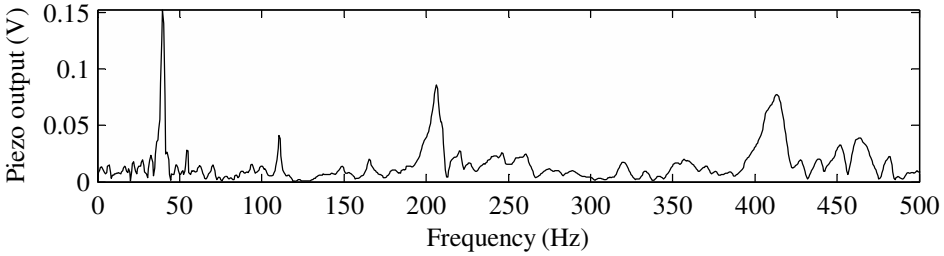

(b) Natural frequency (Frequency domain)

Figure 5.26: Determining the natural frequency of the stator of the AFPM machine.

5.7.2 Rotating tests

In the following tests the piezo film vibration sensor was fixed to the stator of the AFPM generator, which had been shown to be the source of the emitted noise. The tests was performed with the wind generator loaded by a balanced resistive load, a rectifier-battery load and a rectifier-battery load with an external inductance.

Resistive load

In the finite element analysis in Chapter 3, the effect of the mutual torque ripple on all three-phase electrical machines is explained. The wind generator was tested with a balanced resistive load to measure the vibrations caused by the torque ripple.

The test was performed at an electrical frequency of 40 Hz. The piezo film sensor output voltage is shown in Fig. 5.27a. The dc-drift is ignored. The frequency components can be calculated as shown in Fig. 5.27b. From here the frequency peak at the 240 Hz indicates a 6^{th} harmonic component. Thus proving that a 6^{th} harmonic component exists in a circuit with purely sinusoidal currents are drawn, due to the influence of the torque ripple.

Rectifier-battery load

The balanced three-phase resistive load was replaced by a load consisting of a rectifier-battery combination. The wind generator was again rotated at an electrical

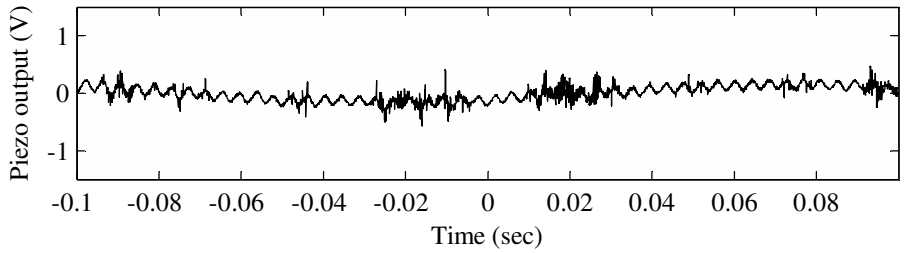

(a) Output voltage (Time domain)

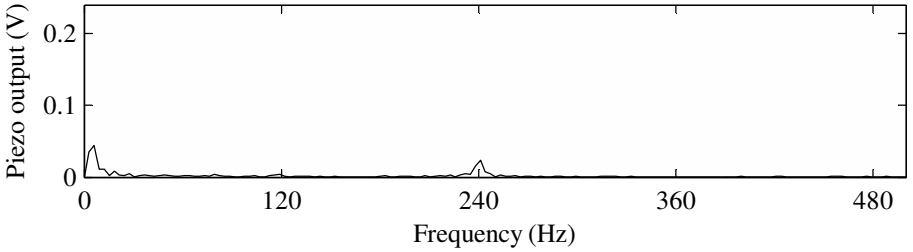

(b) Output voltage (Frequency domain)

Figure 5.27: Vibration measurement of the AFPM generator with resistive load.

frequency of 40 Hz. As indicated by the frequency domain of the measured vibration in Fig. 5.28b, a very large 6^{th} harmonic component and notable 12^{th} harmonic component are present in the system.

Rectifier-battery load with L_e

Next, an external inductance, L_e, was connected in the system. As can be seen in Fig. 5.29b there is a substantial decrease in the measured vibration of the stator. Therefore it can be concluded that with the addition of external inductance a decrease in the stator vibrations is possible.

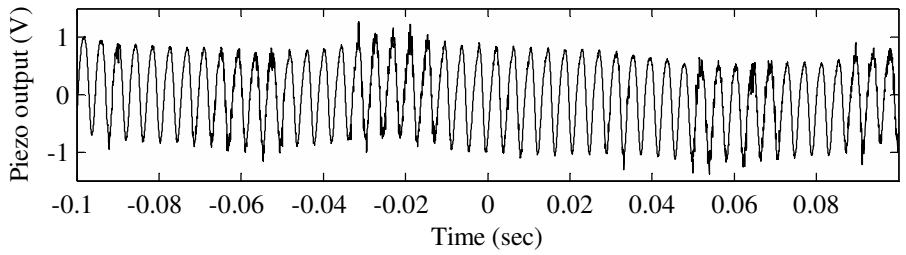

(a) Output voltage (Time domain)

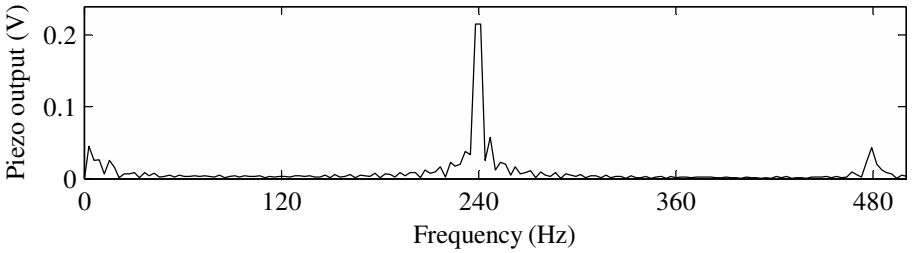

(b) Output voltage (Frequency domain)

Figure 5.28: Vibration measurement of AFPM generator with rectifier-battery load.

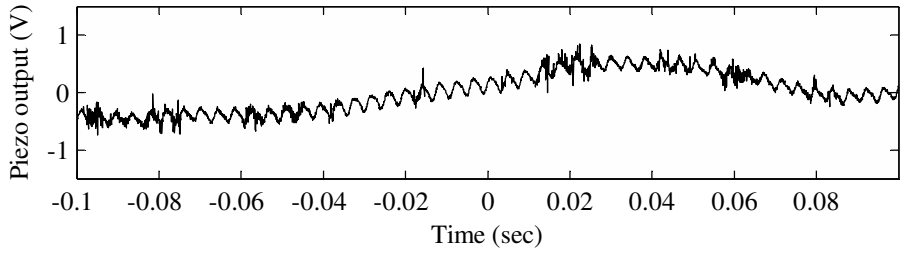

(a) Output voltage (Time domain)

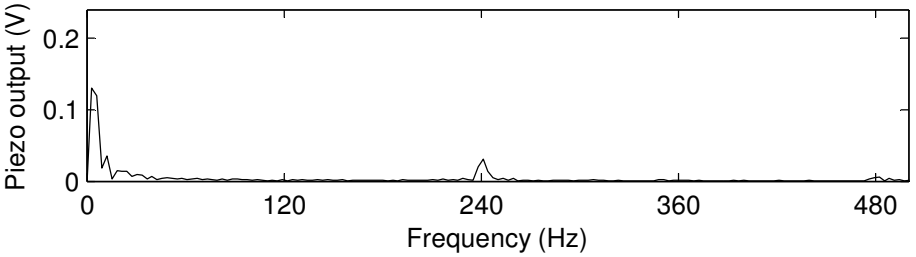

(b) Output voltage (Frequency domain)

Figure 5.29: Vibration measurement of AFPM generator with rectifier-battery load and external inductance.

Chapter 6

Conclusions and recommendations

In this thesis the coreless AFPM generator was evaluated for use in small-scale wind generator applications. These small-scale wind generator systems frequently use direct battery connection, where the battery bank is used for storage of the generated power. The primary concerns that are normally associated with rectifier-fed directly connected battery wind generator systems, such as maximum power point matching and acoustic noise, were discussed.

The coreless AFPM machines was theoretically analysed and different stator winding topologies were evaluated. It was found that AFPM machines equipped with non-overlapping stator windings proved to be as efficient, with similar performance, as machines equipped with the normal overlapping windings. It was also found that the non-overlapping winding equipped AFPM machine uses much less copper. The non-overlapping winding equipped machine also shows an improved sinusoidal back-EMF waveform compared to the normal overlapping machine. These findings were confirmed with finite element analysis and practical measurements.

The wind power system was theoretically analysed with the use of an equivalent circuit analysis. It was shown that AFPM generators are not suitable for direct connection on rectifier-battery loads. This is due to the non-optimal power point matching and harmonic line currents causing severe acoustic noise. It was suggested that the stator winding be redesigned to achieve the battery-clamping voltage at a lower rotating speed, achieving maximum power point matching at the lower rotating speed. The addition of a series-connected three-phase external inductance was suggested to achieve maximum power matching at the higher rotating speed and the required reduction in harmonic line current. An equation was derived which would calculate the value of external inductance to achieve maximum power point matching. Another equation was derived which would calculate the external inductance value required to minimise the harmonic content of the current responsible for the acoustic noise. These calculations were confirmed with the use of Simplorer^{TM} and practical measurements conducted in the laboratory. With correctly selected values of external inductance it was proven that near-optimal power

point matching is achieved with a reduction in acoustic noise.

It was found that the AFPM wind generator system incorporating the external inductance, is not operating at its highest efficiency. The low efficiency is due to the extra turns on the coils of the stator winding to achieve the lower cut-in speed, creating an increase in the stator resistance and resulting in high copper losses in the stator winding. It is recommended that the AFPM wind generator be redesigned to have a slightly higher cut-in speed, which will result in a lower value of external inductance required to achieve the desired power matching, as shown in Fig. 6.1. This will increase the power output of the wind generator system and increase the system efficiency.

It is recommended that to offset the increased copper losses of the AFPM generator, the machine should be slightly over-sized in its design. By increasing the outer diameter the active length of the machine increases, reducing the ratio of end-winding length to active length. An increased active length of the machine increases the generated voltage of the machine, thus lowering the number of turns on each coil of the stator winding, effectively decreasing the phase resistance of the stator winding and decreasing the copper losses.

Another method of minimising the excessive stator resistance is to increase the flux density in the airgap of the AFPM generator. That could be achieved by fitting thicker and/or stronger permanent magnets to the rotor disks. An increase in flux density in the airgap of the generator will also create a higher generated voltage at the same rotating speed, once again resulting in a lower number of turns per coil in the stator winding.

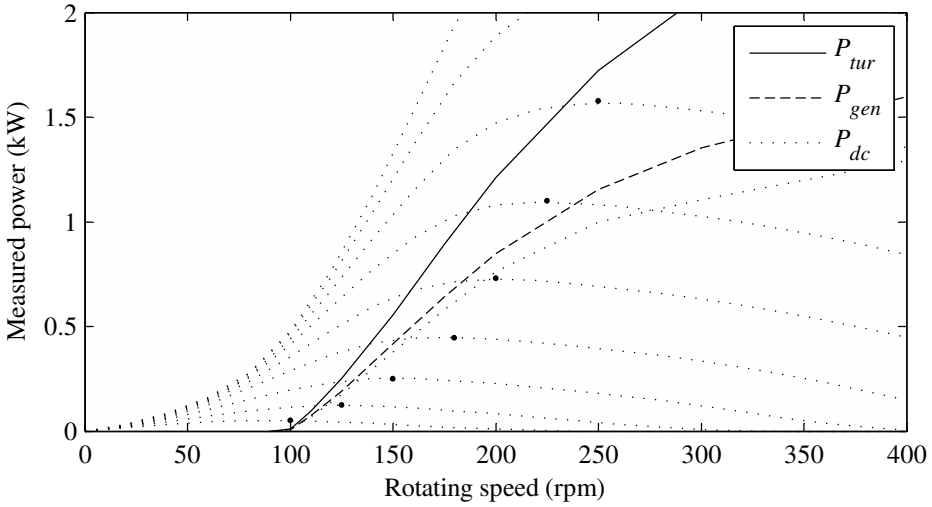

Figure 6.1: Wind generator power point matching.

In classical machine design methodology the wind generator is optimised for the highest efficiency at its rated speed and rated load. An alternative methodology would be to optimise the wind generator for maximum annual energy capture, where highest average efficiency over a wide operating speed range is preferred. This is necessary as the wind generator system seldom operates at its rated operating point [31].

Appendices

Appendix A

Harmonic mitigating transformers

For the purpose of explanation assume the phase current in the wind generator system of squarewave shape. The current is regarded as positive sequence in phase A. Phase A is also taken as the reference with a phase angle of $0°$. The fundamentals of the primaries of the two transformers, TX1 and TX2 shown in Fig. 2.4, are in phase and have the same phase rotation. The fundamentals of the phase currents in the generator bus can be expressed as

$$I_{A(1)} = \frac{2\sqrt{3}}{\pi}\cos\omega t = \frac{2\sqrt{3}}{\pi}\angle 0° \tag{A.0.1}$$

and

$$I_{B(1)} = \frac{2\sqrt{3}}{\pi}\cos(\omega t - 120°) = \frac{2\sqrt{3}}{\pi}\angle -120° \tag{A.0.2}$$

and

$$I_{C(1)} = \frac{2\sqrt{3}}{\pi}\cos(\omega t - 240°) = \frac{2\sqrt{3}}{\pi}\angle -240° \tag{A.0.3}$$

where $I_{A(1)}$, $I_{B(1)}$ and $I_{C(1)}$ are the fundamental currents of the A-, B- and C-phases, respectively.

The 5^{th} harmonic of the current in the A-phase is $180°$ out of phase with the fundamental and is therefore negative sequence. The 5^{th} harmonic of the phase currents in the generator bus can be expressed as

$$I_{A(5)} = \frac{2\sqrt{3}}{5\pi}\cos(5\omega t + 180°) = \frac{2\sqrt{3}}{5\pi}\angle 180° \tag{A.0.4}$$

and

$$I_{B(5)} = \frac{2\sqrt{3}}{5\pi}\cos(5\omega t + 180 - 5(120°)) = \frac{2\sqrt{3}}{5\pi}\angle -60° \tag{A.0.5}$$

and

$$I_{C(5)} = \frac{2\sqrt{3}}{5\pi}\cos(5\omega t + 180 - 5(240°)) = \frac{2\sqrt{3}}{5\pi}\angle -300°. \tag{A.0.6}$$

The 7^{th} harmonic of the current in the A-phase is in phase with the fundamental and is positive sequence. The 7^{th} harmonic of the phase currents in the generator bus can be expressed as

$$I_{A(7)} = \frac{2\sqrt{3}}{7\pi}\cos 7\omega t = \frac{2\sqrt{3}}{7\pi}\angle 0^\circ \tag{A.0.7}$$

and

$$I_{B(7)} = \frac{2\sqrt{3}}{7\pi}\cos(7\omega t - 7(120^\circ)) = \frac{2\sqrt{3}}{7\pi}\angle -120^\circ \tag{A.0.8}$$

and

$$I_{C(7)} = \frac{2\sqrt{3}}{7\pi}\cos(7\omega t - 7(240^\circ)) = \frac{2\sqrt{3}}{7\pi}\angle -240^\circ. \tag{A.0.9}$$

The two transformer models are analysed individually and their currents are referred back to the generator bus. The phasor diagrams indicating the fundamental current on the primary side and secondary side of the transformers are shown by Fig.'s A.1 and A.2, respectively. Note that the fundamental current of the secondary-side of the delta-star transformer is shifted 30° from the delta-delta transformer. The phase rotation of the phasor diagram is regarded as positive in the counter-clockwise direction and the fundamental current is positive sequence.

The 5^{th} harmonic current is negative sequence. The A-phase current of the 5^{th} harmonic at the secondary of TX1 can be calculated by

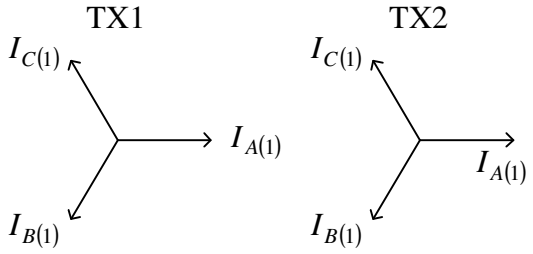

Figure A.1: Phasor diagrams of the fundamental currents on the primary sides of the transformers.

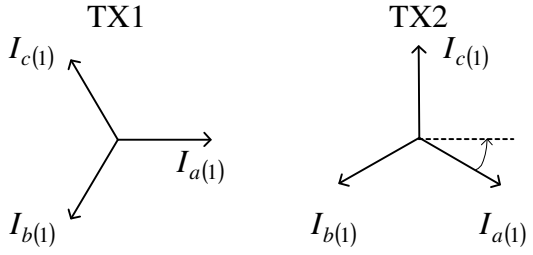

Figure A.2: Phasor diagrams of the fundamental currents on the secondary sides of the transformers.

$$I_{a(5)TX1} = \frac{I_A}{5}\cos(5\omega t + 180°) = \frac{I_A}{5}\angle 180° \tag{A.0.10}$$

while the A-phase current at the secondary of TX2 can be calculated as

$$I_{a(5)TX2} = \frac{I_A}{5}\cos(5(\omega t - 30°) + 180°) = \frac{I_A}{5}\angle 30°. \tag{A.0.11}$$

The phasor diagram of the 5^{th} harmonic current on the secondary side of the transformer is shown by Fig. A.3 and the primary side 5^{th} harmonic current is shown in Fig. A.4. As shown the 5^{th} harmonic currents cancel at the generator power bus. The A-phase current of the 7^{th} harmonic at the secondary of TX1 can be calculated by

$$I_{a(7)TX1} = \frac{I_A}{7}\cos 7\omega t = \frac{I_A}{7}\angle 0° \tag{A.0.12}$$

while the A-phase current at the secondary of TX2 can be calculated as

$$I_{a(7)TX2} = \frac{I_A}{7}\cos 7(\omega t - 30°) = \frac{I_A}{7}\angle -210°. \tag{A.0.13}$$

The phasor diagram of the 7^{th} harmonic current on the secondary side of the transformer is shown by Fig. A.5 and the primary side 7^{th} harmonic current is

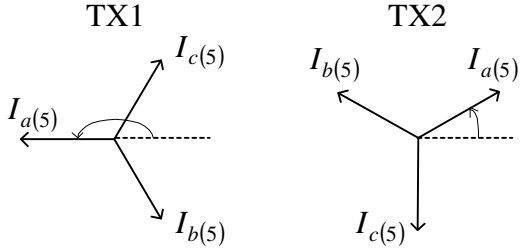

Figure A.3: Phasor diagrams of the 5^{th} harmonic currents on the secondary sides of the transformers.

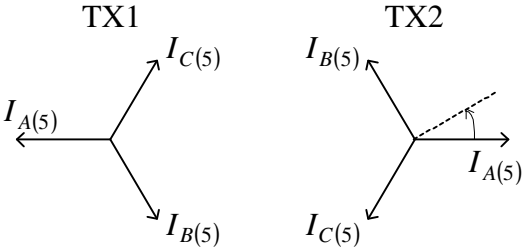

Figure A.4: Phasor diagrams of the 5^{th} harmonic currents on the primary sides of the transformers.

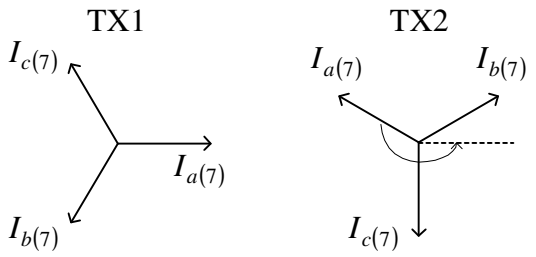

Figure A.5: Phasor diagrams of the 7^{th} harmonic currents on the secondary sides of the transformers.

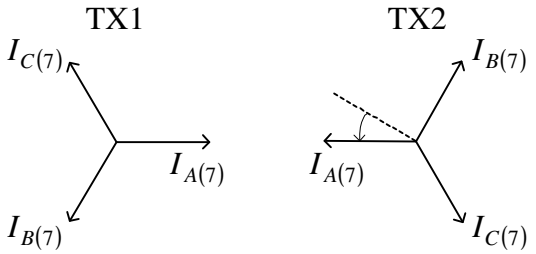

Figure A.6: Phasor diagrams of the 7^{th} harmonic currents on the primary sides of the transformers.

shown in Fig. A.6. As shown the 7^{th} harmonic currents cancel at the generator power bus.

Appendix B

Phase-grouped non-overlapping winding

B.1 Overview

The phase-grouped winding type is based on the non-overlapping winding type where all the coils of the same phase are put side by side. Therefore all the coils forming a phase group occupy a $\frac{1}{3}^{\text{rd}}$ of the circumference of the stator winding, as shown in Fig. B.1.

Due to the absence of iron in the stator there is no unbalanced magnetic pull or an increase of magnetic noise, normally associated with phase-grouped windings in conventional machines. The analytical equations for the phase-grouped windings are the same as those for the non-overlapping windings [30].

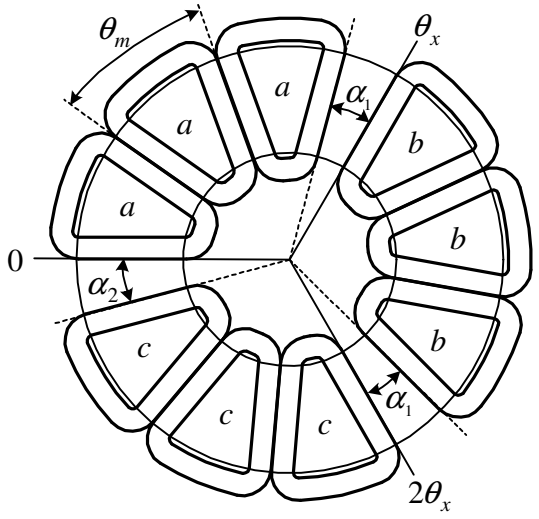

Figure B.1: Schematic of phase-grouped non-overlapping winding.

Figure B.2: Phase-grouped non-overlapping winding.

B.2 Practical measurements

The AFPM wind generator equipped with phase-group non-overlapping winding was evaluated on the test setup in Electrical Machines laboratory. The coreless phase-grouped non-overlapping stator winding is shown in Fig. B.2. The results of the finite element analysis and copper mass tests are tabulated in Table 5.2.

Back-EMF

As part of the stator winding comparative study, the AFPM generator was driven at an electrical frequency of 40 Hz to record the shape of the back-EMF, as shown in Fig. B.3a. The harmonic content of the back-EMF waveform was calculated in the frequency domain, as shown in Fig. B.3b. From this it is clear that the back-EMF of the phase-grouped non-overlapping winding equipped AFPM generator has less 5^{th}- and 7^{th} harmonic content than the normal overlapping winding has, as shown Fig. 5.12b.

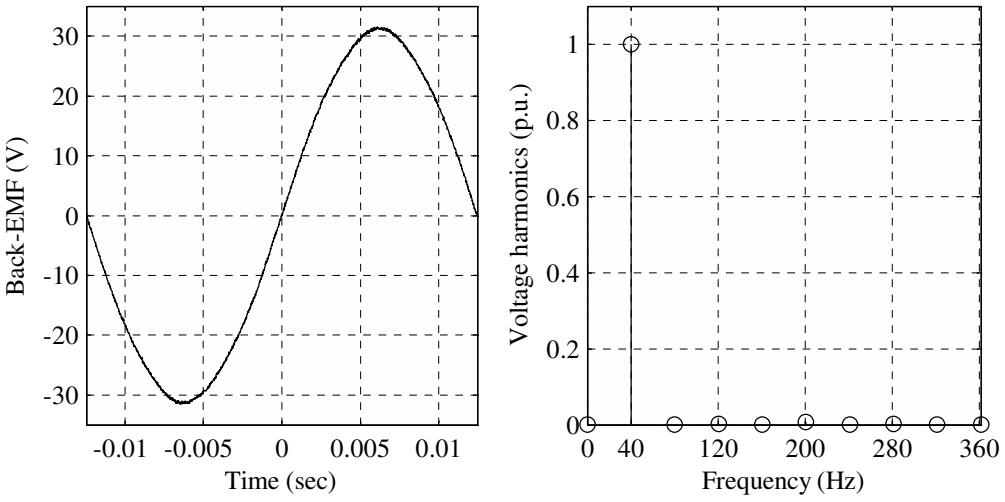

(a) Back-EMF (Time domain) (b) Back-EMF (Frequency domain)

Figure B.3: Harmonic analysis of the back-EMF at 40 Hz.

Appendix C

Inductance calculation

C.1 Inductance

The induced EMF of a coil is proportional to the rate of change of the magnetic flux linkage in a coil. This is also proportional to the rate of change in the current of a coil. This proportionality is referred to as the inductance of the coil. This can be calculated from

$$E_{coil} = L_{coil}\frac{dI_{coil}}{dt} \tag{C.1.1}$$

where E_{coil} is the induced EMF, L_{coil} is inductance of a coil and I_{coil} is the current flowing through a coil. The impedance of the coil, Z_{coil}, can be expressed as

$$Z_{coil} = R_{coil} + j\omega L_{coil} \tag{C.1.2}$$

where ω is the electrical speed of the machine, R_{coil} and L_{coil} are the effective series resistance and inductance, respectively. The coil can now be replaced by an equivalent circuit of a resistor in series with a inductor for simulation and analysis purposes [38].

There are many different types of inductance calculation formulas that can be used to calculate the inductance value of all the different coil shapes and types.

C.2 Non-overlapping winding inductance

In the non-overlapping type winding the inductance calculation in equation (4.4.10) is no longer valid. The reason for this is that the coil-side does not have a square profile. The coil-side width, w, of the coil is much wider than its axial height, h. A formula for calculating the inductance of the non-overlapping winding was

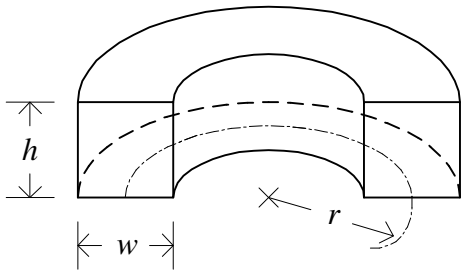

Figure C.1: Cross-section of the round estimation of the coil.

adapted from the air-cored multi-layer solenoid formula [38]. The inductance for the solenoid can be calculated by

$$L_{solenoid} = \frac{4\pi^2 r^2 N_t^2}{h} 10^{-9} \tag{C.2.1}$$

where r is the average radius of the coil, N_t is the number of turns per coil and h is the height of the coil. As shown in Fig. 3.3, the trapezoidal coil's average radius, r, can be calculated as

$$r = \frac{2l_a + l_e}{2\pi} \tag{C.2.2}$$

where l_a and l_e are the active- and end-winding length of the trapezoidal coil respectively, as shown in Fig. C.1.

Appendix D

Eddy currents

In systems where the wind generator is operated at higher frequencies, eddy current losses need to be included in the analysis. Under these higher frequency circumstances the eddy current losses in the stator windings can be significant. The eddy current losses can be simulated as a resistor, R_{eddy}, in parallel with the back-EMF voltage source, E_{gen}, in the equivalent circuit diagram of the synchronous machine.

The following section describes the concept of eddy currents and what can be done to minimise them. In some cases, by sufficiently minimising the effects of eddy-currents their presence can nearly be ignored.

Direct current flows through a conductor and distributes uniformly over the entire cross-sectional area of the conductor. The resistance of the entire cross-sectional area of the conductor to the flow of current is referred to as the dc resistance, R_{dc}, of the conductor and can be calculated by

$$R_{dc} = \frac{\rho l}{a} \tag{D.0.1}$$

where ρ is the resistivity of the material used, l is the length and a is the cross-sectional area of the conductor. When alternating current flows through a conductor it creates a magnetic field around that conductor. This induced magnetic field opposes the penetration of current to the core of the conductor. This causes an increase in the resistance of the conductor [38]. This increase of resistance is referred to as the ac resistance, R_{ac}, of the conductor.

The motion of the magnets across the windings produce a magnetic field in the conductors which induces eddy-currents [18]. These eddy-currents can be split into two types, namely the skin effect and the proximity effect.

D.1 Skin effect

Alternating current that flows through a conductor sets up an alternating magnetic field. This magnetic field can be best described as concentric circles around the

axis of the conductor and is referred to as lines of force, as shown in Fig. D.1a. The magnetic field induces eddy-currents and thus power is dissipated in the conductor. Eddy currents oppose the flow of current in the centre of the wire thereby forcing current to flow closer to the surface of the wire. This effect of the tendency of the current to flow towards the surface of the conductor is increased as the frequency increases. At high frequencies the current flows only in the thin outer skin of the wire while the current density in the centre drops to zero. Therefore the resistance to the flow of alternating current is greater than to the flow of direct current [38].

When direct current is flowing, the current density is the same at all points in the cross-sectional area of the conductor. When alternating current is flowing, the current is displaced more to the surface of the conductor as the frequency increases. Therefore the conductor's effective cross-sectional area is reduced, so the resistance and the power dissipation is increased.

The current density in a conductor decreases from under the surface of the conductor towards the centre. As the current density decreases, a point is reached at some depth below the surface where the current density has decreased to $\frac{1}{\epsilon}$, which is roughly 37% of the value of the current density at the surface. This point is referred to as the depth of penetration point, δ. At low frequencies δ has a high value and R_{dc} is equal to R_{ac}. If the depth of penetration is greater than half the wire diameter, R_{ac} starts to increase. The depth of penetration for copper, δ_{Cu} can be calculated by [38]

$$\delta_{Cu} = \frac{0.066}{\sqrt{f}} \tag{D.1.1}$$

where f is the frequency of the current flowing.

At relatively high operating frequencies these eddy-currents may lead to serious additional losses in the machine. The losses will cause the temperature in the stator windings to increase and therefore the efficiency decreases [18].

D.2 Proximity effect

A coil consists of many turns, which are in close proximity to other turns of the same coil. As explained above, the alternating current that flows through a turn creates a magnetic field. This magnetic field created by one turn cuts another turn in the coil and therefore induces eddy-currents in that second turn, as shown in Fig. D.1b. Thus the resistance of the coil increases due to presence of the magnetic field of another turn. This increase of resistance is referred to as the proximity effect [38].

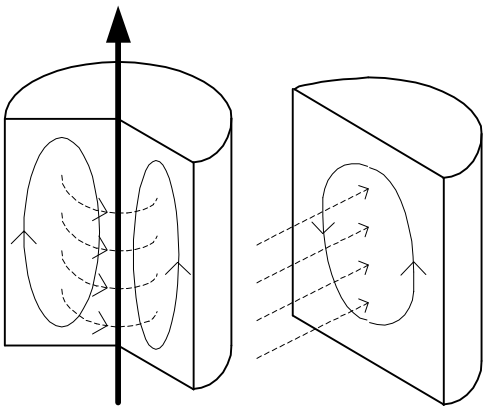

(a) Skin effect (b) Proximity effect

Figure D.1: Figures showing skin and proximity effect.

D.3 Eddy-current losses in a stranded wire

The eddy current losses in a conductor can be reduced by dividing the solid conductor into a bundle of insulated strands of conductors. This in effect increases the resistance of the eddy-current path. If these strands are parallel to one another the strands would have the same losses as the same diameter of solid wire, as the skin effect and proximity effect still occurs. This is because the current will concentrate in some of the strands nearer to the outside. If the strands are interweaved and twisted, each bundle of strands are successfully transposed [38].

The current that flows through a conductor forms a magnetic field in concentric circles along the axis of the conductor. The strands should be interweaved so that the strands are continuously transposed relative to this magnetic field. The induced currents from the perpendicular magnetic field created by the current flowing in other turns will be minimised by the axial twist of the strands [38].

Appendix E

Lead-acid battery

E.1 Overview

A battery is a device which produces electrical energy from spontaneous chemical reactions. It is a portable source of power and can either store or deliver power. The batteries are used for power storage of the surplus energy delivered by the wind generator system. Therefore there is no need for it to be small, light-weight batteries. The primary concern is durability and long service life instead of high power density [54].

There are many different types and sizes of batteries available on the market, but the one that is of interest is the lead-acid type. A lead-acid battery basically consists of two dissimilarly polarised electrodes immersed in an electrolyte. The positive electrode consists of lead dioxide (PbO_2), the negative electrode of lead (Pb) and the electrolyte consists of sulphuric acid (H_2SO_4) in water [54]. When a battery charges, the electrical energy are converted into chemical energy [55].

E.2 Specific factors affecting performance

There are many factors which affect the performance of a battery, amongst them these are the most important

- State of charge (SOC)
- Battery storage capacity
- Rate of charge/discharge
- Ambient temperature
- Age/shelf life

E.3 Equivalent circuit models

A battery model is required to predict the performance of batteries. With the aid of accurate battery models, a circuit designer could optimise the performance of the circuit where the batteries are to be used in [56]. Researchers have developed a wide variety of models, which vary in its complexity. Unfortunately, none of these models are completely accurate. There are many types of battery models including electrochemical, mechanical, hydro-dynamical and finite element models, to name a few. These different models all have their specific purposes and are used to capture the battery's behaviour for these purposes. The battery models which will be looked at in depth are the electrical equivalent models. These models use a combination of voltage sources, resistors and capacitors to model a battery. There exists a wide variety of different types of electrical models which vary in complexity and have an accuracy with about 5% error. Electrical equivalent models are more intuitive and easy to handle especially because it can be modelled alongside the accompaning application circuit [56].

E.4 Thevenin equivalent model

The basic battery model consists of a voltage source, V_{OC}, in series with a resistor, R_i. This resistor, represents the internal resistance of the battery. This battery model shows a simple way of demonstrating the behaviour of the battery voltage, V_b, but oversimplifies the chemistry and physics involved with the inner workings of a lead-acid battery.

An improvement to the basic battery model is the Thevenin equivalent model. The Thevenin equivalent model adds, in series to V_{OC} and R_i, a parallel combination of a capacitor, C_1, and a resistor, R_1, to represent the over voltage at a certain SOC assuming constant V_{OC}.

For all practical reasons the basic battery model was adequate for the purpose of system analysis as it can predict the energy storage ability of the battery. But both the above mentioned models are unable to demonstrate the behaviour of a battery at different states of charge. The models are inaccurate because the model's component values are modelled as constants. In actual fact these component values are not constants but are functions of the battery conditions mentioned above [55].

E.5 Linear and non-linear battery models

The following section is of more accurate battery models that can be used.

An improvement on the Thevenin battery model is the linear electrical battery model. This particular model uses linear components to model the non-linear characteristics of the battery such as the self-discharge and over-voltage characteristics.

To achieve these characteristics the battery bank can be modelled as a voltage source in series with a resistor-capacitor combination [8]. Although this proves to be more accurate it does not take into account the the temperature or the different states of charge of the battery [55].

The next model is the non-linear model, where non-linear elements were used to represent the charge storing capacity of the battery with the use of a capacitor. This represents the non-linear U_{OC} and SOC. These battery components are not constants but are modelled as a function of voltage [55]. In this model the internal resistance of the battery has different values for charge and discharge. This selection between the charge and discharge resistance is achieved by the charge or discharge current flowing in opposite directions through ideal diodes, thereby selecting between different resistor values. A current loop is formed by the self-discharge resistor which is inserted across the source. The self-discharge resistance of a battery is extremely temperature sensitive, hence its value changes dramatically. To achieve the most accurate model possible, the values of the resistances and the capacitances should be determined experimentally [56].

E.6 Model used

The battery models that were discussed in the sections above are not suitable for the simple application that it is intended for. This is due to their complexity and great number of parameters. A simpler battery model could therefore be used if the battery is repeatedly modelled under the same circumstances [55]. Therefore the parameters which only has a small influence on the battery performance can be neglected and it would still yield reasonably accurate results [57].

As mentioned above, the parameters of a battery are multi variable functions of the SOC, the charging current, the temperature and life cycle. Therefore some of these parameters can be simplified to be independent or linear functions. For instance, the temperature factor of a low-capacity battery in constant temperature can be ignored and frequently used batteries can ignore self-discharge. The state of charge of a battery greatly influences the battery performance. The SOC of a lead-acid battery can be monitored by the battery voltage [54]. Therefore if the battery is only modelled in its middle state of charge, which is the most linear region of the operating range, the SOC characteristics can also be ignored. The battery parameters are approximately constant in the 20-80 % SOC region, but change exponentially in the 0-20 % SOC region [56]. This change is due to the internal resistance which increases at extreme SOC [54].

The task is now to develop a battery model based only on what was needed. Thus a modified linear battery model could be used where the battery is modelled merely a resistor in series with a voltage source [57].

Appendix F

Equivalent circuit model

F.1 Overview

As is shown in Fig. F.1, if the AFPM generator has a sinusoidal back-EMF, E_{gen}, and no current is flowing in the wind generator system, the dc-bus voltage, V_{dc}, is calculated as [20]

$$V_{dc} = \sqrt{2}\sqrt{3}V_{rec}\frac{3}{\pi} = \sqrt{6}V_{rec}\frac{3}{\pi} \tag{F.1.1}$$

where V_{rec} is the phase voltage at the terminal of the rectifier. While no current is flowing in the system $E_{gen} = V_{gen} = V_{rec} = V_b$, as shown in Fig. F.1 and $V_{dc} = V_{bat}$ as shown in the ac-equivalent of the system, as shown in Fig. F.3. But, this is not valid for the system under loaded conditions where current is flowing and the rectifier terminal voltage is not a sinusoidal waveform.

Under loaded conditions it can be assumed that after the addition of the series-connected external inductor, L_e, the harmonic line currents which are caused by the low value of L_i, are sufficiently reduced. Therefore, the phase current can be assumed to be a sinusoidal waveform. Thus, the line-to-line voltage at the ac-side of rectifier terminal, $V_{rec_{l-l}}$, will be a stepped squarewave due to the influence of the battery, as shown in Fig. F.2. For the purpose of analysis only the rms-fundamental of the stepped squarewave of line-line voltage, V_{rec}, is analysed as a function of the dc-bus voltage, V_{dc}. By integrating the stepped squarewave of the rectifier terminal voltage, the fundamental of the peak of the rectifier terminal voltage, $V_{rec_{1(p)}}$ is calculated as [7, 45]

$$V_{rec_{1(p)}} = \frac{6}{\pi}\frac{V_{dc}}{3} = \frac{2V_{dc}}{\pi} \tag{F.1.2}$$

where V_{dc} is the dc-bus voltage. To analyse the wind generator system the equivalent circuit analysis, shown Fig. F.1, are converted to an ac-equivalent circuit,

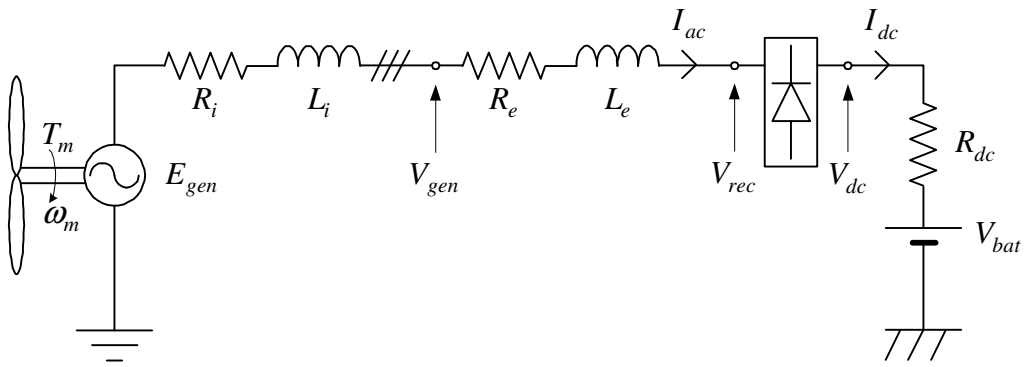

Figure F.1: Per-phase equivalent circuit diagram of the wind generator system.

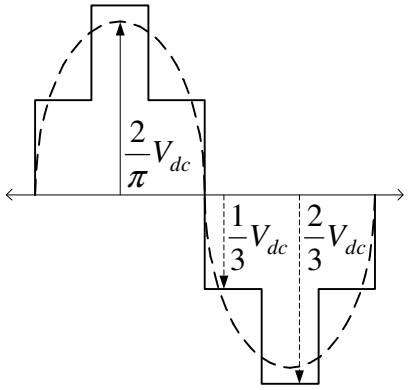

Figure F.2: Rectifier terminal voltage.

shown in Fig. F.3. The rectifier-battery load was modelled by a voltage source, V_b. The ac-equivalent battery voltage, V_b, can be calculated as

$$V_b = V_{rec_{1(rms)}} = \frac{\sqrt{2}(V_{dc} + 2V_d)}{\pi} \tag{F.1.3}$$

where V_d is the forward conducting voltage of the diode [45].

Due to the filtering effect of the external inductance, L_e, the ac-current which flows in the system, I_{ac}, can be regarded as purely sinusoidal. By assuming this, the charging current flowing into the battery bank, I_{dc}, can be calculated as

$$I_{dc} = \sqrt{2} I_{ac} \frac{3}{\pi} \tag{F.1.4}$$

where $\frac{3}{\pi}$ is due to the averaging of the dc-current.

The ac-equivalent of the battery voltage, V_b, can also be calculated by assuming that the power of the wind generator system calculated on the ac-side of the rectifier

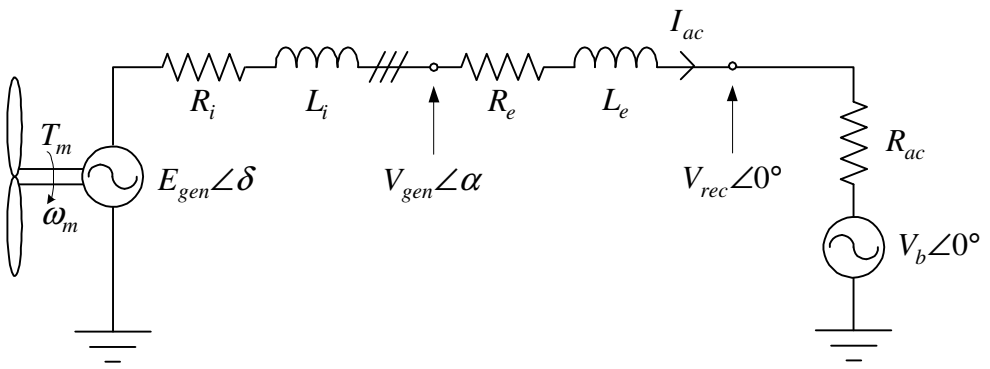

Figure F.3: Per-phase ac-equivalent circuit diagram of the wind generator system.

is equal to the power on the dc-side of the rectifier, where

$$\begin{aligned} 3V_b I_{ac} &= 2V_d I_{dc} + V_{bat} I_{dc} \\ 3V_b I_{dc}\frac{\pi}{3\sqrt{2}} &= 2V_d I_{dc} + V_{bat} I_{dc} \\ V_b &= \frac{\sqrt{2}(2V_d + V_{bat})}{\pi}. \end{aligned} \tag{F.1.5}$$

In the same manner the ac-equivalent internal resistance of the battery bank, R_{ac}, can also be calculated, where

$$\begin{aligned} 3I_{ac}^2 R_{ac} &= I_{dc}^2 R_{dc} \\ 3I_{ac}^2 R_{ac} &= (\frac{3\sqrt{2}}{\pi})^2 R_{dc} \\ R_{ac} &= \frac{6R_{dc}}{\pi^2}. \end{aligned} \tag{F.1.6}$$

Appendix G

Dq-analysis

G.1 Park transformation

The phase voltages of a synchronous machine, v_{ABC} can be calculated by

$$v_{ABC} = R_i i_{ABC} + \frac{d\lambda_{ABC}}{dt} \tag{G.1.1}$$

where i_{ABC} and λ_{ABC} are the phase current and flux linkage in the ABC-reference frame, respectively. R_i is the per-phase internal inductance of the stator winding.

The ABC-reference frame is fixed to the stator. It is convenient to transform the stator reference frame into a synchronously rotating rotor reference frame. The rotor $dq0$-reference frame is fictitious windings that rotate at the same rotating speed as the rotor [58]. The transformation changes the synchronous machine variable to a reference frame that rotates at an arbitrary angular velocity.

The ABC-equivalent circuit parameters of the wind generator system can be transformed from the ABC-reference frame to the $dq0$-reference frame with the use of Park's transformation. The phase voltage in the $dq0$-reference frame, v_{dq0}, can be calculated by

$$[v_{dq0}] = [K_s][v_{ABC}] \tag{G.1.2}$$

where

$$K_s = \frac{2}{3}\begin{bmatrix} \cos\theta & \cos(\theta - \frac{2\pi}{3}) & \cos(\theta + \frac{2\pi}{3}) \\ \sin\theta & \sin(\theta - \frac{2\pi}{3}) & \sin(\theta + \frac{2\pi}{3}) \\ \frac{1}{2} & \frac{1}{2} & \frac{1}{2} \end{bmatrix} \tag{G.1.3}$$

G.2 5th harmonic current analysis

From Fig.'s 4.10 and 4.11, the 5th harmonic d- and q-axis currents can be calculated by

$$i_{d5} = -\frac{\omega_5 L_q i_{q5}}{R_s} \tag{G.2.1}$$

and

$$i_{q5} = -\frac{\omega_5 L_d i_{d5} - v_{q5}}{R_s} \tag{G.2.2}$$

where in coreless AFPM machine system inductance, $L_s = L_d = L_q$. Therefore

$$\begin{aligned} i_{d5} &= -\frac{\omega_5 L_d i_{q5}}{R_s} \\ &= -\frac{\omega_5 L_d}{R_s}\left(\frac{\omega_5 L_d i_{d5} - v_{q5}}{R_s}\right) \\ &= \frac{\omega_5 L_d v_{q5}}{R_s^2 + \omega_5^2 L_d^2} \end{aligned} \tag{G.2.3}$$

and

$$\begin{aligned} i_{q5} &= \frac{\omega_5 L_q i_{d5} - v_{q5}}{R_s} \\ &= \frac{\omega_5 L_q\left(\frac{-\omega_5 L_q i_{q5}}{R_s}\right) - v_{q5}}{R_s} \\ &= -\frac{v_{q5}}{R_s + \left(\frac{\omega_5^2 L_q^2}{R_s}\right)} \end{aligned} \tag{G.2.4}$$

G.3 5th harmonic q-axis voltage

It is required that the value of the 5th harmonic component of the q-axis voltage is calculated. The 5th harmonic q-axis voltage, v_{q5} is calculated from the value of the ac-side of the rectifier, V_{rec} in Fig. 4.1. V_{rec} can be calculated from Fig. 4.2 as

$$V_{rec} = V_b + I_{ac} R_{ac} \tag{G.3.1}$$

where V_b is the ac-equivalent battery voltage, I_{ac} is the line current and R_{ac} is the ac-equivalent battery resistance. The power calculated at the ac-side of the rectifier, P_{rec}, can be calculated as

$$P_{rec} = 3V_{rec}I_{ac}. \tag{G.3.2}$$

From equations G.3.1 and G.3.2 the V_{rec} can be calculated by

$$\frac{V_{rec} - V_b}{R_{ac}} = \frac{P_{rec}}{3V_{rec}} \tag{G.3.3}$$

thus

$$V_{rec} = \frac{V_b + \sqrt{V_b^2 + \frac{4}{3}P_{rec}R_{ac}}}{2}. \tag{G.3.4}$$

G.4 Inductance calculation

The inductance required for the suppression of the 5^{th} harmonic component in the d-axis equivalent circuit can be calculated, from equation G.2.3, as

$$\begin{aligned} i_{d5} &= \frac{\omega_5 L_d v_{q5}}{R_s^2 + \omega_5^2 L_d^2} \\ \omega_5 L_d v_{q5} &= i_{d5}R_s^2 + i_{d5}\omega_5^2 L_d^2 \\ L_d &= \frac{v_{q5} + \sqrt{v_{q5}^2 - 4i_{d5}^2 R_s^2}}{2i_{d5}\omega_5} \end{aligned} \tag{G.4.1}$$

Appendix H

Internal inductance measurements

As previously mentioned, coreless axial flux permanent magnet machines are known to have a very low internal inductance. Therefore accurate measurements of the inductance are extremely difficult to measure practically. A further complication is that as these type of machine frequently make use of high pole numbers, accurate mechanical positioning is made even more difficult [16].

In the following sections a couple of methods of measuring the internal inductance, L_i, of a coreless AFPM machine are discussed.

H.1 Standstill frequency tests

The rotor of the AFPM generator was aligned in its d-axis position, as shown in Fig. H.1a. It is important to note that any small misalignment would result in measurement errors, which is particularly difficult in high pole number machines such as this. The three phases were connected in star. The A-phase was fed with a sinusoidal current and the rotor was manually rotated until a voltage drop of zero was measured across the combination of B- and C-phases [16].

With the rotor aligned in the d-axis position, the B- and C-phases were connected together and a sinusoidal voltage was applied across the stator, as shown in Fig. H.1b. The d-axis inductance, L_d, could now be calculated by measuring the voltage and current across the windings [23]. To calculate the q-axis inductance, the rotor was held in this position, the A-phase was disconnected and a sinusoidal voltage was applied across the B- and C-phases, as shown in Fig. H.1c. As the AFPM machine uses surface-mounted permanent magnets, $L_i = L_d = L_q$. The internal inductance can be calculated by

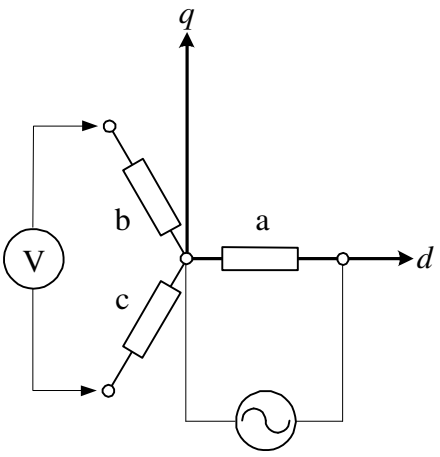

(a) d-axis alignment of the rotor.

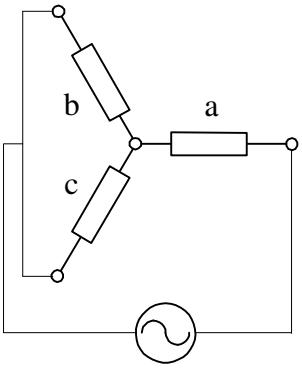

(b) connection diagram for d-axis inductance measurement.

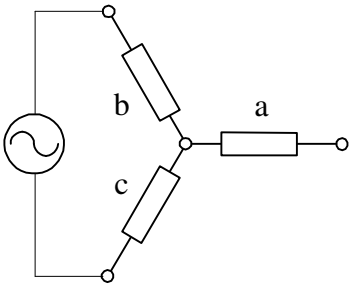

(c) connection diagram for q-axis inductance measurement.

Figure H.1: connection diagram for d and q-axis inductance measurement.

$$\begin{aligned} \theta_A &= \arccos(\frac{P_A}{S_A}) \\ Z_A &= \frac{v_A \angle 0^\circ}{i_A \angle \theta_A} \\ R_a &= \Re(Z_A) \\ L_i = L_A &= \frac{\Im(Z_A)}{\omega} \end{aligned} \tag{H.1.1}$$

where P_A and S_A are the true and apparent power of the A-phase, respectively. θ_A is the angle between v_A, A-phase voltage, and i_A, A-phase current. The Z_A is A-phase impedance which is a function of L_i.

H.2 Decay tests

The standstill locked rotor decay tests were performed to measure the d- and q-axis inductances of the coreless stator of the AFPM machine. The advantage of this test above a rotating load test is that the core losses can be totally ignored.

To determine the d-axis inductance of the AFPM machine, a dc voltage source is connected in parallel across a free-wheeling diode which is connected across the stator windings as shown in Fig. H.2a. From the moment the switch was opened the phase voltages and currents where monitored. The tests were repeated to determine the q-axis inductance with the AFPM machine connected as shown in Fig. H.2b. The d- and q-axis air-gap flux linkage components can be calculated by [59]

$$\lambda_d = \int_{\infty}^{t} [v_d - i_d R_i] dt \tag{H.2.1}$$

and

$$\lambda_q = \int_{\infty}^{t} [v_q - i_q R_i] dt \tag{H.2.2}$$

where R_i is the per-phase stator resistance. The d- and q-axis system inductances can now be calculated by

$$L_d = \frac{\lambda_d}{i_d} \tag{H.2.3}$$

and

$$L_q = \frac{\lambda_q}{i_q} \tag{H.2.4}$$

where $L_i = L_d = L_q$ in an coreless AFPM machine.

H.3 Load tests

Another method of investigating the stator winding inductance of a coreless AFPM machine is with the use of the load test. The AFPM generator was loaded with a balanced resistive load and driven at rated rotating speed. After the stator windings have reached steady-state temperature the phase shift between the voltage and the back-EMF was measured [16]. From this the phasor diagram shown in Fig. H.3a can be derived. With the use of the sine-method of calculating triangles as shown in Fig.'s H.3b and H.3c, the following can be derived and the system inductance, L_s, determined by

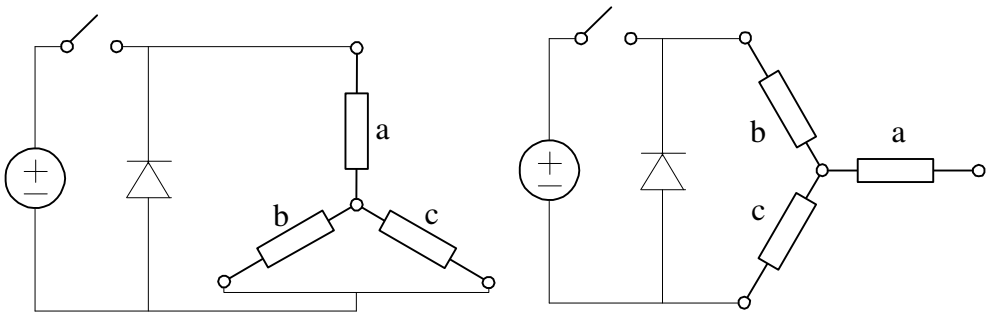

(a) d-axis decay test (b) q-axis decay test

Figure H.2: Decay test setup.

$$
\begin{aligned}
x &= \sqrt{V_b^2 + (I_r R_s)^2 - 2 V_b I_r R_s \cos(\pi - \theta)} \\
\frac{I_r R_s}{\sin A} &= \frac{V_b}{\sin B} = \frac{x}{\sin(\pi - \theta)} \\
A &= \sin^{-1}\left(\frac{I_r R_s \sin(\pi - \theta)}{x}\right) \\
B &= \sin^{-1}\left(\frac{V_b \sin(\pi - \theta)}{x}\right) \\
\frac{I_r \omega L_s}{\sin(\delta + A} &= \frac{E_{gr}}{\sin(\frac{\pi}{2} + B)} = \frac{x}{\sin X} \\
X &= \sin^{-1}\left(\frac{x \sin(\frac{\pi}{2} + B)}{E_{gr}}\right) \\
\delta &= \pi - A - \frac{\pi}{2} - B - X \\
Ls &= \frac{x \sin(\delta + A)}{I_r \omega \sin X}.
\end{aligned}
\tag{H.3.1}
$$

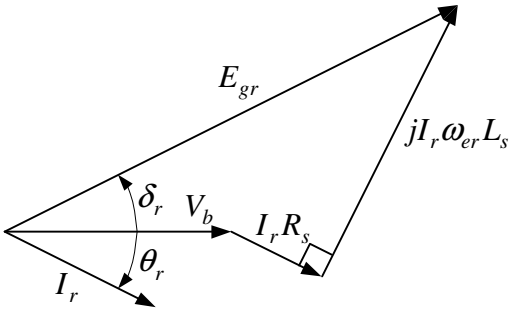

(a) Load test to calculate the inductance of the system.

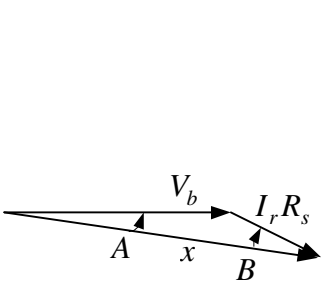

(b) Sine method of solving triangles

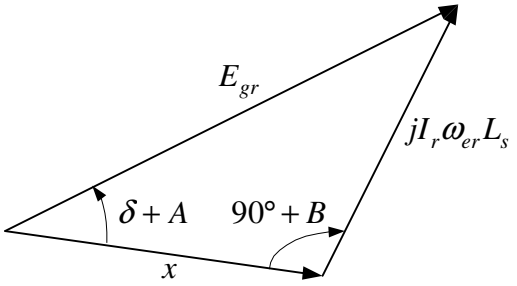

(c) Sine method of solving triangles

Figure H.3: Phasor diagram of the AFPM generator with balanced resistive load connected.

Bibliography

[1] J. Gieras, R. Wang, and M. Kamper, *Axial Flux Permanent Magnet Brushless Machines*. Kluwer, 2004.

[2] J. Rizk and M. H. Nagrial, "Permanent-magnet generators for wind turbines."

[3] R. Teodorescu and F. Blaabjerg, "Flexible control of small wind turbines with grid failure detection operating in stand-alone and grid-connected mode," *Power Electronics, IEEE Transactions on*, vol. 19, no. 5, pp. 1323–1332, 2004.

[4] A. De Broe, S. Drouilhet, and V. Gevorgian, "A peak power tracker for small wind turbines in battery charging applications," *Energy Conversion, IEEE Transaction on*, vol. 14, no. 4, pp. 1630–1635, 1999.

[5] E. Odendal, "Design, construction and testing of a small wind generator with electronic controller for domestic use."

[6] E. Eggleston, "How can i calculate the amount of power available at a given wind speed?" Feb 1998.

[7] E. Muljadi, S. Drouilhet, and R. Holz, "Analysis of wind power for battery charging," in *ASME Wind Energy Symposium*, 1996.

[8] B. Borowy and Z. Salameh, "Dynamic response of a stand-alone wind energy conversion system with battery energy storage to a wind gust," *Energy Conversion, IEEE Transaction on*, vol. 12, no. 1, pp. 73–78, 1997.

[9] D. A. Spera, Ed., *Wind Turbine Technology*. ASME Press, 1994.

[10] R. Gasch and J. Twele, *Wind power plants*. Solarpraxis, 2002.

[11] J. Bosman, "The aerodynamic and structural design of a 1kw wind turbine blade," 2003.

[12] E. W. Golding, *The generation of electricity by wind power*. E. & F. N. Spon Limited, 1955.

[13] E. Muljadi, C. Butterfield, and Y.-H. Wan, "Axial-flux modular permanent-magnet generator with a toroidal winding for wind-turbine applications," *Industry Applications, IEEE Transactions on*, vol. 35, no. 4, pp. 831–836, 1999.

[14] N. A. Karim, N. A. Karim, J. Azzouzi, and G. Barakat, "Influence of skewing on the performances of an axial flux pm wind generator coupled to a diode rectifier," in *Electric Machines & Drives Conference, 2007. IEMDC '07. IEEE International*, J. Azzouzi, Ed., vol. 2, 2007, pp. 1037–1042.

[15] F. Libert and J. Soulard, "Design study of direct-driven surface mounted permanent magnet motor for low speed application," *Symposium on Advanced Electromechanical Motion Systems Electromotion 2003*, vol. 1, pp. 252–257, 2003.

[16] G. Tomassi, M. Topor, F. Marignetti, and I. Boldea, "Characterization of an axial-flux machine with non-overlapping windings as a generator," *Electromotion*, vol. 13, pp. 73–79, 2006.

[17] K. Nilsson, E. Segergren, and M. Leijon, "Simulation of direct drive generators designed for underwater vertical axis turbines," in *Fifth European Wave Energy Conference*, 2003.

[18] R.-J. Wang and M. Kamper, "Calculation of eddy current loss in axial field permanent-magnet machine with coreless stator," *Energy Conversion, IEEE Transaction on*, vol. 19, no. 3, pp. 532–538, 2004.

[19] R.-J. Wang, M. Kamper, K. Van der Westhuizen, and J. Gieras, "Optimal design of a coreless stator axial flux permanent-magnet generator," *Magnetics, IEEE Transactions on*, vol. 41, no. 1, pp. 55–64, 2005.

[20] R. Esmaili and L. Xu, "Sensorless control of permanent magnet generator in wind turbine application," in *Industry Applications Conference, 2006. 41st IAS Annual Meeting. Conference Record of the 2006 IEEE*, vol. 4, 2006, pp. 2070–2075.

[21] E. Muljadi and C. Butterfield, "Pitch-controlled variable-speed wind turbine generation," *Industry Applications, IEEE Transactions on*, vol. 37, no. 1, pp. 240–246, 2001.

[22] S. Drouilhet, E. Muljadi, R. Holz, and V. Gevorgian, "Optimizing small wind turbine performance in battery charging applications," in *Windpower '95*, 1995.

[23] D. Vizireanu, D. Vizireanu, S. Brisset, and P. Brochet, "Design and optimization of a 9-phase axial-flux pm synchronous generator with concentrated winding for direct-drive wind turbine," in *Industry Applications Conference, 2006.*

41st IAS Annual Meeting. Conference Record of the 2006 IEEE, S. Brisset, Ed., vol. 4, 2006, pp. 1912–1918.

[24] J. Kolar, H. Ertl, and F. Zach, "Design and experimental investigation of a three-phase high power density high efficiency unity power factor pwm (vienna) rectifier employing a novel integrated power semiconductor module," in *Applied Power Electronics Conference and Exposition, 1996. APEC '96. Conference Proceedings 1996., Eleventh Annual*, vol. 2, 1996, pp. 514–523 vol.2.

[25] A. Pathak, R. Locher, and H. Mazumdar, "3-phase power factor correction, using vienna rectifier approach and modulr construction for improved overall performance, efficiency and reliability," in *Power Electronics Conference*, 2003.

[26] W. Xu, "Component modeling issues for power quality assessment," in *IEEE Power Engineering Review*, 2001.

[27] W. Lawrance and W. Mielczarski, "Harmonic current reduction in a three-phase diode bridge rectifier," *Industrial Electronics, IEEE Transactions on*, vol. 39, no. 6, pp. 571–576, 1992.

[28] SquareD, "Harmonic mitigating transformers," July 2003.

[29] W. Nichols and J. Cosse, R.E., "An illustration of harmonic suppression due to transformer connection-a simplified approach," in *Petroleum and Chemical Industry Conference, 1988, Record of Conference Papers., Industrial Applications Society 35th Annual*, 1988, pp. 197–203.

[30] M. Kamper, R. Wang, and F. Rossouw, "Analysis and performance of axial flux permanent magnet machine with air-cored non-overlapping concentrated stator windings," in *IAS*, 2008.

[31] M. Khan and P. Pillay, "Design of a pm wind generator, optimised for energy capture over a wide operating range," in *Electric Machines and Drives, 2005 IEEE International Conference on*, 2005, pp. 1501–1506.

[32] R. Wang, "Design aspects and optimisation of an axial field permanent magnet machine with an ironless stator," Ph.D. dissertation, University of Stellenbosch, 2003.

[33] J. Cros and P. Viarouge, "Synthesis of high-performance pm motors with concentrated windings," *Power Engineering Review, IEEE*, vol. 22, no. 4, pp. 74–74, 2002.

[34] A. Parviainen, J. Pyrhonen, and P. Kontkanen, "Axial flux permanent magnet generator with concentrated winding for small wind power applications," in

Electric Machines and Drives, 2005 IEEE International Conference on, 2005, pp. 1187–1191.

[35] F. Magnussen and C. Sadarangani, "Winding factors and joule losses of permanent magnet machines with concentrated windings," in *Electric Machines and Drives Conference, 2003. IEMDC'03. IEEE International*, vol. 1, 2003, pp. 333–339 vol.1.

[36] N. Bianchi, S. Bolognani, and M. Dai Pre, "Magnetic loading of fractional-slot three-phase pm motors with non-overlapped coils," in *Industry Applications Conference, 2006. 41st IAS Annual Meeting. Conference Record of the 2006 IEEE*, vol. 1, 2006, pp. 35–43.

[37] F. W. Grover, *Inductance Calculations Working Formulas and Tables.* D. van Nostrand Company Inc, 1946.

[38] V. G. Welsby, *The theory and design of inductance coils.* MacDonald & Co, 1950.

[39] F. Libert and J. Soulard, "Investigation on pole-slot combinations for permanent-magnet machines with concentrated windings."

[40] M. J. Kamper, "Analysis and winding design of linear permanent magnet machine with overlap air-cored windings," 2008.

[41] F. Magnussen, P. Thelin, and C. Sadarangani, "Performance evaluation of permanent magnet synchronous machines with concentrated and distributed windings including the effect of field-weakening," in *Power Electronics, Machines and Drives, 2004. (PEMD 2004). Second International Conference on (Conf. Publ. No. 498)*, vol. 2, 2004, pp. 679–685 Vol.2.

[42] Y. Yoshikawa, H. Li, and H. Murakami, "Design of ultra low acoustic noise and high power density direct drive machines with double rotor and toroidally wound structure," in *Industry Applications Conference, 2006. 41st IAS Annual Meeting. Conference Record of the 2006 IEEE*, vol. 4, 2006, pp. 1949–1954.

[43] F. Magnussen, D. Svechkarenko, P. Thelin, and C. Sadarangani, "Analysis of a pm machine with concentrated fractional pitch windings."

[44] F. G. Rossouw and M. J. Kamper, "Use of air-cored axial flux permanent magnet generator in direct battery charging wind energy systems," in *Power Electronics and Drive Systems*, 2007.

[45] N. Mohan, T. Undeland, and W. Robbins, *Power Electronics*, B. Zobrist, Ed. Wiley, 2003.

[46] C. Qiao and K. Smedley, "Three-phase unity-power-factor star-connected switch (vienna) rectifier with unified constant-frequency integration control," *Power Electronics, IEEE Transactions on*, vol. 18, no. 4, pp. 952–957, 2003.

[47] T. Skvarenina, *The Power Electronics Handbook*, T. Skvarenina, Ed. CRC Press, 2002.

[48] R. Lisner and P. Timar, "A new approach to electric motor acoustic noise standards and test procedures," *Energy Conversion, IEEE Transaction on*, vol. 14, no. 3, pp. 692–697, 1999.

[49] H. Klug, "Noise from wind turbines standards and noise reduction procedures," in *Forum Acusticum 2002*, September 2002.

[50] S.-H. Lee, J.-P. Hong, W.-T. Lee, S.-M. Hwang, J.-Y. Lee, and Y.-K. Kim, "Optimal design for noise reduction in interior permanent magnet motor," in *Industry Applications Conference, 2006. 41st IAS Annual Meeting. Conference Record of the 2006 IEEE*, vol. 4, 2006, pp. 1927–1932.

[51] J. Fiedler, K. Kasper, F. Chaparro, and R. De Doncker, "Effectiveness of noise reducing measures in switched reluctance drives," in *Industry Applications Conference, 2006. 41st IAS Annual Meeting. Conference Record of the 2006 IEEE*, vol. 3, 2006, pp. 1163–1170.

[52] J. Zhao, "Causes and reduction of mechanical vibration in an electrical drive system," Master's thesis, University of Stellenbosch, 1998.

[53] I. Measurement Specialities, "Piezo film sensors technical manual," April 1999.

[54] K. Peters, *Modern battery technology*, C. D. S. Tuck, Ed. Ellis Horwood, 1991.

[55] Z. Salameh, M. Casacca, and W. Lynch, "A mathematical model for lead-acid batteries," *Energy Conversion, IEEE Transaction on*, vol. 7, no. 1, pp. 93–98, 1992.

[56] M. Chen and G. Rincon-Mora, "Accurate electrical battery model capable of predicting runtime and i-v performance," *Energy Conversion, IEEE Transaction on*, vol. 21, no. 2, pp. 504–511, 2006.

[57] P. Ekdunge, "A simplified model of the lead/acid battery," *Journal of Power Sources*, vol. 46, pp. 251–262, 1993.

[58] P. C. Krause, *Analysis of Electric Machinery and Drive Systems*, S. V. Kartalopoulos, Ed. Wiley-Interscience, 2002.

[59] M. Kamper and A. Volschenk, "Effect of rotor dimensions and cross magnetisation on ld and lq inductances of reluctance synchronous machine with cageless flux barrier rotor," *IEE Proc. Electr. Power Appl.*, vol. 141, pp. 213–220, 1994.